Master Thesis

# Stability Analysis of a Rotating Cantilever Beam inside a Geotechnical Centrifuge

Dakka Sricharan

TU Delft

Witteveen + Bos

# Stability Analysis of a Rotating Cantilever Beam inside a Geotechnical Centrifuge

by

Dakka Sricharan

**Master of Science Thesis**

**Faculty of Civil Engineering and Geosciences**
**Delft University of Technology**

Student Number: 5932785

Committee Members:

| | |
|---|---|
| Dr. Ir. Apostolos Tsouvalas | TU Delft - Chairman |
| Dr. Ir. Evangelos Kementzetzidis | TU Delft |
| Dr. Ir. Alessandro Cabboi | TU Delft |
| Ir. Stavros Panagoulias | TU Delft & Siemens Energy |
| Ir. Apostolos Bougioukos | Witteveen+Bos |

An electronic version of this thesis is available at
https://repository.tudelft.nl/

Cover photo source: ngcf.edu.au

TU Delft ; Witteveen + Bos ;

# Acknowledgements

Where shall I begin? Well, let me start by describing this thesis, which was conducted as the final aspect of obtaining a Master of Science degree from Delft University of Technology. Finishing this thesis has been a challenging yet rewarding experience. The research was performed in collaboration with Witteveen+Bos, a consultancy and design firm offering services in the fields of water, infrastructure, environment, and construction. This study is intended for engineers and researchers interested in performing experiments on small-scale models of slender structures, such as offshore wind turbines founded on monopiles, in a geotechnical centrifuge.

This thesis would not have been possible without the guidance of all my supervisors, and I would like to express my deepest gratitude to them. To Dr. Apostolos Tsouvalas, I will forever be in debt for considering me and trusting me with this thesis. I am glad to have taken one step closer to understanding the physics behind the mathematics of differential equations and stability analysis. Your ability to connect the dots far ahead surprises me every time we discuss my thesis. To Ir. Stavros Panagoulias, you are more than a mentor, and I consider you a well-wisher. Thank you for always steering me in the right direction whenever I deviate, for being patient with my inexperience, and for helping me beyond my thesis. To Ir. Apostolos Bougioukos, I am fortunate to have met another such gentleman of a mentor. Thank you for always offering an engineer's perspective and giving me the freedom to develop my own ideas, and I hope I can continue to collaborate with you in the future. To Dr. Alessandro Cabboi, thank you for joining my committee at the last moment and accommodating me into your busy schedule when I requested. Finally, to Dr. Vagelis Kementzetzidis, I'm very glad Stavros suggested that I approach you to join my assessment committee. Your intuition about the spinning instability helped me to better understand the physics behind this study. Here's to looking forward to working with you in your team.

Let me take a step back to the beginning of the academic year at TU Delft. It was my first time outside my home country, and I am not someone who can make friends easily. However, I was fortunate to have found a group of international friends who have since become my family. We call ourselves the Habaibi group. Without them, the differential equations might have gotten the best of me, and I would probably have gone insane. I made some of my best memories in Delft and in the Netherlands with you guys, and I am so very thankful for that.

I am also grateful for the TU Delft ambassador programme, through which I met Bruno, my ambassador. He helped me find my way through both campus life and academics. Bruno, you inspired me to become an ambassador myself, an experience that will always remain close to my heart. You will forever be my ambassador.

The second year was the most challenging period of my life, but looking back, I am glad that I pushed myself, especially when I said yes to becoming a board member of U-BASE, because that was one role completely outside my comfort zone. Thank U, Grey, for being the best committee member I could have asked for. Thank U, U-BASE, for teaching me how to enjoy a drink and for the study tour trip to Japan. Not even in my wildest dreams would I have gone to Japan.

I was also fortunate that Dr. Apostolos selected me as a student assistant for the course, Slender Structures, which gave me the motivation to pursue structural dynamics as my career. I consider myself lucky to have been part of the teaching team, helping and working alongside Hans and Andrei, an opportunity that only a few selected students get to experience.

But the idea of joining TU Delft originated when I was working back in Mumbai. I must thank my family at Force SE, where I had the opportunity to work and grow as an engineer. I am especially grateful to Ir. Akhilesh Lahoti for always giving me opportunities that encouraged me to learn more and push my limits. I would also like to thank Ir. Harshal Chandna for suggesting TU Delft. I believe I owe all my experiences and learnings at TU Delft to you. Amit, Sagar, and Prachi, of course, you too deserve a special mention.

It is not very common in our tradition to explicitly express our affection to our parents, so I take this chance to talk about you. Maa, Daddy, I owe my life to you, and I cannot tell you how much I respect you for all the sacrifices you made and are still making for us.

Finally, to Prof. Dr. Andrei Metrikine, words cannot express my gratitude to you. The subject I learnt during your classes helped me become a student assistant, perform this thesis, and even get selected for a PhD position. You inspired me to pursue structural dynamics, and I will forever be a fanboi of you, Andrei.

*Dakka Sricharan*
*Delft, September 2025*

# Summary

A geotechnical centrifuge is used to conduct tests on small-scale models to obtain data on the response of real-life structures. In the field of earthquake engineering, centrifuges can be used to model soil-structure interaction and to analyse structural response to earthquakes through scaled models. By rotating the centrifuge at high angular velocities, the model inside the centrifuge can experience the stresses corresponding to a full-scale prototype. Through simplified scaling laws, the dimensions of the small-scale model are estimated, and the results from these tests can be extrapolated to study the behaviour of the prototype.

When the small-scale model of a dynamically sensitive structure, such as an offshore wind turbine, is subjected to high angular velocities inside a centrifuge, it is essential that the model remains stable to obtain meaningful results from the test. Instabilities, such as divergence or flutter, may arise in the small-scale model depending on the system's parameters due to the action of pseudo-forces and coupling between the displacement fields, which may lead to the failure of the model. Moreover, it is unclear whether the simplified scaling laws can still be applied for such slender small-scale models due to the action of these pseudo-forces and the coupling terms. Therefore, understanding the behaviour of these dynamically sensitive small-scale models under centrifuge conditions is important to ensure their stability and to obtain conclusive results about the prototype.

This research represents the small-scale model of a monopile-founded offshore wind turbine inside a centrifuge as a homogeneous Rayleigh cantilever beam rotating about a vertical axis, with each point along the beam consisting of three translational displacements. A mathematical model is formulated using Lagrangian formalism that incorporates all relevant pseudo-forces and coupling of displacement fields that may affect the stability of the small-scale model. Euler-Lagrange equations are then applied to formulate the governing equations of motion, and a dimensionless form of the equations is presented to draw general conclusions. Moreover, the effect of soil-structure interaction is considered using a lumped spring model.

Subsequently, an eigenvalue analysis is performed using analytical and numerical approaches. The numerical approach is more robust and is applied to calculate the eigenproperties of the system, although it requires a good initial guess. The technique of representing the response as a summation of assumed modes is explored in the analytical approach, and a convergence study is conducted. Afterwards, a parametric study is performed to identify the factors influencing stability. The angular velocity at which the onset of instability happens is also determined. Finally, the findings are applied to a case study of a small-scale model of an offshore wind turbine tested inside the centrifuge facility at ETH Zürich as part of the research project, DONISIS, led by TU Delft.

The results of this study demonstrate that, for the small-scale beam model of a monopile-founded offshore wind turbine tested inside a centrifuge, the dominant instability mode is the divergence of chordwise lateral bending. This instability arises from the axial compression induced by the centrifugal forces acting along the beam. The coupling of displacement fields through Coriolis forces does not affect the onset of instability, although its influence on the eigenproperties becomes apparent only at angular velocities far exceeding the practical operating range of a centrifuge. Since the Coriolis terms have no significant impact on system behaviour, their effect on scaling laws can be regarded as negligible. Consequently, the existing scaling laws remain applicable to small-scale models of rotating beams within the practically operating range of angular velocities of the centrifuge.

# Contents

# List of Figures

# List of Tables

# Abbreviations

| Abbreviation | Definition |
|---|---|
| AMM | Assumed-Modes Method |
| DMM | Direct modelling method |
| DOF(s) | Degree(s) of Freedom |
| EOM(s) | Equation(s) of Motion |
| ETHZ | ETH Zürich |
| OWT | Offshore wind turbine |
| SSI | Soil-Structure Interaction |

# 1

# Introduction

## 1.1. Background and Motivation

When a rigid body of mass $M$ moves in a circular path of radius $r$ with a uniform speed, it experiences an acceleration of $\Omega^2 r$ towards the center of rotation, where $\Omega$ is the angular velocity. The corresponding force required to maintain this uniform circular motion is given by $F = Mr\Omega^2$. As the angular velocity increases, the force experienced by the body increases. This is the working principle of a geotechnical centrifuge, widely used in soil mechanics to simulate stresses at great depths. For instance, stress experienced by soil due to its self-weight at a depth of $100\,\mathrm{m}$ below the ground level can be replicated in a centrifuge of radius $4\,\mathrm{m}$ by rotating the corresponding small-scale model of depth $1\,\mathrm{m}$ at an angular velocity of $16\,\mathrm{rad\,s^{-1}}$, which produces an enhanced acceleration field of $\Omega^2 r = 16^2 \times 4 = 1000\,\mathrm{m\,s^{-2}} \approx 100\,\mathrm{g}$ [15].

In earthquake engineering, centrifuge modelling is widely used to investigate the effects of soil-structure interaction (SSI), where increased gravity is applied to small-scale models to simulate the stresses experienced by full-scale prototypes. Consider an offshore wind turbine (OWT) whose performance when subjected to an earthquake is to be investigated. Simulating a seismic event on a real-life model is prohibitively expensive. However, earthquake motion can be replicated within the centrifuge on a small-scale model, allowing us to study the structural performance of the full-scale prototype during a seismic event. In this way, centrifuge modelling provides a practical approach to investigate the behaviour of OWTs by conducting tests on their scaled models.

To calculate the dimensions of a small-scale model, established scaling laws [10] are used, which primarily consider an inertial frame of reference for the rotating model under centrifugal force, disregarding Coriolis and Euler fictitious forces. This assumption is generally accurate for quasi-static SSI applications when the small-scale model is not moving within the centrifuge but may be questioned in systems experiencing significant dynamic effects, such as those with slender superstructures. A notable example is an OWT supported by a monopile.

Consider the small-scale model of an OWT, which is a slender structure and hence dynamically sensitive. Since the model is flexible and can move within the centrifuge, it not only experiences centrifugal acceleration but also other pseudo-accelerations (Coriolis & Euler accelerations). Simplified scaling laws only consider centrifugal force and may not be applicable to calculate the dimensions of the small-scale model of such dynamically sensitive structures and to extrapolate the results [7]. Hence, a mathematically rigorous approach needs to be adopted to derive the mathematical model of a dynamically sensitive structure, which is then used to verify if the simplified scaling laws are also applicable and to study the performance of the full-scale prototype.

An interesting phenomenon to study is the instability that may arise in the small-scale model that is being tested inside the centrifuge. The small-scale model of a monopile-founded OWT can be imagined as a rotating cantilever beam, which is a slender structure, with part of it embedded in the soil and the

rest extending outside. The external forces acting on the beam are the gravitational force due to the self-weight of the beam and pseudo-forces such as centrifugal, Coriolis, and Euler forces due to the angular rotation of the centrifuge. Assuming that the centrifuge operates at a constant angular velocity, the Euler force is considered absent.

Typical instability may arise when there is an external source supplying energy to the system (here, due to the angular velocity of the centrifuge) and the forces acting on the structure depend on any of the displacement fields of the structure. When the system is perturbed from its equilibrium position, different types of instability may emerge. Classical Euler Buckling is a well-known instability where the effective stiffness of the system turns negative and the system can no longer hold the load. Galloping form of instability occurs when the energy source can induce negative effective damping in the system, leading to energy accumulation. (Physical) Flutter type of instability can happen due to the coupling of displacement fields in their governing equations, even when the effective damping of the system is positive. Gyroscopic instability can emerge due to translating mass, even though there is no damping in the system, which results in odd time derivatives in the equations of motion (EOMs). It is essential for the small-scale model to remain stable during the centrifuge operation to obtain meaningful results and to understand the behaviour of the prototype.

Previous studies ([4], [8], [9], [13], [16], [17]) have focused on deriving the EOMs for a cantilever beam, fixed on one end and free on the other, rotating about a vertical axis about its fixed end. Such models typically represent wind turbine blades, where the angular velocity induces centrifugal forces that cause tension in the beam. A new dynamic modelling method was also proposed in these studies to derive the non-linear coupled EOMs, which are then linearized. These studies have examined free vibration characteristics, the onset of instability, and the effects of coupling terms, centrifugal stiffening, and centrifugal inertia forces.

## 1.2. Aim and Scope

The main objective of this research is to investigate the stability of a dynamically sensitive small-scale model, such as a monopile-founded OWT, when tested inside a geotechnical centrifuge and to identify the conditions under which the current approach of using simplified scaling laws is valid for such slender structures. This involves deriving the governing EOMs of the small-scale model and incorporating relevant pseudo forces, coupling terms, and boundary and interface conditions such that the mathematical model represents the small-scale model of an OWT within the centrifuge. This research focuses on identifying the angular velocity of the centrifuge at which the small-scale beam model may become unstable, examining potential instability phenomena such as divergence and flutter, and analysing the factors influencing such instabilities. Ultimately, these findings are applied to analyse the instability criteria for the small-scale model of real-life wind turbines using a case study.

This research analyses the small-scale model of a monopile-founded OWT, which is a dynamically sensitive structure, as a linear-elastic, homogeneous Rayleigh beam with a uniform and doubly symmetric cross-section along the length. The effect of rotational inertia of the cross-section is also considered. First, the beam is modeled as a cantilever beam with a fixed end and carrying a tip mass on the other end. Next, the interaction with soil is considered through a lumped spring model instead of a fixed end. The angular velocity of rotation is considered around only the vertical axis. Since the linear regime of the structure is considered, only the onset of instability can be analysed. To examine the amplitude of vibration post-instability, a non-linear analysis needs to be performed, which is beyond the scope of this research. Note that the damping in the structure is neglected.

## 1.3. Research Methodology

The primary aim of this research is to derive the mathematical model of a small-scale beam tested inside a centrifuge using a mathematically rigorous approach and to investigate the potential instability mechanisms that may arise when the relevant pseudo-forces and coupling terms are considered. The results can then be used to determine the conditions under which current simplified scaling laws are applicable. To systematically explore the problem, the following sub-questions are formulated:

1) Derive the governing EOMs for the axial and bending vibrations of the small-scale model, considering relevant pseudo forces and coupling of DOFs, for the following cases:
   a) Cantilever beam with a tip mass at the free end and clamped at the base, as shown in Fig.1.1a.
   b) Cantilever beam with a tip mass at the free end with SSI modeled via lumped springs at the base, as shown in Fig.1.1b.
2) Perform an eigenvalue analysis using the derived EOMs to calculate eigenfrequencies and mode shapes via:
   a) Analytical approach - using Assumed Modes Method(AMM), including convergence study
   b) Numerical approach
3) Identify possible instability mechanisms, such as divergence and flutter, by analysing the eigenproperties of the system:
   a) Determine how parameters (such as angular velocity and slenderness ratio) influence the onset of instability.
   b) Analyse the contribution of each term in the equations of motion to overall stability.
4) Apply the mathematical model to perform stability analysis of a small-scale model of an OWT tested inside the centrifuge facility at ETH Zürich, as a part of the research project, DONISIS project [3], led by TU Delft.

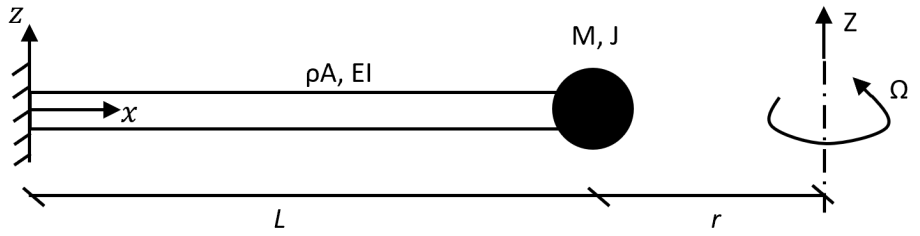


**(a)** With clamped end

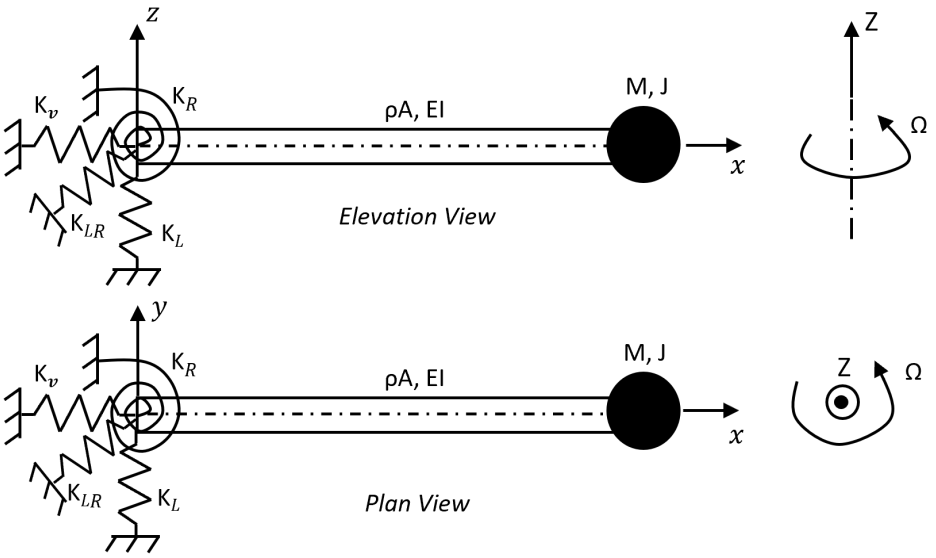


**(b)** With lumped springs

**Figure 1.1:** Rotating cantilever beam models.

## 1.4. Literature Review

Kane, Ryan & Banerjee [1987] [8] studied the dynamics of a cantilever beam attached to a rigid base that is undergoing a prescribed translational and rotational motion as shown in Fig. 1.2 and presented an algorithm to predict the response of the beam. Each point in the beam can undergo three translations and three rotations, resulting in a total of six DOFs, which include extension, bending in two planes, torsion, shear, and warping. In addition, the hub to which the beam is attached can undergo three translational and three rotational motions. Using the separation of variables technique, the DOFs are expressed as a summation of the product of modal functions and modal coordinates, with the mode shapes derived from the corresponding non-rotating cantilever beam with its base fixed. Linearization is performed on the kinematic terms (modal coordinates) to consider small vibrations of all the DOFs.

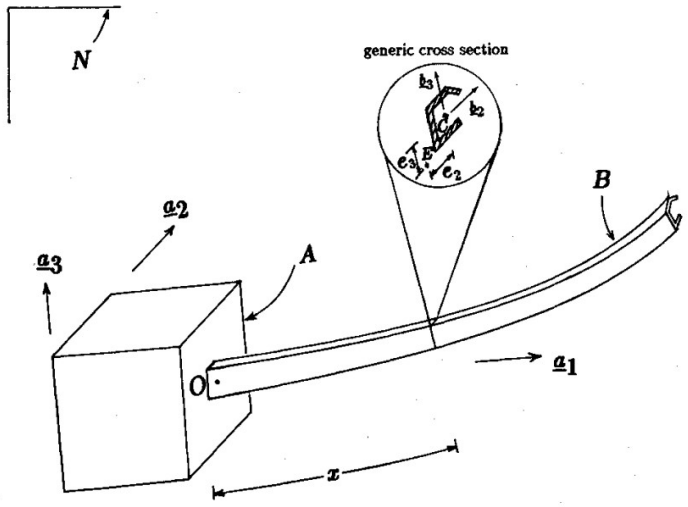


**Figure 1.2:** Beam attached to a moving rigid base [8]

The linear dynamical EOMs are generated from the strain energy function and generalized inertia force, considering the total velocity vector, including the effects of rotation. The modal representations of DOFs are substituted into the EOMs, and a matrix equation is generated after which the modal coordinates are solved numerically. The gyroscopic effect, centrifugal stiffening, and various other coupling effects are inherently considered while formulating the kinematic relations for deriving the EOMs. The authors provide an example of demonstrating how their approach to deriving the EOMs can show a system to be stable, while the conventional method would predict it as unstable.

H.H.Yoo & S.H.Shin [1998] [17] studied a specific case of Kane, Ryan & Banerjee [1987] [8] and formulated the equations of motion for the in-plane rotation of a straight cantilever beam (fixed on one end and free on the other end) as illustrated in Fig. 1.3 using a dynamic modelling method (DMM). The beam undergoes large overall motions due to the rotation as well as small strain elastic deformations. Three independent DOFs are considered, namely, stretch, flapwise, and chordwise deformations. The beam is modeled as a homogeneous, isotropic, and uniform Euler-Bernoulli beam. Linear equations of motion are derived, which suggest that the stretch and chordwise of the EOMs are coupled via a gyroscopic coupling term, while the flapwise EOM is independent.

Rayleigh-Ritz assumed mode method is used, wherein the DOFs are expressed as a summation of 'N' number of mode shapes that satisfy the boundary conditions multiplied by time-dependent modal coordinates. The EOMs are rewritten in the form of dimensionless parameters. The natural frequencies of the coupled EOMs are calculated by setting the determinant of the coefficient matrix of modal coordinates after writing the EOMs in state-space form, and the mode shapes are then determined. Convergence of natural frequencies is verified by increasing the number of considered modes to ten. The effects of centrifugal inertial force, the stiffening effect, and modal characteristics variation due to rotation are investigated. The effect of the gyroscopic term was studied as a function of angular velocity,

and phenomena such as veering, resonance, and divergence instability were also investigated.

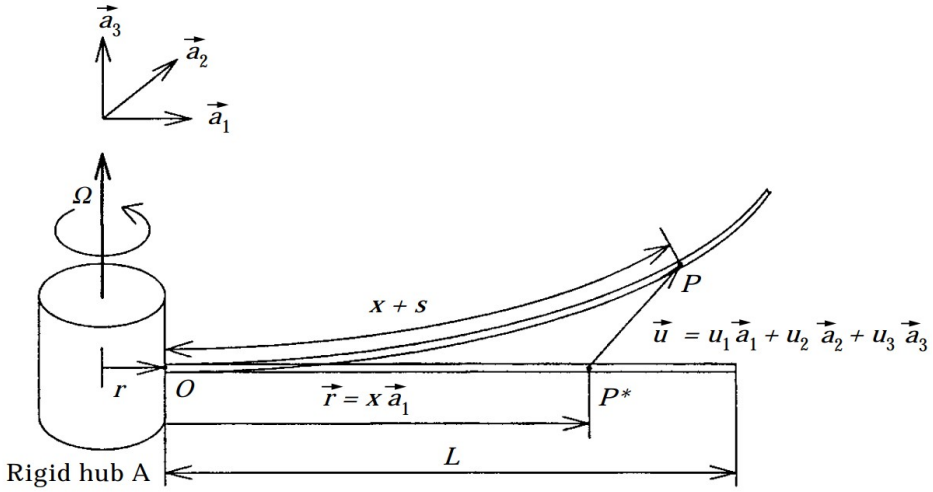


**Figure 1.3:** Configuration of rotating cantilever beam [16]

J.Chung & H.H.Yoo [2001] followed the same procedure as mentioned in the previous paragraph to derive the EOMs considering the same beam model. From the linearized EOMs, reduced forms are derived, and FEM is used instead of the Rayleigh-Ritz assumed mode method to calculate the natural frequencies by setting the external forces to zero. By setting the determinant to zero, the natural frequencies are calculated. Convergence of natural frequencies is verified by changing the number of elements. In addition, the natural frequencies are plotted against varying angular velocities to understand the divergence instability criteria and veering phenomenon. The stress distributions are drawn, and comparisons are made to a simple cantilever beam.

Existing studies mainly focus on deriving the EOMs of a cantilever beam fixed at one end and rotating about a vertical axis about its fixed end. These studies provide guidance on when to linearize the EOMs and how to calculate free vibration characteristics using various methods. Phenomena such as centrifugal stiffening, gyroscopic coupling, and motion-induced stiffness terms that may lead to the destabilisation of a rotating beam are explored. Furthermore, the predominant effect of angular velocity on the stability of the beam is well documented.

Although the literature provides insights into analysing stability and the parameters influencing it, the specific context of a rotating cantilever beam subjected to the conditions of a geotechnical centrifuge remains underexplored. For this case, a rigorous mathematical approach shall be adopted to consider all the relevant pseudo forces and coupling terms and then apply a proper method of linearization such that the stability of the beam can be analysed. Further, while centrifugal force induces tension when the beam rotates about its fixed end, the conditions within a centrifuge shift the rotation center, causing compression instead. This shift necessitates adjustments to the EOMs to accurately account for compression-induced effects.

## 1.5. Thesis Outline

This report begins in Chapter 1 with an introduction to centrifuge testing and its relevance for slender structures such as monopile-founded OWTs. The importance of stability of small-scale models inside the centrifuge and limitations of current experimental techniques and scaling laws for dynamically sensitive structures such as OWTs are highlighted, and a research gap is identified. The objectives, scope, and research methodology of this thesis are also presented. The chapter also reviews the existing literature on beams rotating about an axis at their fixed end, highlighting the methods used to derive and solve the governing equations of motion. Moreover, the types of structural instability and the influence of gyroscopic and centrifugal stiffening effects on instability are studied.

Chapter 2 develops the mathematical model of the rotating beam inside a centrifuge using Rayleigh beam theory and Lagrangian formalism. The kinematics of a rotating beam is introduced first, and the potential and kinetic energies are then formulated. The governing equations of motion are then derived using the Euler-Lagrange equations. The effect of SSI is included through a lumped spring model, and the EOMs are reformulated in dimensionless form.

The stability analysis is presented in Chapter 3, where both flapwise and chordwise motions are investigated. The concepts of divergence and flutter are explained, and the scope of instability is identified through a dispersion analysis. A parametric stability analysis is conducted using numerical techniques, and the influence of various parameters on the onset of instability is examined. Note that the effect of SSI is not considered in this chapter.

A practical application is given in Chapter 4, which presents a case study of a small-scale offshore wind turbine tested at the centrifuge facility of ETH Zürich. Analytical and numerical results for flapwise and chordwise stability are compared, and the influence of SSI is examined.

Finally, Chapter 5 concludes the thesis by summarizing the main findings. Divergence is identified as the dominant instability, while SSI has only a small effect compared to geometry and tip mass. Moreover, it is found that the Coriolis terms can be safely ignored for the range of parameters considered within this research. Recommendations for future research include extending the study to nonlinear behaviour, improving the small-scale model, and experimental validation.

# 2

# Equations of Motion

Three basic theories are commonly used to describe the transverse vibrations of beams: Euler-Bernoulli, Rayleigh, and Timoshenko. A detailed review of the existing beam theories is presented in [6]. Among these, the Euler-Bernoulli beam theory is the most widely adopted due to its mathematical simplicity and its ability to provide acceptable results for many engineering problems. Nevertheless, it usually overestimates natural frequencies, especially for higher modes. The Rayleigh beam theory improves on this by including the effect of rotational inertia, which partially reduces this overestimation. Among the three, the Timoshenko beam theory is the most accurate, as it also accounts for shear deformation, making it suitable for non-slender beams.

Since the small-scale model of a monopile-founded OWT considered in this study can be treated as a slender beam, the Rayleigh beam theory is adopted to derive the EOMs that govern the small vibrations of the beam. The motivation for this choice is to adopt the simplest beam model that can still capture the essential physics of stability. The Rayleigh beam model provides sufficient accuracy in predicting the lower natural frequencies while remaining less complex than the Timoshenko model, making it an appropriate and efficient choice for the present study.

This chapter presents the derivation of the governing EOMs using Rayleigh beam theory following Lagrangian formalism. First, the kinematics of a rotating beam are described in Section 2.1 using a non-inertial frame of reference, which introduces the relevant pseudo forces and coupling of displacement fields. Next, the potential and kinetic energies of the system are derived in sections 2.2 and 2.3, respectively, which together define the Lagrange function as shown in 2.4. Using this, the governing EOMs are then obtained by applying the Euler-Lagrange equations in Section 2.5, after which their dimensionless forms are formulated. Finally, the effect of SSI is included by means of a lumped spring model, and the corresponding modified boundary conditions are presented.

## 2.1. Kinematics

The configuration of the rotating beam is illustrated in Fig. 2.1. It is fixed at the base and carries a tip mass at the other end. The tip mass is idealized as a rigid point mass with mass $M$ and mass moment of inertia $J$. The beam is assumed to be homogeneous and linear-elastic with a uniform and doubly symmetric cross-section along its length. The length of the beam is denoted by $L$, and its cross-sectional area by $A$. The distance from the center of the centrifuge to the tip mass is $r$, and the centrifuge rotates with a constant angular velocity $\Omega$ about the $Z$ axis as shown in the Figure 2.1.

To describe the motion of any point in the beam, two frames of reference can be used. The first is an inertial frame of reference, $R_F(X, Y, Z)$, fixed in space with its origin $O'$ located at the center of the centrifuge. The second is a rotating local frame of reference, $R_L(x, y, z)$, which rotates along with the beam and has its origin $O$ at the fixed end. In the Fig. 2.1, plan views of the $R_F$ & $R_L$ frames of reference are shown. According to the right-hand thumb rule, the $Z$-axis of the $R_F$ is directed out of the page, and the same rule also applies to $R_L$.

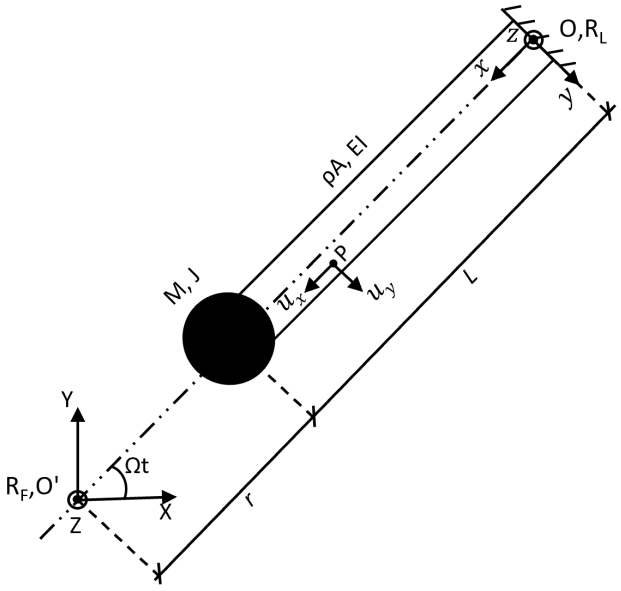


**Figure 2.1:** Schematic of a rotating cantilever beam tested inside a centrifuge

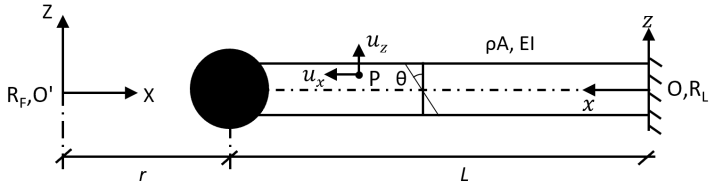


**(a)** Elevation view

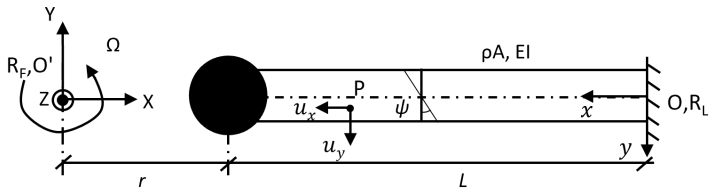


**(b)** Plan view

**Figure 2.2:** Rotating cantilever beam models showing rotation of cross-section.

The governing equations are derived in the rotating local frame of reference, $R_L$. Any arbitrary point $P$ within the beam consists of three translational displacements, $u_x$, $u_y$, and $u_z$, which along the local $x$, $y$, and $z$ axes, respectively. These are expressed as

$$\begin{aligned} u_x(x,y,z,t) &= u(x,t) + z\,\theta(x,t) - y\,\psi(x,t) \\ &= u(x,t) - z\frac{\partial w(x,t)}{\partial x} - y\frac{\partial v(x,t)}{\partial x} \\ u_y(x,y,z,t) &= v(x,t) \\ u_z(x,y,z,t) &= w(x,t) \end{aligned}$$

Here, $u(x,t)$, $v(x,t)$, and $w(x,t)$ represent the displacements of a point on the centroidal axis of the undeformed beam, located at a distance $x$ from the fixed end. These displacements are along the local $x$, $y$, and $z$ axes, respectively. The terms $\theta(x,t)$ and $\psi(x,t)$ denote the slope of the centroidal axis of the beam in $yz$ and $xy$ planes, respectively, as shown in Fig. 2.2. According to the Rayleigh beam

theory, the slopes are related to the corresponding transverse displacements as

$$\psi(x,t) = \frac{\partial v(x,t)}{\partial x} \quad \text{and} \quad \theta(x,t) = -\frac{\partial w(x,t)}{\partial x}$$

## 2.2. Potential Energy

For small strains, the general nonlinear expression of the axial strain is given by the Green–Lagrange formulation as

$$\varepsilon_{xx} = u_{x,x} + \frac{1}{2}(u_{x,x}^2 + u_{y,x}^2 + u_{z,x}^2)$$

where the subscript notation denotes partial differentiation. For example,

$$u_{y,x} = \frac{\partial u_y}{\partial x}$$

Hence, the total strain energy is given by

$$\frac{1}{2}\, E \int_V \varepsilon_{xx}^2 dV$$

where $E$ is the Young's modulus of the material of the beam and $V$ is the volume of the beam. This expression accounts for both axial and bending deformations of the beam. By substituting the Green-Lagrange formulation into the above equation and integrating over the cross-sectional area, the total strain energy due to axial and bending deformations is obtained. The following standard integral relations for the cross-sectional area are utilized,

$$\int dA = A,\ \int y\ dA = 0,\ \int z\ dA = 0,\ \int y^2\, dA = I_z,\ \int z^2\, dA = I_y,\ \int y\, z\, dA = I_{yz} = 0$$

Here, $I_y$ and $I_z$ represent the second moments of inertia of the section about the local $y$ and $z$ axes, respectively. Since the cross-section of the beam is assumed to be symmetric, $I_{yz}$ is zero.

The resulting strain energy is

$$\int_0^L \left(\frac{1}{2}EA(u_{,x})^2 + \frac{1}{2}EI_z(v_{,xx})^2 + \frac{1}{2}EI_y(w_{,xx})^2\right) dx \tag{2.1}$$

Note that the higher-order terms are neglected in the strain energy formulation. It is essential that linearization is applied at a stage where the resulting governing equations still retain the terms responsible for instability. Performing the linearization at this stage yields the same governing equations as when it is carried out at the final stage after deriving full nonlinear set of EOMs. The complete nonlinear potential energy expression and the corresponding nonlinear equations of motion are provided in Appendix D.

The first term in Eq. (2.1) corresponds to the strain energy due to axial deformation, while the second and third terms represent the strain energy associated with bending deformations along lateral and vertical directions.

Let $T(x)$ be the axial compression force in the beam acting along the centroid of the cross section. $T(x)$ is assumed to be positive and needs to be solved from the static equilibrium of the axial motion. The potential energy due to $T(x)$ is given by:

$$\int_0^L \left(-\frac{1}{2}T(x)(v_{,x})^2 - \frac{1}{2}T(x)(w_{,x})^2\right) dx$$

Combining the strain energy and the contribution from axial forces, the total potential energy of the system can be expressed as

$$P = \int_0^L \left(\frac{1}{2}EA(u_{,x})^2 + \frac{1}{2}EI_z(v_{,xx})^2 dx + \frac{1}{2}EI_y(w_{,xx})^2 - \frac{1}{2}T(x)(v_{,x})^2 - \frac{1}{2}T(x)(w_{,x})^2\right) dx \tag{2.2}$$

## 2.3. Kinetic Energy

Consider an arbitrary point, $P$, inside the beam as shown in Fig. 2.1. Before deformation, the position vector of $P$ within the frame of reference, $R_L$, is given by $\overrightarrow{OP}_0 = \{x, y, z\}^T$. After deformation, the position vector within $R_L$ becomes $\overrightarrow{OP} = \{x + u_x, y + u_y, z + u_z\}^T$. So, the displacement vector of $P$ may be expressed as

$$\mathbf{u} = \overrightarrow{OP} - \overrightarrow{OP}_0 = \begin{Bmatrix} u_x \\ u_y \\ u_z \end{Bmatrix}$$

where, $u_x$, $u_y$, and $u_z$ are the displacements of point $P$ along the local $x$, $y$, and $z$ axes, respectively. Differentiating this displacement vector with respect to time gives the local velocity of $P$ in $R_L$,

$$\dot{\mathbf{u}} = \begin{Bmatrix} \dot{u}_x \\ \dot{u}_y \\ \dot{u}_z \end{Bmatrix} = \begin{Bmatrix} \dot{u} + z\dot{\theta} - y\dot{\psi} \\ \dot{v} \\ \dot{w} \end{Bmatrix}$$

where an overdot denotes differentiation with respect to time, i.e.,

$$\dot{u}_x = \frac{\partial u_x}{\partial t}$$

Since the beam rotates with angular velocity $\Omega$ about the $Z$ axis of the inertial frame of reference, $R_F$, the position of $P$ after deformation in $R_F$ can be written as

$$\overrightarrow{O'P} = \begin{Bmatrix} (r + L - x - u_x)\cos(\Omega t) + (y + u_y)\sin(\Omega t) \\ (r + L - x - u_x)\cos(\Omega t) - (y + u_y)\sin(\Omega t) \\ z + u_z \end{Bmatrix}$$

where $\Omega t$ is the angle made by the undeformed beam with respect to the $X$ axis of $R_F$.

The linear velocity of point $P$ within the $R_F$ due to the angular velocity is obtained by the cross product of the angular velocity vector and the position vector of $P$,

$$\begin{aligned} \begin{Bmatrix} v_X^\Omega \\ v_Y^\Omega \\ v_Z^\Omega \end{Bmatrix} &= \begin{Bmatrix} 0 \\ 0 \\ \Omega \end{Bmatrix} \times \begin{Bmatrix} (r + L - x - u_x)\cos\Omega t + (y + u_y)\sin\Omega t \\ (r + L - x - u_x)\sin\Omega t - (y + u_y)\cos\Omega t \\ z + u_z \end{Bmatrix} \\ &= \begin{Bmatrix} -\Omega\left[(r + L - x - u_x)\sin\Omega t - (y + u_y)\cos\Omega t\right] \\ \Omega\left[(r + L - x - u_x)\cos\Omega t + (y + u_y)\sin\Omega t\right] \\ 0 \end{Bmatrix} \end{aligned}$$

This velocity vector is along the $X, Y$, and $Z$ axes of $R_F$. Therefore, the linear velocities along the local $x, y, z$ axes within the $R_L$ are obtained by resolving this velocity vector

$$\mathbf{v}^\Omega = \begin{Bmatrix} v_x^\Omega \\ v_y^\Omega \\ v_z^\Omega \end{Bmatrix} = \begin{Bmatrix} -\left[v_X^\Omega \cos\Omega t + v_Y^\Omega \sin\Omega t\right] \\ \left[v_X^\Omega \sin\Omega t - v_Y^\Omega \cos\Omega t\right] \\ v_Z^\Omega \end{Bmatrix} = \begin{Bmatrix} -\Omega(y + u_y) \\ -\Omega(r + L - x - u_x) \\ 0 \end{Bmatrix}$$

The total velocity vector, $\mathbf{v}_P$, of point $P$ in the rotating frame of reference, $R_L$, is therefore the sum of

the local velocity, $\dot{\mathbf{u}}$, and the contribution due to angular velocity, $\mathbf{v}^{\Omega}$,

$$\begin{aligned}
\mathbf{v}_P &= \begin{Bmatrix} \dot{u} + z\dot{\theta} - y\dot{\psi} \\ \dot{v} \\ \dot{w} \end{Bmatrix} + \begin{Bmatrix} -\Omega(y + u_y) \\ -\Omega(r + L - x - u_x) \\ 0 \end{Bmatrix} \\
&= \begin{Bmatrix} \dot{u} + z\dot{\theta} - y\dot{\psi} - \Omega(y + v) \\ \dot{v} - \Omega(r + L - x - u - z\theta + y\psi) \\ \dot{w} \end{Bmatrix} \\
&= \begin{Bmatrix} \dfrac{\partial u(x,t)}{\partial t} - z\dfrac{\partial^2 w(x,t)}{\partial x \partial t} - y\dfrac{\partial^2 v(x,t)}{\partial x \partial t} - \Omega(y + v(x,t)) \\ \dfrac{\partial v(x,t)}{\partial t} - \Omega\left[r + L - x - u(x,t) + z\dfrac{\partial w(x,t)}{\partial x} + y\frac{\partial v(x,t)}{\partial x}\right] \\ \dfrac{\partial w(x,t)}{\partial t} \end{Bmatrix} \\
&= \begin{Bmatrix} u_{,t} - zw_{,xt} - yv_{,xt} - \Omega(y + v) \\ v_{,t} - \Omega\left[r + L - x - u + zw_{,x} + yv_{,x}\right] \\ w_{,t} \end{Bmatrix}
\end{aligned}$$

Therefore, Kinetic energy of the system is given by

$$\begin{aligned}
K =& \frac{1}{2}\,\rho \int_V \mathbf{v}_P \cdot \mathbf{v}_P \, dV \\
=& \frac{1}{2}\int_V \rho \left(u_{,t} - zw_{,xt} - yv_{,xt} - \Omega(y + v)\right)^2 dV + \\
& \frac{1}{2}\int_V \rho \left(v_{,t} - \Omega\left(r + L - x - u + zw_{,x} + yv_{,x}\right)\right)^2 dV + \frac{1}{2}\int_V \rho \left(w_{,t}\right)^2 dV
\end{aligned}$$

where $\rho$ is the mass density of the material.

Expanding the kinetic energy and utilizing the following standard integral relations for the cross-sectional area presented before, the expression for the total kinetic energy is obtained.

$$\begin{aligned}
K = \int_0^L \Big[ & \frac{1}{2}\rho A(u_{,t})^2 + \frac{1}{2}\rho I_y (w_{,xt})^2 + \frac{1}{2}\rho I_z (v_{,xt})^2 + \rho I_{yz} w_{,xt} v_{,xt} \\
& + \frac{1}{2}\rho A\Omega^2 v^2 - \rho A\Omega v u_{,t} + \rho I_{yz}\Omega w_{,xt} + \rho I_z \Omega v_{,xt} \\
& + \frac{1}{2}\rho A(v_{,t})^2 + \frac{1}{2}\rho A\Omega^2 u^2 + \frac{1}{2}\rho I_y \Omega^2 (w_{,x})^2 + \frac{1}{2}\rho I_z \Omega^2 (v_{,x})^2 + \rho I_{yz}\Omega^2 (w_{,x})(v_{,x}) \\
& - \rho A\Omega(r + L - x)v_{,t} + \rho A\Omega u v_{,t} - \rho A\Omega^2 (r + L - x)u + \frac{1}{2}\rho A (w_{,t})^2 \Big] dx
\end{aligned} \tag{2.3}$$

## 2.4. Lagrange Function

The Lagrange function, $L$, of a system is defined as the difference between the kinetic energy, $K$, and potential energy, $P$, of the system, at any given instant of time. For a continuous system such as a beam, it is convenient to work with the linear density of the Lagrange function, denoted by $\lambda$, which represents the Lagrangian per unit length of the beam. Mathematically, this is expressed as

$$L = K - P = \int_0^L \lambda \, dx$$

By substituting the expressions for kinetic energy and potential energy derived in Sections 2.2 and 2.3, the linear density of the Lagrange function of the beam is obtained as

$$\begin{aligned}\lambda = &\frac{1}{2}\rho A(u_{,t})^2 + \frac{1}{2}\rho I_y(w_{,xt})^2 + \frac{1}{2}\rho I_z(v_{,xt})^2 + \rho I_{yz}w_{,xt}v_{,xt} \\ &+ \frac{1}{2}\rho A\Omega^2 v^2 - \rho A\Omega v u_{,t} + \rho I_{yz}\Omega w_{,xt} + \rho I_z\Omega v_{,xt} \\ &+ \frac{1}{2}\rho A(v_{,t})^2 + \frac{1}{2}\rho A\Omega^2 u^2 + \frac{1}{2}\rho I_y\Omega^2(w_{,x})^2 + \frac{1}{2}\rho I_z\Omega^2(v_{,x})^2 + \rho I_{yz}\Omega^2(w_{,x})(v_{,x}) \\ &- \rho A\Omega(r+L-x)v_{,t} + \rho A\Omega u v_{,t} - \rho A\Omega^2(r+L-x)u + \frac{1}{2}\rho A(w_{,t})^2 \\ &- \frac{1}{2}EA(u_{,x})^2 - \frac{1}{2}EI_z(v_{,xx})^2 - \frac{1}{2}EI_y(w_{,xx})^2 + \frac{1}{2}T(x)(v_{,x})^2 + \frac{1}{2}T(x)(w_{,x})^2\end{aligned} \tag{2.4}$$

Here, the subscript notation denotes partial derivatives. For example,

$$u_{,x} = \frac{\partial u}{\partial x}, \quad v_{,t} = \frac{\partial v}{\partial t}, \quad w_{,xt} = \frac{\partial^2 w}{\partial x \partial t}$$

In addition to the beam, the system includes an end attachment in the form of a concentrated tip mass $M$ with mass moment of inertia $J$. This tip mass influences the dynamics of the beam and must therefore be included in the Lagrangian formulation. The tip mass is located at the free end of the beam, whose position vector in the local rotating frame $R_L$ is given by $\{L, 0, 0\}^T$. After deformation, its velocity vector in $R_L$, including the effect of angular velocity, is expressed as

$$\begin{Bmatrix} u_{,t} - \Omega v \\ v_{,t} - \Omega\,(r-u) \\ w_{,t} \end{Bmatrix}$$

Accordingly, the Lagrangian contribution of the end attachment, denoted by $L_b$, can be written as

$$L_b = \frac{1}{2}M\left[u_{,t} - \Omega v\right]^2 + \frac{1}{2}M\left[v_{,t} - \Omega(r-u)\right]^2 + \frac{1}{2}M(w_{,t})^2 + \frac{1}{2}J(v_{,xt})^2 + \frac{1}{2}J(w_{,xt})^2 \tag{2.5}$$

The first three terms in the above expression represent the translational kinetic energy of the tip mass along the $x$, $y$, and $z$ directions, respectively, while the last two terms account for the rotational kinetic energy of the attachment about the transverse axes, $y$, and $z$, respectively.

## 2.5. Euler-Lagrange Equations

The governing equations of motion and associated boundary conditions are obtained by applying the Euler–Lagrange equations to the Lagrangian density $\lambda$ derived in Section 2.4. The general form of the Euler–Lagrange equations for a field variable $w(x,t)$, as derived in appendix A, is recalled here for completeness:

Equation of Motion:

$$\frac{\partial \lambda}{\partial w} - \frac{\partial}{\partial t}\left(\frac{\partial \lambda}{\partial w_{,t}}\right) - \frac{\partial}{\partial x}\left(\frac{\partial \lambda}{\partial w_{,x}}\right) + \frac{\partial^2}{\partial x^2}\left(\frac{\partial \lambda}{\partial w_{,xx}}\right) + \frac{\partial^2}{\partial x \partial t}\left(\frac{\partial \lambda}{\partial w_{,xt}}\right) = 0$$

Natural Boundary Conditions (NBCs):

At $x = 0$ (left end):

$$-\frac{\partial \lambda}{\partial w_{,x}} + \frac{\partial}{\partial x}\left(\frac{\partial \lambda}{\partial w_{,xx}}\right) + \frac{\partial}{\partial t}\left(\frac{\partial \lambda}{\partial w_{,xt}}\right) + \frac{\partial L_{aw}}{\partial w(a,t)} - \frac{\partial}{\partial t}\left(\frac{\partial L_{aw}}{\partial w_{,t}(a,t)}\right) = 0$$

$$-\frac{\partial \lambda}{\partial w_{,xx}} + \frac{\partial L_{a\varphi}}{\partial w_{,x}(a,t)} - \frac{\partial}{\partial t}\left(\frac{\partial L_{a\varphi}}{\partial w_{,xt}(a,t)}\right) = 0$$

At $x = L$ (right end):

$$\frac{\partial \lambda}{\partial w_{,x}} - \frac{\partial}{\partial x}\left(\frac{\partial \lambda}{\partial w_{,xx}}\right) - \frac{\partial}{\partial t}\left(\frac{\partial \lambda}{\partial w_{,xt}}\right) + \frac{\partial L_{bw}}{\partial w(b,t)} - \frac{\partial}{\partial t}\left(\frac{\partial L_{bw}}{\partial w_{,t}(b,t)}\right) = 0$$

$$\frac{\partial \lambda}{\partial w_{,xx}} + \frac{\partial L_{b\varphi}}{\partial w_{,x}(b,t)} - \frac{\partial}{\partial t}\left(\frac{\partial L_{b\varphi}}{\partial w_{,xt}(b,t)}\right) = 0$$

Since each point in the beam can undergo three displacements, $u$, $v$, and $w$, the Euler–Lagrange equations must be applied once for each displacement field. By doing so, the following governing EOMs are obtained for the configuration shown in Fig. 2.1:

$$\rho A\frac{\partial^2 u}{\partial t^2} - 2\rho A\Omega\frac{\partial v}{\partial t} - EA\frac{\partial^2 u}{\partial x^2} - \rho A\Omega^2 u = -\rho A\Omega^2(r + L - x) \tag{2.6a}$$

$$\rho A\frac{\partial^2 v}{\partial t^2} + 2\rho A\Omega\frac{\partial u}{\partial t} + EI_z\frac{\partial^4 v}{\partial x^4} + \rho I_z\Omega^2\frac{\partial^2 v}{\partial x^2} + \frac{\partial}{\partial x}\left[T(x)\frac{\partial v}{\partial x}\right] - \rho I_z\frac{\partial^4 v}{\partial x^2\partial t^2} - \rho A\Omega^2 v = 0 \tag{2.6b}$$

$$\rho A\frac{\partial^2 w}{\partial t^2} + EI_y\frac{\partial^4 w}{\partial x^4} + \rho I_y\Omega^2\frac{\partial^2 w}{\partial x^2} + \frac{\partial}{\partial x}\left[T(x)\frac{\partial w}{\partial x}\right] - \rho I_y\frac{\partial^4 w}{\partial x^2\partial t^2} = 0 \tag{2.6c}$$

where $T(x)$ denotes the axial compression force in the beam, which needs to be solved from the static equilibrium of axial motion.

The above equations represent the balance of forces acting on any differential element along the beam along $x, y, z$ directions. Note that Eq. (2.6a) and Eq. (2.6b) represent axial and lateral bending motions respectively and are coupled through the velocity-dependent Coriolis terms, ($-2\rho A\Omega\frac{\partial v}{\partial t}$ and $2\rho A\Omega\frac{\partial u}{\partial t}$). Together, these two equations describe the **chordwise motion** of the beam. Eq. (2.6c), on the other hand, is decoupled and describes the vertical bending motion of the beam, and is termed as **flapwise motion**. The EOM along the axial direction, Eq. (2.6a), includes both static and dynamic components of the axial displacement, whereas the EOMs along the transverse directions include only the dynamic part.

The corresponding boundary conditions can be classified into those at the fixed end ($x = 0$) and those at the free end with the tip mass ($x = L$). At the fixed end ($x = 0$), the displacements and the slopes are set to zero:

$$u(x,t)\big|_{x=0} = 0, \quad v(x,t)\big|_{x=0} = 0, \quad \left.\frac{\partial v(x,t)}{\partial x}\right|_{x=0} = 0, \quad w(x,t)\big|_{x=0} = 0, \quad \left.\frac{\partial w(x,t)}{\partial x}\right|_{x=0} = 0 \tag{2.7}$$

At the free end with tip mass ($x = L$), the boundary conditions should account for the inertia of the tip mass $M$ and its rotational inertia $J$. These conditions are obtained by applying the natural boundary conditions of Euler-Lagrange equations:

$$M\frac{\partial^2 u}{\partial t^2} - 2M\Omega\frac{\partial v}{\partial t} + EA\frac{\partial u}{\partial x} - M\Omega^2 u = -M\Omega^2 r \tag{2.8a}$$

$$M\frac{\partial^2 v}{\partial t^2} + 2M\Omega\frac{\partial u}{\partial t} - EI_z\frac{\partial^3 v}{\partial x^3} - M\Omega^2 v - T(L)\frac{\partial v}{\partial x} - \rho I_z\Omega^2\frac{\partial v}{\partial x} + \rho I_z\frac{\partial^3 v}{\partial x\partial t^2} = 0 \tag{2.8b}$$

$$-EI_z\frac{\partial^2 v}{\partial x^2} - J\frac{\partial^3 v}{\partial x\partial t^2} = 0 \tag{2.8c}$$

$$M\frac{\partial^2 w}{\partial t^2} - EI_y\frac{\partial^3 w}{\partial x^3} - T(L)\frac{\partial w}{\partial x} - \rho I_y\Omega^2\frac{\partial w}{\partial x} + \rho I_y\frac{\partial^3 w}{\partial x\partial t^2} = 0 \tag{2.8d}$$

$$-EI_y\frac{\partial^2 w}{\partial x^2} - J\frac{\partial^3 w}{\partial x\partial t^2} = 0 \tag{2.8e}$$

Note that, similar to the governing equations (2.6a) and (2.6b), the axial boundary condition, (2.8a) and the lateral shear boundary condition, (2.8b) are coupled through the Coriolis terms, ($-2M\Omega\frac{\partial v}{\partial t}$ and $2M\Omega\frac{\partial u}{\partial t}$), which represent the Coriolis forces acting on the tip mass.

The next step is to derive an expression for the axial compression force, $T(x)$, along the beam by solving the static equilibrium of the axial EOM. For this, the total axial displacement is decomposed into two parts, a static component, $u_0(x)$, and a dynamic component, $u_d(x,t)$. The static part accounts for the mean displacement caused by centrifugal forces acting along the axial direction, while the dynamic part accounts for the time-dependent displacements due to vibration. This decomposition can be written as

$$u(x,t) = u_0(x) + u_d(x,t), \tag{2.9}$$

By substituting $u(x,t) = u_0(x)$ into Eq. (2.6a), the time-dependent terms drop out, and the equations describing the static equilibrium of the axial forces are obtained. Note that the partial derivative is now replaced by an ordinary derivative as the equations depend only on the spatial variable $x$.

$$-EA\frac{d^2u_0}{dx^2} = -\rho A\Omega^2(r + L - x - u_0)$$

By substituting $u(x,t) = u_0(x)$ into Eq. 2.7 and Eq. 2.8a, the associated boundary conditions for the static equilibrium for the axial direction are obtained.

$$u_0(0) = 0 \quad \text{and} \quad EA\,\frac{du_0}{dx}\bigg|_{x=L} = -M\Omega^2\big(r - u_0(L)\big).$$

At the free end, the displacement $u_0(L)$ is typically much smaller than the centrifuge radius $r$. By neglecting $u_0$ in comparison to $r$, the governing equation simplifies to

$$-EA\frac{d^2u_0}{dx^2} = -\rho A\Omega^2(r + L - x) \tag{2.10}$$

with boundary conditions,

$$u_0(0) = 0 \quad \text{and} \quad EA\,\frac{du_0}{dx}\bigg|_{x=L} = -M\Omega^2 r. \tag{2.11}$$

Solving the above system of equations, (2.10) and (2.11), gives the following expression for axial compression force:

$$T(x) = Mr\Omega^2 + \rho A\Omega^2\left[(r+L)(L-x) - \left(\frac{L^2 - x^2}{2}\right)\right] \tag{2.12}$$

This expression shows that the axial compression has two main contributions: a constant term, $Mr\Omega^2$, due to the centrifugal force acting on the tip mass, and a quadratic term, due to the centrifugal force acting on the distributed mass of the beam. Note that $T(x)$ is assumed to be constant over time, neglecting any fluctuations due to dynamic oscillations of the beam along the axial direction.

Substituting (2.9) into Eq. (2.6a) and Eq. (2.8a) gives the governing equations for axial motion:

$$\rho A\frac{\partial^2 u_d}{\partial t^2} - 2\rho A\Omega\frac{\partial v}{\partial t} - EA\frac{\partial^2 u_d}{\partial x^2} - \rho A\Omega^2 u_d = 0 \tag{2.13}$$

with the following boundary conditions

$$\text{At } x = 0\text{:} \quad u_d = 0 \tag{2.14a}$$

$$\text{At } x = L\text{:} \quad M\frac{\partial^2 u_d}{\partial t^2} - 2M\Omega\frac{\partial v}{\partial t} + EA\frac{\partial u_d}{\partial x} - M\Omega^2 u_d = 0 \tag{2.14b}$$

Note that the subscript $d$ will be omitted for brevity for future representations. Eq. (2.13) describes the small vibrations of any differential element within the beam along the axial direction about its static equilibrium.

## 2.6. Soil-Structure Interaction

The properties of the soil supporting an OWT play a key role in its performance. Over their lifetime, OWTs are exposed to repeated cyclic and dynamic loads, such as wind and wave actions. These loads are transferred to the soil and can gradually change the soil properties around the OWT. As a result, the stiffness of the foundation may vary, which directly influences the natural frequencies of the OWT. The current design process normally ensures that the natural frequencies of the OWT lie outside the excitation frequency range of external loads.

To understand the influence of SSI, the OWT and its supporting soil are represented by a small-scale model tested in a centrifuge. It is therefore important to investigate how variations in soil stiffness affect the stability of the small-scale model and to determine whether these changes in stiffness have a significant impact on the model's stability.

Several models exist in the literature to mathematically account for the effect of SSI. In this study, the so-called lumped spring model [14] is adopted, which is based on the monopile head stiffness at the mudline level where the foundation is modeled using four point springs as shown in Fig. 1.1b. For simplicity, the stiffness of the soil is assumed to be axisymmetric. This assumption implies that the two cross-coupling springs are assigned the same stiffness, and the two lateral springs in orthogonal directions also have the same value. Similarly, the rotational springs are considered identical in both planes. This simplification reduces the number of independent soil parameters. The expressions used for calculating the spring stiffness values are provided in Appendix B.

The boundary conditions at the base are modified from the fixed-end conditions discussed in the previous section, following the analytical framework of [2]. They are expressed as:

$$EA\frac{\partial u}{\partial x} - K_v u = 0 \tag{2.15a}$$

$$-EI_z\frac{\partial^3 v}{\partial x^3} - T(0)\frac{\partial v}{\partial x} - \rho I_z\Omega^2\frac{\partial v}{\partial x} + \rho I_z\frac{\partial^3 v}{\partial x \partial t^2} - K_L v - K_{LR}\frac{\partial v}{\partial x} = 0 \tag{2.15b}$$

$$-EI_z\frac{\partial^2 v}{\partial x^2} + K_R\frac{\partial v}{\partial x} + K_{LR}v = 0 \tag{2.15c}$$

$$-EI_y\frac{\partial^3 w}{\partial x^3} - T(0)\frac{\partial w}{\partial x} - \rho I_y\Omega^2\frac{\partial w}{\partial x} + \rho I_y\frac{\partial^3 w}{\partial x \partial t^2} - K_L w - K_{LR}\frac{\partial w}{\partial x} = 0 \tag{2.15d}$$

$$-EI_y\frac{\partial^2 w}{\partial x^2} + K_R\frac{\partial w}{\partial x} + K_{LR}w = 0 \tag{2.15e}$$

Here, $K_v$ denotes the axial spring stiffness, $K_L$ the transverse spring stiffness, $K_R$ the rotational spring stiffness, and $K_{LR}$ the coupling stiffness between lateral displacement and rotation.

## 2.7. Dimensionless Equations of Motion

In order to simplify the governing equations and reduce the number of independent parameters, the system of equations derived earlier is reformulated in a dimensionless form. This reformulation not only makes the equations more compact but also allows general conclusions to be drawn from the numerical results, independent of the specific geometry or material properties of a particular system.

To achieve this, the following dimensionless spatial coordinate, time, and displacement variables are introduced:

$$\zeta = \frac{x}{h},\ \ \tau = t\omega_0,\ \ \tilde{u} = \frac{u}{h},\ \ \tilde{v} = \frac{v}{h},\ \ \tilde{w} = \frac{w}{h},\ \ \tilde{r} = \frac{r}{h},\ \ \tilde{L} = \frac{L}{h} \tag{2.16}$$

In addition, the following parameters are introduced to represent dimensionless angular velocity, slenderness ratio, dimensionless tip mass, and dimensionless mass moment of inertia of the tip mass

$$\gamma = \frac{\Omega}{\omega_0},\ \ \lambda^2 = \frac{Ah^2}{I},\ \ \tilde{M} = \frac{M}{\rho Ah},\ \ \tilde{J} = \frac{J}{\rho Ah^3} \tag{2.17}$$

Note that for doubly symmetric cross-sections, $I_y = I_z = I$ is used. Finally, the stiffnesses of the soil springs are expressed in a dimensionless form, which enables direct comparison across different soil conditions:

$$\eta_L = \frac{K_L h^3}{EI},\ \eta_R = \frac{K_R h}{EI},\ \eta_{LR} = \frac{K_{LR} h^2}{EI},\ \eta_V = \frac{K_V h}{EA} \tag{2.18}$$

where $EI$ is the flexural rigidity of the beam.

The values of $h$ and $\omega_0$ appearing in the above equations can be chosen arbitrarily, and the following definitions are adopted to obtain simplified dimensionless EOMs:

$$h = L \quad \text{and} \quad \omega_0^2 = \frac{E}{\rho h^2}$$

Substituting the above relations into the governing equations and performing basic rearrangements, the governing EOMs in their dimensionless form are obtained:

$$\frac{\partial^2 \tilde{u}}{\partial \tau^2} - 2\gamma \frac{\partial \tilde{v}}{\partial \tau} - \frac{\partial^2 \tilde{u}}{\partial \zeta^2} - \gamma^2 \tilde{u} = 0 \tag{2.19a}$$

$$\frac{\partial^2 \tilde{v}}{\partial \tau^2} + 2\gamma \frac{\partial \tilde{u}}{\partial \tau} + \frac{1}{\lambda^2}\frac{\partial^4 \tilde{v}}{\partial \zeta^4} + \frac{\gamma^2}{\lambda^2}\frac{\partial^2 \tilde{v}}{\partial \zeta^2} + \frac{\partial}{\partial \zeta}\left[T(\zeta)\frac{\partial \tilde{v}}{\partial \zeta}\right] - \frac{1}{\lambda^2}\frac{\partial^4 \tilde{v}}{\partial \zeta^2 \partial \tau^2} - \gamma^2 \tilde{v} = 0 \tag{2.19b}$$

$$\frac{\partial^2 \tilde{w}}{\partial \tau^2} + \frac{1}{\lambda^2}\frac{\partial^4 \tilde{w}}{\partial \zeta^4} + \frac{\gamma^2}{\lambda^2}\frac{\partial^2 \tilde{w}}{\partial \zeta^2} + \frac{\partial}{\partial \zeta}\left[T(\zeta)\frac{\partial \tilde{w}}{\partial \zeta}\right] - \frac{1}{\lambda^2}\frac{\partial^4 \tilde{w}}{\partial \zeta^2 \partial \tau^2} = 0 \tag{2.19c}$$

where the dimensionless axial compression force expressed as

$$T(\zeta) = \tilde{M}\tilde{r}\gamma^2 + \gamma^2\left[(\tilde{r} + \tilde{L})(\tilde{L} - \tilde{\zeta}) - \left(\frac{\tilde{L}^2 - \tilde{\zeta}^2}{2}\right)\right] \tag{2.20}$$

The boundary conditions at the fixed end $(\zeta = 0)$ in their dimensionless form are:

$$\tilde{u}(\zeta,\tau)\big|_{\zeta=0} = 0, \quad \tilde{v}(\zeta,\tau)\big|_{\zeta=0} = 0, \quad \left.\frac{\partial \tilde{v}(\zeta,\tau)}{\partial \zeta}\right|_{\zeta=0} = 0, \quad \tilde{w}(\zeta,\tau)\big|_{\zeta=0} = 0, \quad \left.\frac{\partial \tilde{w}(\zeta,\tau)}{\partial \zeta}\right|_{\zeta=0} = 0 \tag{2.21}$$

At the other end with the tip mass $(\zeta = \tilde{L})$, the boundary conditions become

$$\tilde{M}\frac{\partial^2 \tilde{u}}{\partial \tau^2} - 2\tilde{M}\gamma \frac{\partial \tilde{v}}{\partial \tau} + \frac{\partial \tilde{u}}{\partial \zeta} - \tilde{M}\gamma^2 \tilde{u} = 0 \tag{2.22a}$$

$$\tilde{M}\frac{\partial^2 \tilde{v}}{\partial \tau^2} + 2\tilde{M}\gamma \frac{\partial \tilde{u}}{\partial \tau} - \frac{1}{\lambda^2}\frac{\partial^3 \tilde{v}}{\partial \zeta^3} - T(\tilde{L})\frac{\partial \tilde{v}}{\partial \zeta} - \frac{\gamma^2}{\lambda^2}\frac{\partial \tilde{v}}{\partial \zeta} + \frac{1}{\lambda^2}\frac{\partial^3 \tilde{v}}{\partial \zeta \partial \tau^2} - \tilde{M}\gamma^2 \tilde{v} = 0 \tag{2.22b}$$

$$-\frac{\partial^2 \tilde{v}}{\partial \zeta^2} + \tilde{J}\lambda^2 \frac{\partial^3 \tilde{v}}{\partial \zeta \partial \tau^2} = 0 \tag{2.22c}$$

$$\tilde{M}\frac{\partial^2 \tilde{w}}{\partial \tau^2} - \frac{1}{\lambda^2}\frac{\partial^3 \tilde{w}}{\partial \zeta^3} - T(\tilde{L})\frac{\partial \tilde{w}}{\partial \zeta} - \frac{\gamma^2}{\lambda^2}\frac{\partial \tilde{w}}{\partial \zeta} + \frac{1}{\lambda^2}\frac{\partial^3 \tilde{w}}{\partial \zeta \partial \tau^2} = 0 \tag{2.22d}$$

$$\frac{\partial^2 \tilde{w}}{\partial \zeta^2} + \tilde{J}\lambda^2 \frac{\partial^3 \tilde{w}}{\partial \zeta \partial \tau^2} = 0 \tag{2.22e}$$

Finally, when soil–structure interaction (SSI) is included, the fixed-end boundary conditions at $\zeta = 0$ are modified to incorporate the effect of discrete soil springs and their dimensionless forms are presented

below:

$$\frac{\partial \tilde{u}}{\partial \zeta} - \tilde{K}_V \tilde{u} = 0 \tag{2.23a}$$

$$-\frac{1}{\lambda^2}\frac{\partial^3 \tilde{v}}{\partial \zeta^3} - T(0)\frac{\partial \tilde{v}}{\partial \zeta} - \frac{\gamma^2}{\lambda^2}\frac{\partial \tilde{v}}{\partial \zeta} + \frac{1}{\lambda^2}\frac{\partial^3 \tilde{v}}{\partial \zeta \partial \tau^2} - \tilde{K}_L \tilde{v} - \tilde{K}_{LR}\frac{\partial \tilde{v}}{\partial \zeta} = 0 \tag{2.23b}$$

$$-\frac{\partial^2 \tilde{v}}{\partial \zeta^2} + \tilde{K}_R \frac{\partial \tilde{v}}{\partial \zeta} + \tilde{K}_{LR}\tilde{v} = 0 \tag{2.23c}$$

$$-\frac{1}{\lambda^2}\frac{\partial^3 \tilde{w}}{\partial \zeta^3} - T(0)\frac{\partial \tilde{w}}{\partial \zeta} - \frac{\gamma^2}{\lambda^2}\frac{\partial \tilde{w}}{\partial \zeta} + \frac{1}{\lambda^2}\frac{\partial^3 \tilde{w}}{\partial \zeta \partial \tau^2} - \tilde{K}_L \tilde{w} - \tilde{K}_{LR}\frac{\partial \tilde{w}}{\partial \zeta} = 0 \tag{2.23d}$$

$$-\frac{\partial^2 \tilde{w}}{\partial \zeta^2} + \tilde{K}_R \frac{\partial \tilde{w}}{\partial \zeta} + \tilde{K}_{LR}\tilde{w} = 0 \tag{2.23e}$$

# 3

# Stability Analysis

The stability of structures is of significant importance, especially in civil and offshore engineering. Instability can develop suddenly and grow rapidly, often leading to failure of the structure. Classical examples of instability include the buckling of building columns and railway track lines, galloping and flutter of power lines and bridges, and the instability of conveyor belts and pipes conveying fluid.

In the previous chapter, a mathematical model of a rotating cantilever beam inside a geotechnical centrifuge was developed using a non-inertial frame of reference, which introduced pseudo-forces, such as centrifugal and Coriolis forces in the system. The centrifugal forces introduced axial compression in the beam. Moreover, the EOMs of axial and lateral bending motions were coupled through the Coriolis force terms. These two forces might trigger instability, which needs to be determined through a stability analysis. Note that Euler forces were not considered following the assumption that the angular velocity of the centrifuge was assumed to be constant.

Using the mathematical model developed in the previous chapter, the stability of the small-scale model is analysed in this chapter, providing insights into the applicability and limitations of the current centrifuge experimental techniques on slender small-scale models. Both flapwise and chordwise motions are studied using the dimensionless EOMs. A dispersion analysis is first performed to understand the possibility of instability mechanisms, after which the role of boundary conditions is incorporated. Finally, a parametric study is conducted to assess the sensitivity of instability to key system parameters. Note that the effect of SSI is not considered in this chapter and is examined in Chapter 4 using a case study.

## 3.1. Concept of Stability

A characteristic feature of instability is that the deformation occurs in a direction different from that of the applied load. Consider a structure subjected to external forces that is in equilibrium. For whatever reason, if the structure is perturbed from this equilibrium position, these forces begin to act and either restore the system back to its original equilibrium or drive it further away. The equilibrium is said to be stable if, after this perturbation, the structure returns to its original equilibrium. But if the system moves away from equilibrium, the system is said to be unstable.

For instability to develop, the system must have an external source supplying energy into the system. In the case of galloping of power lines, the wind force acts as the source of energy, whereas in the case of classical buckling of building columns, the weight of the floor does the work needed to destabilise the column.

## 3.2. Types of Instabilities

Instability in structures can broadly be classified into two categories: static and dynamic. Static instability, also referred to as divergence, occurs at zero frequency and can therefore be examined using

static considerations. In such cases, upon perturbation, the structure suddenly shifts to a new equilibrium configuration once the critical load is exceeded without oscillating. Euler buckling of columns is a classical example of static instability.

Dynamic instability, also referred to as flutter, on the other hand, occurs at non-zero frequencies. In this case, the response amplitude grows gradually over successive oscillation cycles, thereby requiring a dynamic analysis. The term flutter is often used to describe this phenomenon in a mathematical sense, where the system oscillates while simultaneously becoming unstable. A well-known example is the galloping of iced power lines under wind. Another form of dynamic instability is physical flutter, which arises from the coupling of different displacement fields. Here, instability originates from the phase relationship between the coupled motions, where one displacement field feeds energy into and amplifies the response of the other. The failure of the Tacoma Narrows Bridge is a classical example of physical flutter-type instability

## 3.3. Mathematics of Stability Analysis

The governing EOMs of the three displacement fields, $u$, $v$, and $w$, derived in the Chapter 2 form a linear, homogeneous system of equations, mathematically describing a free vibration problem. Therefore, the stability of such a linear dynamical system can be fully determined by analysing its eigenvalues. Using the governing EOMs, an eigenvalue problem is generated by substituting a harmonic time-dependent function, $e^{\mathbf{i}\omega t}$, into the governing equations, where $\omega$ represents the eigenvalues of the system and $\mathbf{i} = \sqrt{-1}$ is the imaginary unit. For a conservative system, the eigenvalues are real. For non-conservative systems, for example, in systems with damping, the eigenvalues are complex, which can be represented as

$$\omega = \Re\{\omega\} + \mathbf{i}\,\Im\{\omega\}$$

where $\Re\{\omega\}$ is the real part and $\Im\{\omega\}$ is the imaginary part of $\omega$.

The time-dependent function can then be expressed as

$$e^{\mathbf{i}.\Re\{\omega\}.t}.e^{-\Im\{\omega\}.t}$$

The first part, $e^{\mathbf{i}.\Re\{\omega\}.t}$, represents stable harmonic oscillations with time, whereas the second part, $e^{-\Im\{\omega\}.t}$, represents either exponential growth or decay depending on the sign of $\Im\{\omega\}$.

If the eigenvalues have a negative imaginary part, the amplitude of the corresponding mode grows with time, and the system becomes unstable, which can happen when there is an energy source pumping energy into the system. Two primary cases can be distinguished when the imaginary part of the eigenvalue is negative: divergence, which occurs when the real part of the eigenvalue is zero, and flutter, which occurs when the real part is non-zero.

$$\begin{aligned} \text{Divergence}: \ & \Re\{\omega\} = 0 \quad \text{and} \quad \Im\{\omega\} < 0 \\ \text{Flutter}: \ & \Re\{\omega\} \neq 0 \quad \text{and} \quad \Im\{\omega\} < 0 \end{aligned}$$

With this framework in place, the concept of stability is now applied to the case of a rotating cantilever beam inside a geotechnical centrifuge.

## 3.4. Stability Analysis of Flapwise Motion

The governing EOMs that describe the flapwise motion of a rotating cantilever beam inside a centrifuge are derived in the previous chapter. The flapwise motion describes the vertical bending vibrations of the beam and is decoupled from the other displacement fields ($u$ and $v$). Therefore, its dynamics can be studied independently. The dimensionless form of the governing equations is repeated below for the reader's convenience.

Governing differential equation:

$$\frac{\partial^2 \tilde{w}}{\partial \tau^2} + \frac{1}{\lambda^2}\frac{\partial^4 \tilde{w}}{\partial \zeta^4} + \frac{\gamma^2}{\lambda^2}\frac{\partial^2 \tilde{w}}{\partial \zeta^2} + \frac{\partial}{\partial \zeta}\left[T(\zeta)\frac{\partial \tilde{w}}{\partial \zeta}\right] - \frac{1}{\lambda^2}\frac{\partial^4 \tilde{w}}{\partial \zeta^2 \partial \tau^2} = 0 \tag{3.1}$$

Boundary conditions, at $\zeta = 0$

$$\tilde{w}(\zeta,\tau)\big|_{\zeta=0} = 0 \quad \text{and} \quad \left.\frac{\partial\tilde{w}(\zeta,\tau)}{\partial\zeta}\right|_{\zeta=0} = 0$$

Boundary conditions, at $\zeta = \tilde{L}$

$$\tilde{M}\frac{\partial^2\tilde{w}}{\partial\tau^2} - \frac{1}{\lambda^2}\frac{\partial^3\tilde{w}}{\partial\zeta^3} - T(\tilde{L})\frac{\partial\tilde{w}}{\partial\zeta} - \frac{\gamma^2}{\lambda^2}\frac{\partial\tilde{w}}{\partial\zeta} + \frac{1}{\lambda^2}\frac{\partial^3\tilde{w}}{\partial\zeta\partial\tau^2} = 0$$

$$\frac{\partial^2\tilde{w}}{\partial\zeta^2} + \tilde{J}\lambda^2\frac{\partial^3\tilde{w}}{\partial\zeta\partial\tau^2} = 0$$

where

$$T(\zeta) = \tilde{M}\tilde{r}\gamma^2 + \gamma^2\left[(\tilde{r}+\tilde{L})(\tilde{L}-\tilde{\zeta}) - \left(\frac{\tilde{L}^2-\tilde{\zeta}^2}{2}\right)\right]$$

The governing differential equation is a balance of forces acting on a differential element of the beam along the $z$ direction. The first term corresponds to the product of mass and acceleration of the element. The second term represents the restoring force due to the flexural rigidity of the beam and therefore contributes a stabilising effect. The third term introduces a destabilising effect resulting from axial compression induced by centrifugal forces, while the fourth term accounts for an additional destabilising contribution arising from the spatial variation of the centrifugal force within the cross-section of the beam. Together, the third and fourth terms have softening effects on the system. The fifth term accounts for the rotational inertia of the element. It should be noted that structural damping is not included in this formulation.

The above EOMs constitute a linear system of equations, and as discussed earlier, for linear systems, stability is fully determined by analysing the eigenvalues.

### 3.4.1. Scope of Instability

From the governing EOM, Eq. (3.1), it is evident that no damping term is present, which rules out the possibility of galloping-type instability, which happens when the effective damping of the system turns negative. Physical flutter type of instability happens when the displacement fields are coupled. However, since flapwise motion is decoupled from other displacement fields, physical flutter cannot occur. Instability in this case arises from the reduction of effective stiffness due to the axial compression force, which may reduce the stiffness to zero and lead to divergence instability. Consequently, the stability of flapwise bending can be examined using static considerations, similar to classical Euler buckling.

The stability of flapwise bending is investigated through a stepwise approach, beginning with the simplest formulation. The analysis is then gradually extended by including complex terms, and finally, the exact stability behaviour is obtained using numerical techniques.

### 3.4.2. Dispersion Analysis

Dispersion analysis is used as a first step to determine whether instability is possible in a system. Physically, it represents the case of a very long beam, where boundary conditions can be neglected. The dispersion equation is obtained by substituting a propagating wave $w(x,t) = W_0 e^{i(\omega t - kx)}$ into the EOM, and it represents a relation between the wavenumbers and angular frequencies of the waves that can exist as per the chosen model. Here, $T(\zeta) = \tilde{M}\tilde{r}\gamma^2$ is considered to be constant to obtain analytical solutions. This means the centrifugal force acting on the distributed mass of the beam is neglected as compared to the tip mass. $\omega$ is the frequency, $k$ is the wavenumber, and $W_0$ represents the maximum amplitude of the wave. Substituting the propagating waveform into the EOM gives the dispersion equation.

$$k^4 + \left(-\tilde{M}\gamma^2\lambda^2\tilde{r} - \gamma^2 - \omega^2\right)k^2 - \omega^2\lambda^2 = 0 \tag{3.2}$$

Eq. (3.2) can be solved analytically for $\omega$, giving the frequency as a function of the wavenumber. The resulting relations are known as dispersion curves and are plotted in Fig. 3.1 for $\tilde{r} = 3.40625$ and

$\lambda = 41.2$ and for different values of $\tilde{M}$ and $\gamma$. Since the dispersion equation is quadratic in $\omega$, two roots are obtained, meaning that each wavenumber corresponds to two frequencies.

The dispersion curves show that, for certain ranges of wavenumbers, the frequencies become complex when $\gamma > 0$. Physically, this can be interpreted by imagining an initial perturbation to the system, such as a small deflection or an impact. This initial disturbance can be represented as a sum of harmonic space-dependent functions using Fourier transform, and the system responds at the frequencies allowed by the model. A complex-valued frequency with a negative imaginary part implies that the response grows exponentially with time, meaning the system becomes unstable. As $\gamma$ increases, the low-wavenumber modes become unstable. Moreover, an increase in the dimensionless tip mass value enlarges the instability region because the axial compression force becomes larger.

When $\gamma = 0$, the system reduces to an infinitely long, non-rotating Rayleigh beam. This is a conservative system as there is no energy input, and hence all the frequencies are real, and no instability occurs.

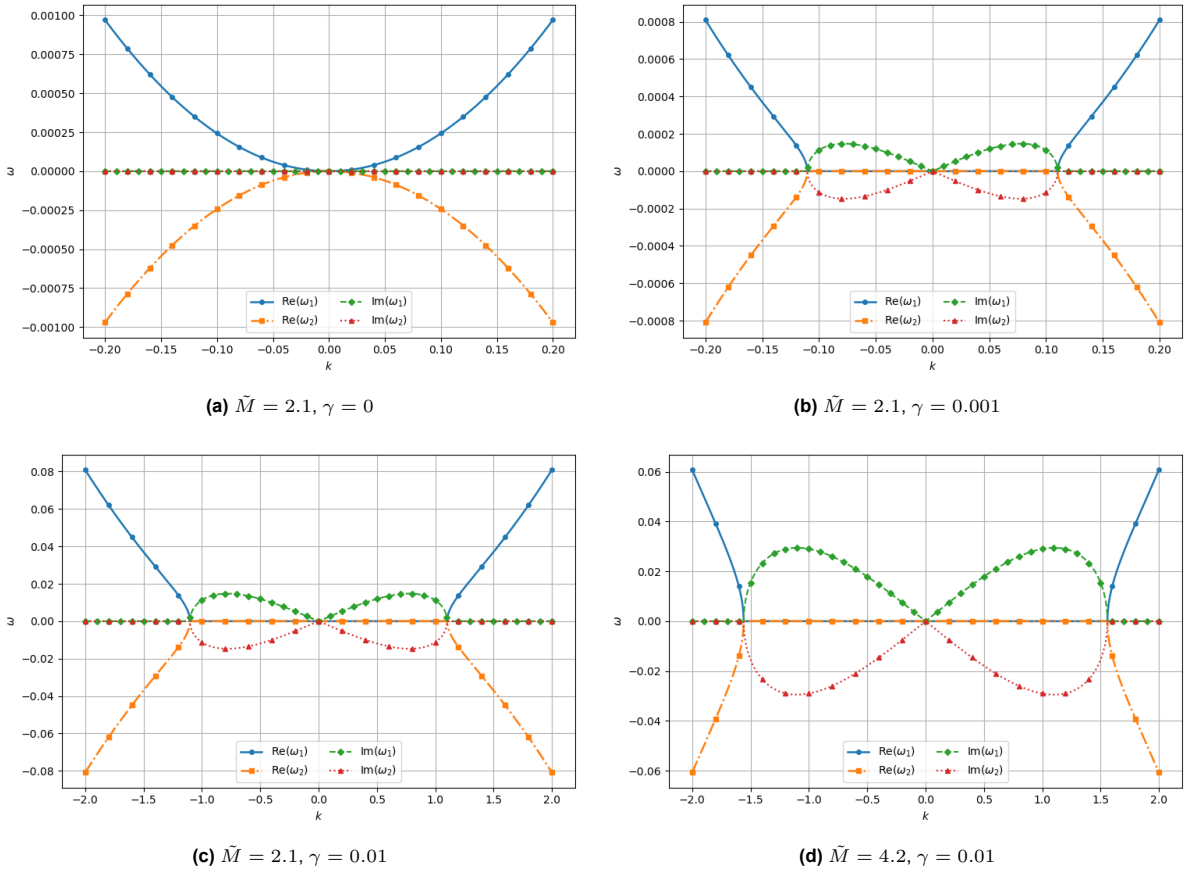


**(a)** $\tilde{M} = 2.1, \gamma = 0$ **(b)** $\tilde{M} = 2.1, \gamma = 0.001$

**(c)** $\tilde{M} = 2.1, \gamma = 0.01$ **(d)** $\tilde{M} = 4.2, \gamma = 0.01$

**Figure 3.1:** Dispersion analysis of flapwise motion for $\tilde{r} = 3.40625$ and $\lambda = 41.2$.

### 3.4.3. Effect of Boundary Conditions

Dispersion analysis indicates that the system has the potential to become unstable. However, whether instability actually occurs depends on the specific boundary conditions of the system.

To determine the critical angular velocity, $\gamma_{\text{cr}}$, corresponding to the onset of divergence instability of flapwise motion for the actual boundary conditions, a static solution, $\tilde{w}(x,t) = \tilde{W}(x)$ is substituted into the governing equations. This is because the divergence type of instability can be analysed using static considerations, as it happens at zero frequency. This results in the following equations that describe the dimensionless form of flapwise motion for the static case. Note that the partial derivative is replaced by an ordinary derivative, as the system now depends on only the spatial variable, $x$.

Governing differential equation (Statics):

$$\frac{1}{\lambda^2}\frac{d^4\tilde{W}}{d\zeta^4} + \frac{\gamma^2}{\lambda^2}\frac{d^2\tilde{W}}{d\zeta^2} + \frac{d}{d\zeta}\left[T(\zeta)\frac{d\tilde{W}}{d\zeta}\right] = 0 \tag{3.3}$$

Boundary conditions, at $\zeta = 0$:

$$\tilde{W}(\zeta)\big|_{\zeta=0} = 0 \quad \text{and} \quad \left.\frac{d\tilde{W}(\zeta)}{d\zeta}\right|_{\zeta=0} = 0$$

Boundary conditions, at $\zeta = \tilde{L}$:

$$-\frac{1}{\lambda^2}\frac{\partial^3\tilde{w}}{\partial\zeta^3} - T(\tilde{L})\frac{\partial\tilde{w}}{\partial\zeta} - \frac{\gamma^2}{\lambda^2}\frac{\partial\tilde{w}}{\partial\zeta} = 0 \quad \text{and} \quad \frac{\partial^2\tilde{w}}{\partial\zeta^2} = 0$$

where

$$T(\zeta) = \tilde{M}\tilde{r}\gamma^2 + \gamma^2\left[(\tilde{r}+\tilde{L})(\tilde{L}-\tilde{\zeta}) - \left(\frac{\tilde{L}^2-\tilde{\zeta}^2}{2}\right)\right]$$

Due to the spatial dependence of $T(\zeta)$, the EOM has non-constant coefficients, and therefore, a general closed-form analytical solution is not available, which means that the system of equations needs to be solved numerically.

#### Simplest case

A simplified form of flapwise motion is considered to estimate the $\gamma_{\text{cr}}$ for the onset of divergence instability analytically. In general, obtaining a closed-form solution depends strongly on the boundary conditions, and in many cases, it is not possible. For the present case, with one end fixed (ignoring SSI) and the other end free, an analytical expression for the stability limit can be derived if the centrifugal force on the distributed mass of the beam is neglected. In this case, the axial compression becomes constant along the length, given by $T(\zeta) = \tilde{M}\tilde{r}\gamma^2$.

Under this assumption, the governing equations simplify to a system with constant coefficients. An exponential form of general solution is assumed for the differential equation, which is substituted into the boundary conditions to generate a coefficient matrix. By setting the determinant of the coefficient matrix to zero, the first dimensionless buckling angular velocity is obtained as

$$\gamma_{cr} = \frac{\pi}{2\sqrt{\tilde{M}\tilde{r}\lambda^2 + 1}} \tag{3.4}$$

This expression provides a preliminary but non-conservative estimate of the critical dimensionless angular velocity for divergence in flapwise bending. The actual $\gamma_{cr}$ must be smaller than the value predicted by this expression.

Numerical analysis is carried out to determine the critical angular velocity when $T(\zeta)$ varies along the beam length.

### 3.4.4. Parametric Stability Analysis

A sensitivity analysis is performed to investigate the influence of different parameters on the stability behaviour of flapwise motion.

#### Influence of $\tilde{M}$ and $\lambda$

The effect of dimensionless tip mass, $\tilde{M}$, and slenderness ratio, $\lambda$, on the critical angular velocity, $\gamma_{cr}$, is examined, neglecting SSI. As the centrifuge rotates, centrifugal forces act on both the concentrated tip mass and the distributed mass of the beam. These forces generate an effective axial compression along the beam length, which softens the system.

The relation between $\gamma_{cr}$ and $\lambda$ for different values of $\tilde{M}$ is presented in Fig. 3.2. The plots show that the stability behaviour of the system follows the trends consistent with the behaviour of classical Euler

buckling of a column. As the slenderness ratio increases, the beam becomes more prone to buckling. Similarly, increasing the tip mass increases the axial compression force, causing the beam to buckle at lower angular velocities.

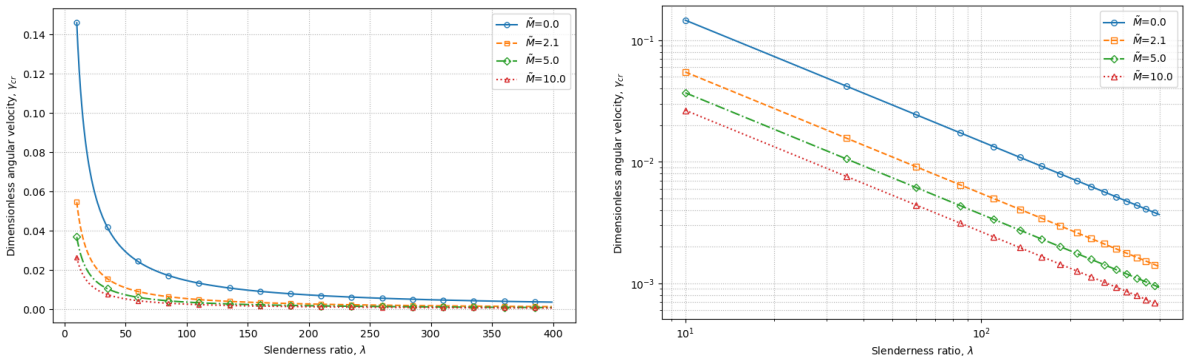


**(a)** Normal scale **(b)** log-log scale

**Figure 3.2:** Flapwise motion - Influence of $\tilde{M}$ and $\lambda$ on $\gamma_{\text{cr}}$ for $\tilde{r} = 3.40625$ (Without SSI).

This behaviour can be understood as a balance between bending stiffness, which stabilises the system, and centrifugal axial compression, which softens, thereby causing divergence instability. Mathematically, when the effective stiffness of the system turns negative, the system loses its stability through divergence. Short beams are governed by stiffness and require high angular velocities to lose stability, while longer beams become more flexible and buckle at much lower velocities.

### Sensitivity to spatial dependence of $T(\zeta)$

The effect of the centrifugal force on the system is examined. As described earlier, the axial compression force in the beam is induced due to the centrifugal force acting on the tip mass and on the distributed mass of the beam. Substituting typical values shows that their magnitudes can be of similar order. However, the tip mass produces a stronger destabilising effect because it acts at the free end $\zeta = \tilde{L}$, while the resultant of the distributed load acts closer to the root, $\zeta = 0$, resulting in a smaller effective length. As a result, the contribution of the tip mass is expected to dominate, which is confirmed in the plot below.

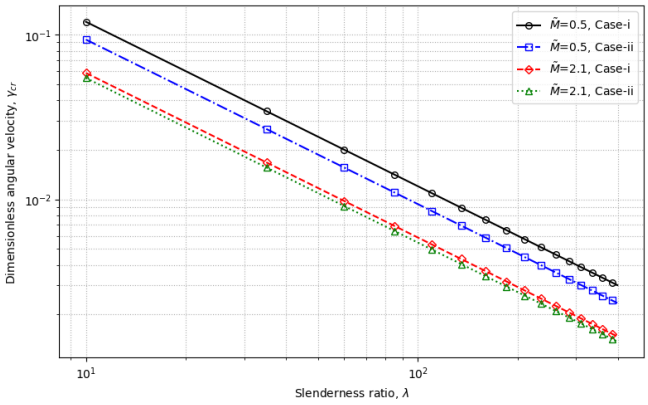


**Figure 3.3:** Flapwise motion - Influence of spatial dependence of $T(\zeta)$ on $\gamma_{\text{cr}}$ for $\tilde{r} = 3.40625$ (Without SSI)

In Fig. 3.3, Case–i corresponds to assuming $T(\zeta)$ as constant, $\tilde{M}\tilde{r}\gamma^2$, while Case–ii considers $T(\zeta)$ as varying along the beam length. The results show that the centrifugal force acting on the distributed mass of the beam can be neglected in comparison to the tip mass when making a preliminary estimate of the critical angular velocity for design purposes, especially when the tip mass is heavy. At small values of $\tilde{M}$, the distributed mass of the beam still has some influence, but as $\tilde{M}$ increases, the tip mass effect becomes predominant.

### Influence of $\tilde{r}$

The centrifugal force is directly proportional to the radius of the centrifuge, $\tilde{r}$. Increasing the radius, therefore, increases the axial compression along the beam, which reduces the critical angular velocity by further softening the system. Fig. 3.4 shows the influence of $\tilde{r}$ on the onset of divergence instability of flapwise motion.

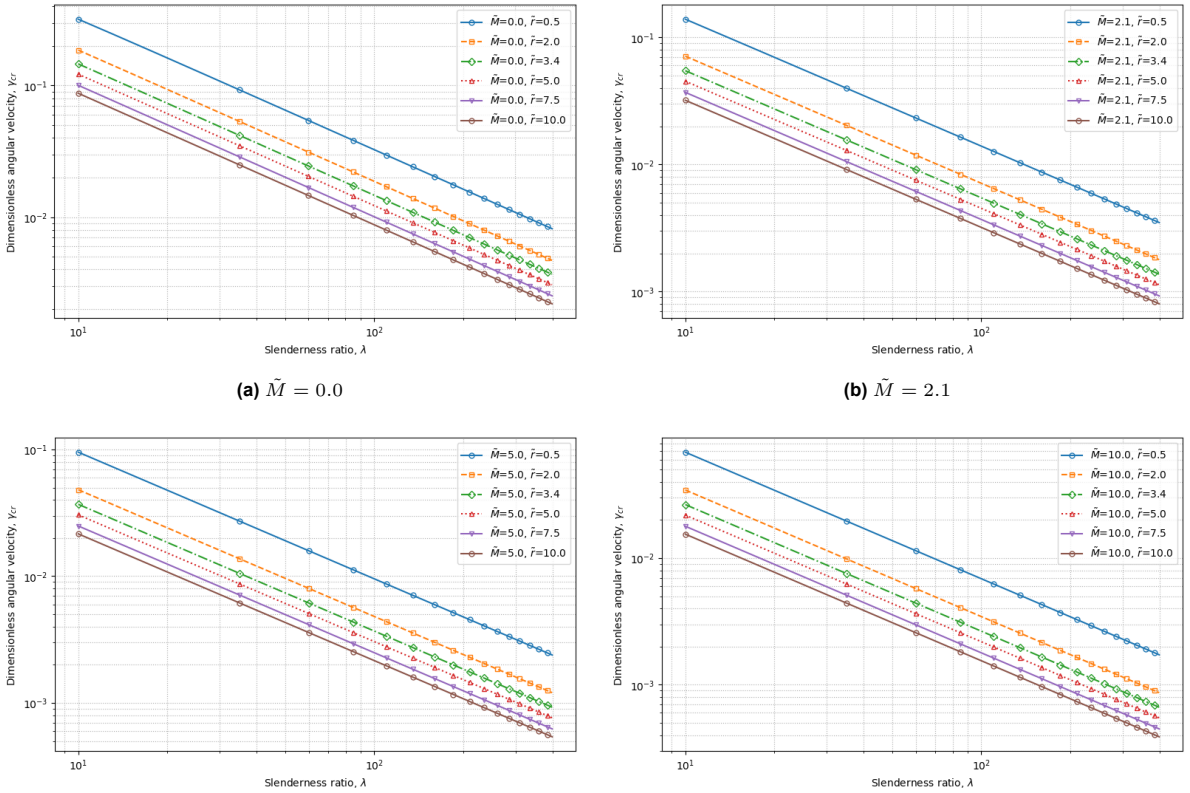


**(a)** $\tilde{M} = 0.0$ **(b)** $\tilde{M} = 2.1$

**(c)** $\tilde{M} = 5.0$ **(d)** $\tilde{M} = 10.0$

**Figure 3.4:** Flapwise motion - Influence of $\tilde{r}$ on $\gamma_{cr}$ for various $\tilde{M}$ values (Without SSI).

## 3.5. Stability Analysis of Chordwise Motion

Chordwise motion of the rotating beam is characterized by the interaction of lateral bending motion along $y$ direction and axial displacement along the $x$ direction, coupled through the velocity-dependent Coriolis terms. The governing EOMs that describe the chordwise motion as derived in the previous chapter are presented again in their dimensionless forms for the reader's convenience.

Governing differential equations:

$$\frac{\partial^2 \tilde{u}}{\partial \tau^2} - 2\gamma \frac{\partial \tilde{v}}{\partial \tau} - \frac{\partial^2 \tilde{u}}{\partial \zeta^2} - \gamma^2 \tilde{u} = 0 \tag{3.5a}$$

$$\frac{\partial^2 \tilde{v}}{\partial \tau^2} + 2\gamma \frac{\partial \tilde{u}}{\partial \tau} + \frac{1}{\lambda^2}\frac{\partial^4 \tilde{v}}{\partial \zeta^4} + \frac{\gamma^2}{\lambda^2}\frac{\partial^2 \tilde{v}}{\partial \zeta^2} + \frac{\partial}{\partial \zeta}\left[T(\zeta)\frac{\partial \tilde{v}}{\partial \zeta}\right] - \frac{1}{\lambda^2}\frac{\partial^4 \tilde{v}}{\partial \zeta^2 \partial \tau^2} - \gamma^2 \tilde{v} = 0 \tag{3.5b}$$

Boundary conditions, at $\zeta = 0$

$$\tilde{u}(\zeta,\tau)\big|_{\zeta=0} = 0, \quad \tilde{v}(\zeta,\tau)\big|_{\zeta=0} = 0, \quad \text{and} \quad \left.\frac{\partial \tilde{v}(\zeta,\tau)}{\partial \zeta}\right|_{\zeta=0} = 0$$

Boundary conditions, at $\zeta = \tilde{L}$

$$\tilde{M}\frac{\partial^2\tilde{u}}{\partial\tau^2} - 2\tilde{M}\gamma\frac{\partial\tilde{v}}{\partial\tau} + \frac{\partial\tilde{u}}{\partial\zeta} - \tilde{M}\gamma^2\tilde{u} = 0$$

$$\tilde{M}\frac{\partial^2\tilde{v}}{\partial\tau^2} + 2\tilde{M}\gamma\frac{\partial\tilde{u}}{\partial\tau} - \frac{1}{\lambda^2}\frac{\partial^3\tilde{v}}{\partial\zeta^3} - T(\tilde{L})\frac{\partial\tilde{v}}{\partial\zeta} - \frac{\gamma^2}{\lambda^2}\frac{\partial\tilde{v}}{\partial\zeta} + \frac{1}{\lambda^2}\frac{\partial^3\tilde{v}}{\partial\zeta\partial\tau^2} - \tilde{M}\gamma^2\tilde{v} = 0$$

$$-\frac{\partial^2\tilde{v}}{\partial\zeta^2} + \tilde{J}\lambda^2\frac{\partial^3\tilde{v}}{\partial\zeta\partial\tau^2} = 0$$

where

$$T(\zeta) = \tilde{M}\tilde{r}\gamma^2 + \tilde{\gamma}\left[(\tilde{r}+\tilde{L})(\tilde{L}-\tilde{\zeta}) - \left(\frac{\tilde{L}^2-\tilde{\zeta}^2}{2}\right)\right]$$

Compared to the EOM of flapwise motion, (3.3), two additional terms appear in the governing differential equation of lateral bending of the chordwise motion, (3.5b). The first is the velocity-dependent Coriolis term $(2\gamma\frac{\partial\tilde{v}}{\partial t})$, which couples the axial and lateral bending motions. The second is $-\gamma^2\tilde{v}$, which represents the component of the centrifugal force perpendicular to the deformed beam. This term is mathematically a negative stiffness term, and hence has a destabilising effect on the system.

Eq. (3.5a) describes the balance of forces acting on a differential element of the beam along the $x$ direction. The first term represents the product of mass and acceleration of the element along the x direction. The second is the Coriolis term $(-2\gamma\frac{\partial\tilde{u}}{\partial t})$, which couples $u$ and $v$, and the third is the restoring force from axial stiffness of the beam. The fourth term, $-\gamma^2\tilde{u}$, is the centrifugal force in addition to the static component along the $x$ direction due to axial oscillations, and it has a destabilising effect.

Because of the Coriolis coupling, the two fields, $u$ and $v$, are linked and must be solved together along with their boundary conditions. In total, the chordwise motion consists of two coupled equations of motion and six boundary conditions. Unlike flapwise motion, a preliminary analytical estimate of the critical velocity is not possible here due to the coupling. Therefore, the stability of chordwise motion must be assessed through a dynamic analysis of the coupled system using numerical techniques.

### 3.5.1. Scope of Instability

In chordwise motion, the displacement fields, $u$ and $v$, are coupled by the velocity-dependent Coriolis terms. This coupling may cause flutter-type instability, which requires a dynamic analysis. In addition, similar to flapwise motion, the axial compression force may reduce the effective stiffness to zero, leading to divergence instability. Furthermore, a combined interaction between flutter and divergence can also occur.

### 3.5.2. Dispersion Analysis

As described earlier, dispersion analysis can reveal the possibility of instability in a system. The propagating wave forms are assumed for both the coupled displacement fields, expressed as $u(x,t) = U_0 e^{i(\omega t - kx)}$ and $v(x,t) = V_0 e^{i(\omega t - kx)}$, and substituted into the governing EOMs. The axial compression force in the beam is considered to be constant, $T(\zeta) = \tilde{M}\tilde{r}\gamma^2$, to obtain analytical results. The dispersion equation is obtained by setting the determinant of the coefficient matrix to zero. Figs. 3.5 and 3.6 show the dispersion curves obtained by solving the dispersion equation, plotted for $\tilde{r} = 3.40625$ and $\lambda = 41.2$ and for different values of $\tilde{M}$ and $\gamma$

$$\det\begin{bmatrix} k^2-\omega^2-\gamma^2 & -2i\,\omega\gamma \\ 2i\,\omega\gamma & \dfrac{\left[\left(-\tilde{M}k^2\tilde{r}-1\right)\gamma^2-\omega^2\right]\lambda^2 + k^2\left(k^2-\omega^2-\gamma^2\right)}{\lambda^2} \end{bmatrix} = 0$$

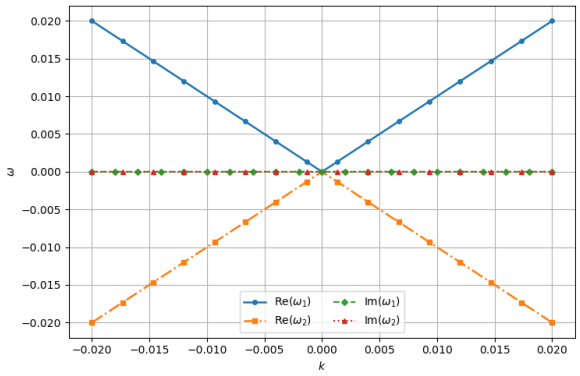


**(a)** First and second roots of the dispersion equation

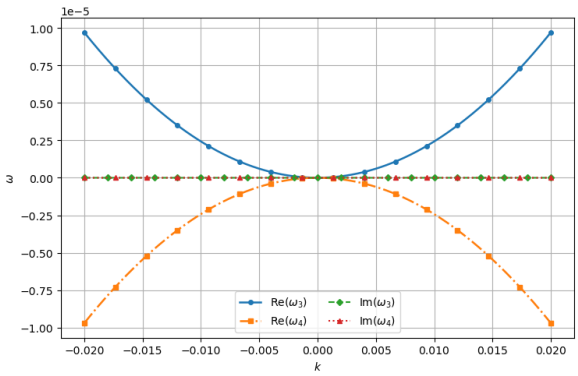


**(b)** Third and fourth roots of the dispersion equation

**Figure 3.5:** Dispersion analysis of chordwise motion for $\tilde{r} = 3.40625$, $\lambda = 41.2$, $\tilde{M} = 2.1$, and $\gamma = 0$.

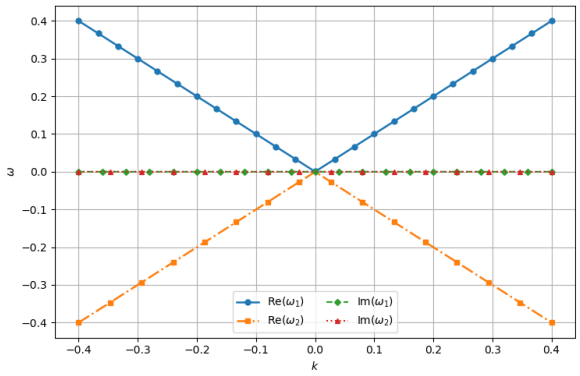


**(a)** First and second roots of the dispersion equation

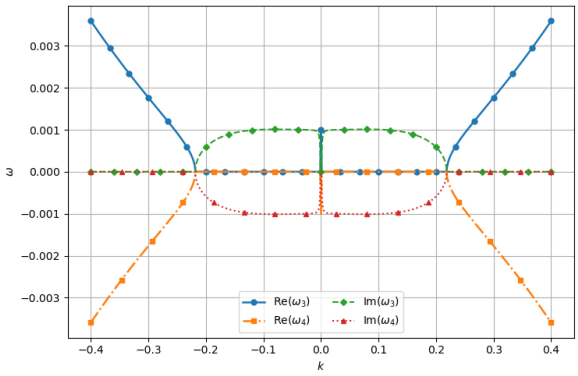


**(b)** Third and fourth roots of the dispersion equation

**Figure 3.6:** Dispersion analysis of chordwise motion for $\tilde{r} = 3.40625$, $\lambda = 41.2$, $\tilde{M} = 2.1$ and $\gamma = 0.001$.

The dispersion relation for chordwise motion yields four roots, giving two pairs of frequencies for each wavenumber. When $\gamma = 0$, the system is conservative and hence all the frequencies remain real, consistent with a stable, non-rotating system. For non-zero $\gamma$, however, some branches acquire a negative imaginary part, which signals the possibility of instability. It is interesting to notice that the real part of $\omega$ is zero when the imaginary part turns non-zero, indicating a divergence type of instability. However, whether instability actually occurs and the possibility of flutter-type instability depend on the specific boundary conditions of the system.

### 3.5.3. Eigenfrequencies of Chordwise Motion

The effect of boundary conditions is considered in this subsection, and a numerical analysis is performed to evaluate the eigenfrequencies of the system. Fig. 3.7 shows the evolution of the first four eigenfrequencies as a function of dimensionless angular velocity, $\gamma$. Note that coupling of the DOFs is considered in the numerical analysis, including the spatial variation of axial compression force, while SSI is neglected.

The eigenfrequency curves in Fig. 3.7 are plotted for $\tilde{M} = 2.1$, $\lambda = 41.225$, and $\tilde{r} = 3.40625$. They show a progressive decrease of the real part of each eigenfrequency with increasing $\gamma$. At critical angular velocities, the real part becomes zero and the corresponding imaginary part becomes non-zero, marking the onset of divergence-type instability. The first bending mode is the first to destabilise. Interestingly, the third bending mode becomes unstable earlier than the first axial mode, even though the axial motion has a lower eigenfrequency compared to the third bending mode. This indicates that the onset of instability in chordwise motion is governed primarily by bending behaviour, while the axial mode contributes only at much higher angular velocities. Therefore, it can be concluded that flutter-

type instability does not occur for the parameters chosen in this subsection within the considered range of $\gamma$.

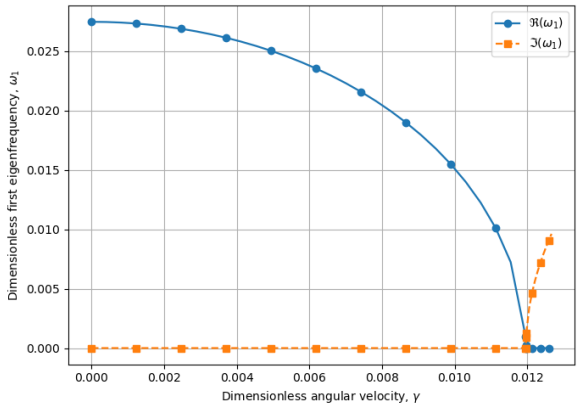


**(a)** First eigenfrequency (Lateral bending)

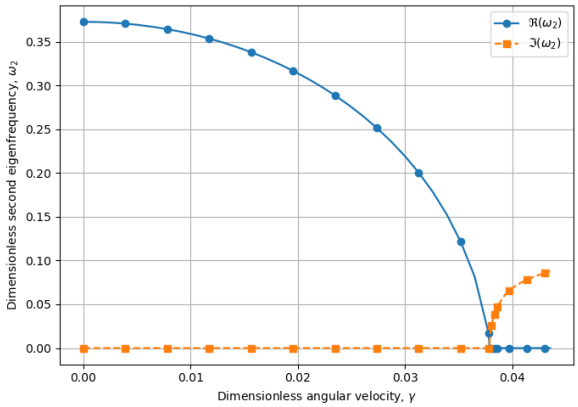


**(b)** Second eigenfrequency (Lateral bending)

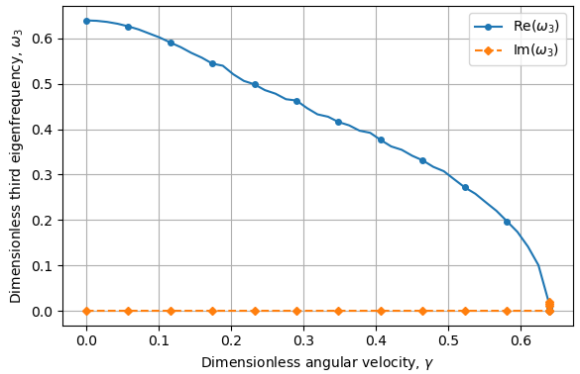


**(c)** Third eigenfrequency (Axial motion)

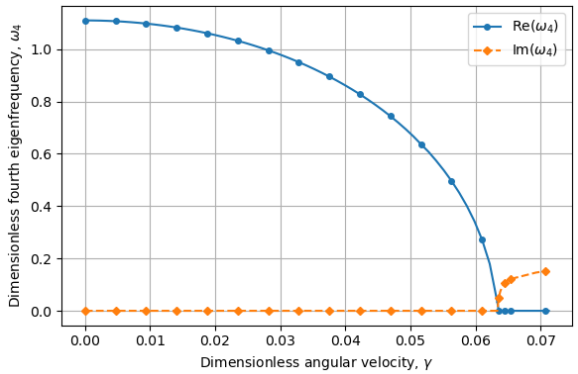


**(d)** Fourth eigenfrequency (Lateral bending)

**Figure 3.7:** Chordwise motion - eigenfrequencies for $\tilde{M} = 2.1$, $\lambda = 41.225$, $\tilde{r} = 3.40625$.

### 3.5.4. Effect of Coriolis Terms

Instability in chordwise motion can originate from two main factors: the coupling of displacement fields through the Coriolis terms, and the reduction in stiffness caused by axial compression induced by the centrifugal force. In the previous subsection, it was revealed that the chordwise motion experiences a divergence-type of instability for the chosen set of parameters. In this subsection, the Coriolis terms are neglected from both the governing differential equations and the boundary conditions, and the eigenfrequencies are plotted in Fig. 3.8 to understand the influence of the Coriolis term.

The resulting frequency curves closely resemble those obtained with the Coriolis term included. A noticeable difference is observed in the eigenvalues of the axial mode, which occurs at very high angular velocities of the centrifuge, beyond the practical range of operation. This shows that the dominant factor driving instability is the softening effect produced by axial compression, while the Coriolis coupling plays only a secondary role. In other words, the presence or absence of the Coriolis term has little impact on the onset of instability, confirming that axial compression governs the primary mechanism of divergence in chordwise motion for the set of parameters considered ($\tilde{M} = 2.1$, $\lambda = 41.225$, and $\tilde{r} = 3.40625$). The evolution of eigenshapes with and without the effect of the Coriolis term is shown in Appendix F.

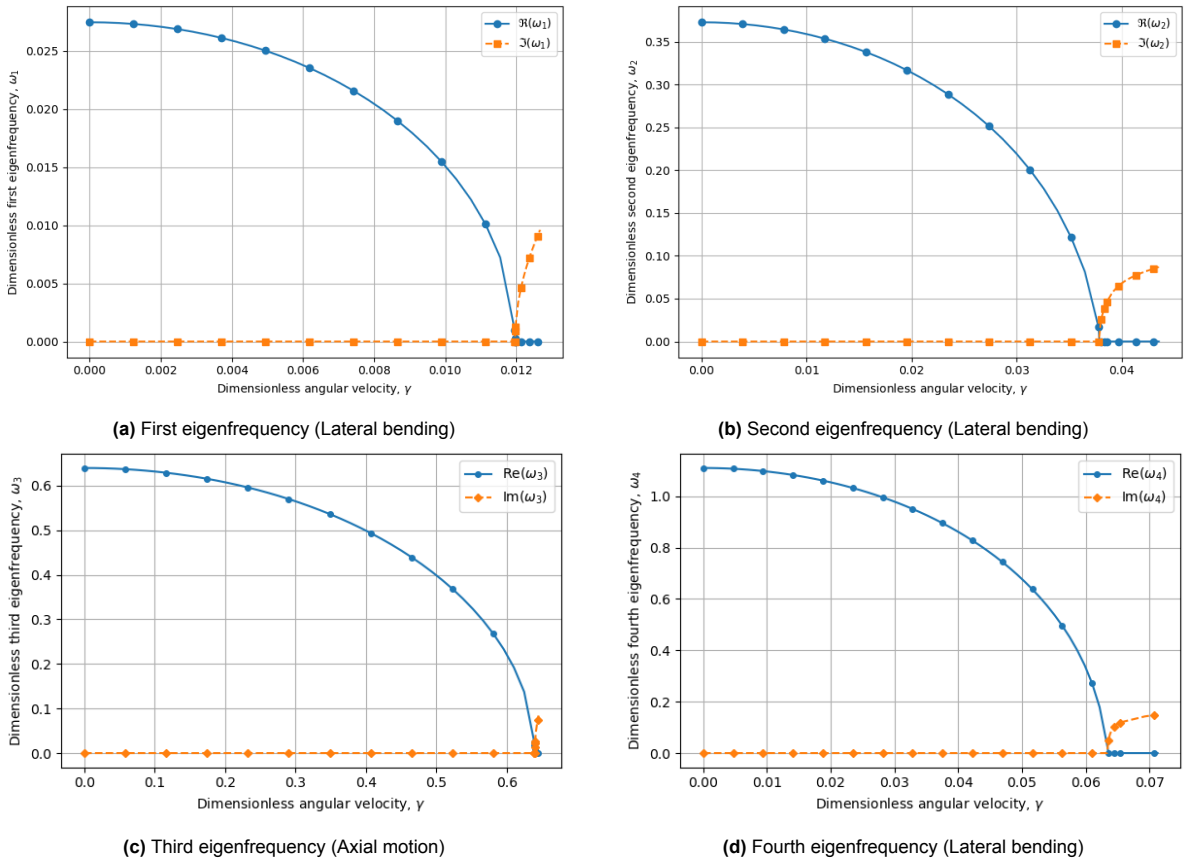


**(a)** First eigenfrequency (Lateral bending)

**(b)** Second eigenfrequency (Lateral bending)

**(c)** Third eigenfrequency (Axial motion)

**(d)** Fourth eigenfrequency (Lateral bending)

**Figure 3.8:** Chordwise motion - eigenfrequencies (Without Coriolis term) $\tilde{M} = 2.1$, $\lambda = 41.225$, $\tilde{r} = 3.40625$.

### 3.5.5. Parametric Stability Analysis

Using numerical techniques, a sensitivity study is performed in this subsection to investigate the influence of different parameters on the onset of divergence instability of chordwise motion.

#### Influence of $\tilde{M}$ and $\lambda$

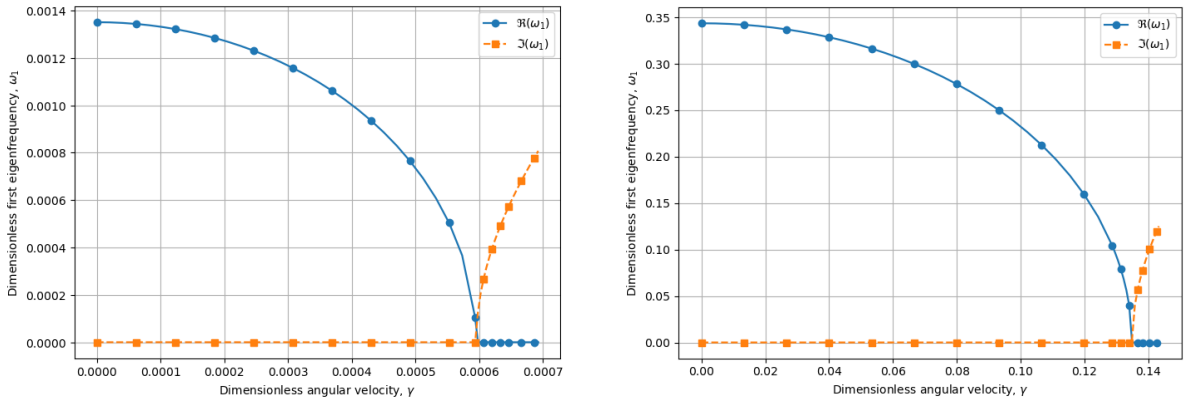


**(a)** Flexible case - $\tilde{M} = 10$ and $\lambda = 400$

**(b)** Stiff case - $\tilde{M} = 0$ and $\lambda = 10$

**Figure 3.9:** Chordwise motion - First eigenfrequency for extreme case of $\tilde{M}$ and $\lambda$ for $\tilde{r} = 3.40625$ (Without SSI).

In the previous subsection, a dynamic analysis was performed for a specific set of parameters ($\tilde{M} = 2.1$, $\lambda = 41.225$, and $\tilde{r} = 3.40625$), and it was determined that the divergence-type of instability governs.

To generalize this statement, two more extreme cases are considered, and the evolution of the first eigenfrequency as a function of dimensionless angular velocity is plotted for both cases to verify if divergence remains the governing form of instability. The results are shown in Fig. 3.9, and divergence is again found to be the governing instability.

The effect of dimensionless tip mass, $\tilde{M}$, and slenderness ratio, $\lambda$ ,on the divergence instability of chordwise motion is plotted in Fig. 3.10, neglecting SSI. The softening effect of the centrifugal forces is similar to flapwise motion. The $\gamma_{\text{cr}}$ values of chordwise motion are slightly lower as compared to that of flapwise motion. This is because the EOM governing the lateral bending of chordwise motion, given by (3.5b), contains an additional negative stiffness term, $-\gamma^2 v$, which further reduces the effective bending stiffness. As a result, the system becomes softer and the critical angular velocity is reached at lower values compared to the flapwise motion. Hence, the system is expected to destabilise in chordwise motion before the flapwise motion begins to buckle.

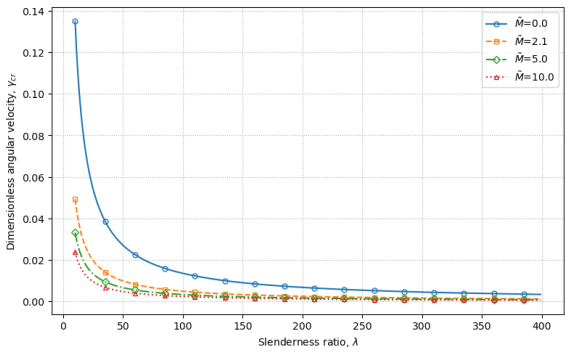


**(a)** Normal scale

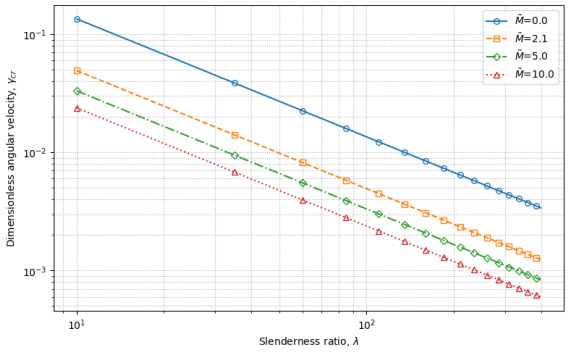


**(b)** Log-log scale

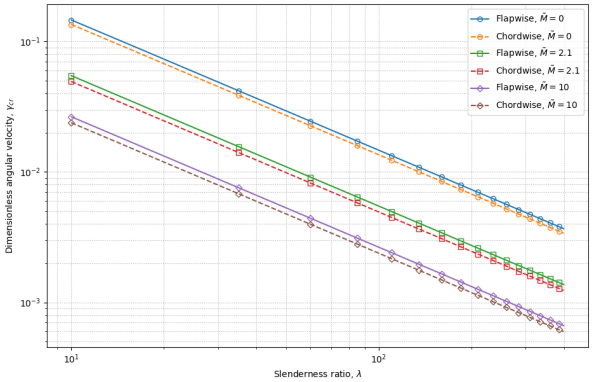


**(c)** Comparison between flapwise and chordwise bending (Log–log scale)

**Figure 3.10:** Chordwise motion - Influence of $\tilde{M}$ and $\lambda$ on $\gamma_{\text{cr}}$ for $\tilde{r} = 3.40625$ (Without SSI).

### Influence of $\tilde{r}$

In this subsection, two extreme values of the dimensionless radius, $\tilde{r}$ and dimensionless tip mass, $\tilde{M}$, are used to determine whether divergence instability governs and to check for the possibility of flutter. The first eigenfrequency is plotted as a function of $\gamma$ in the Fig. 3.11. The plot shows that the real part of the frequency keeps decreasing and becomes zero at a certain angular velocity. After this point, the frequency turns purely imaginary, which means the system no longer vibrates but instead grows without bound, similar to divergence instability.

Fig. 3.12 shows the influence of radius of centrifuge, $\tilde{r}$, on the onset of divergence instability of chordwise motion. As expected, a higher radius of the centrifuge can decrease the critical angular velocity significantly.

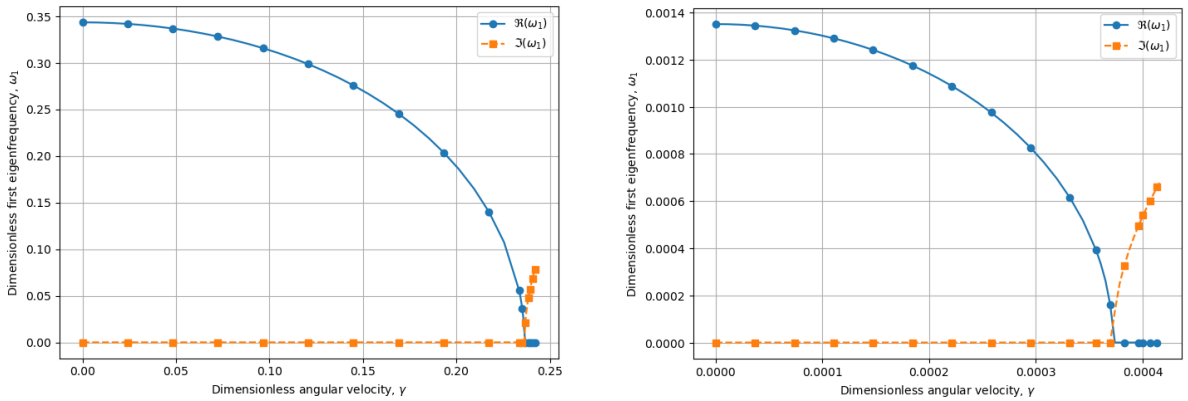


**(a)** $\tilde{M} = 0, \tilde{r} = 0.5, \lambda = 10$ **(b)** $\tilde{M} = 10, \tilde{r} = 10, \lambda = 400$

**Figure 3.11:** Chordwise motion - First eigenfrequency for extreme case of $\tilde{r}$

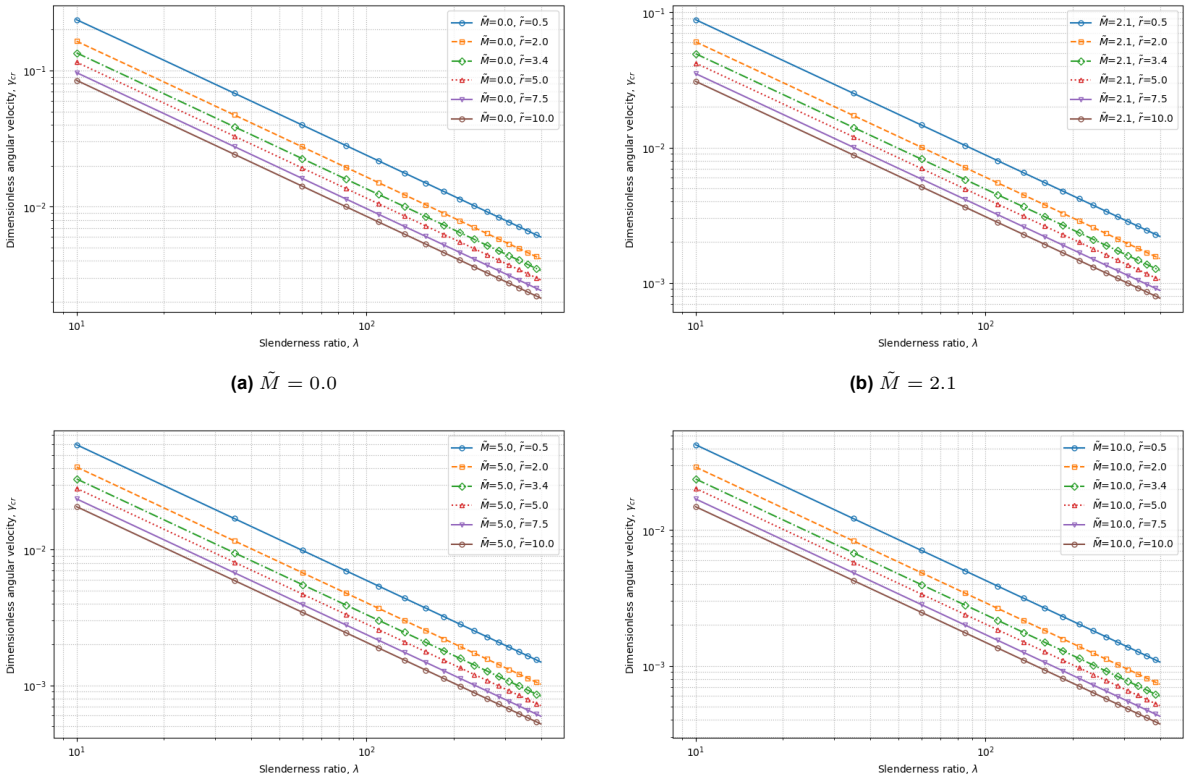


**(a)** $\tilde{M} = 0.0$ **(b)** $\tilde{M} = 2.1$

**(c)** $\tilde{M} = 5.0$ **(d)** $\tilde{M} = 10.0$

**Figure 3.12:** Chordwise motion - Influence of $\tilde{r}$ on $\gamma_{cr}$ for different $\tilde{M}$(Without SSI).

## 3.6. Conclusions

In this chapter, the stability of both flapwise and chordwise motions of a rotating cantilever beam inside a geotechnical centrifuge is studied using the dimensionless form of governing equations derived in Chapter 2. In addition, a parametric stability analysis is conducted to understand the influence of various parameters on the onset of instability. The analysis showed that:

- Flapwise motion is governed by divergence instability, since it is decoupled from other displacement fields ($u$ and $v$) and has no damping terms. As a result, static analysis is sufficient to predict

the critical dimensionless angular velocity. The main softening effect comes from the axial compression produced by centrifugal forces acting on the tip mass.

- Chordwise motion is more complex because the axial and lateral displacements are coupled through the Coriolis term. Although this coupling suggests the possibility of flutter, the results indicate that divergence remains the dominant form of first critical instability within the range of parameters considered. The Coriolis effect plays only a minor role compared to the softening caused by axial compression within the range of angular velocities considered. As a result, the instability of chordwise motion can be reliably estimated using static considerations.
- In both directions, the critical angular velocity decreases with larger tip mass, higher slenderness ratio, and greater centrifuge radius. These parameters increase the effective axial compression and make the system more prone to instability.
- Chordwise bending is more critical than flapwise bending because its governing equations include an additional negative stiffness term due to the centrifugal force. This extra softening means chordwise instability occurs at lower angular velocities compared to flapwise instability.

# 4

# Case study

In this chapter, the mathematical model developed earlier is applied to analyze the stability of the small-scale model of a monopile-founded OWT tested in the geotechnical centrifuge at ETH Zürich, as a part of the research project, DONISIS [3]. The objective is to examine whether the small-scale model experiences instabilities, such as divergence or flutter, within the operating angular velocity range of the centrifuge. The small-scale model, as shown in Fig. 1.1a, is considered first, and the effect of soil-structure interaction (SSI) is included through a lumped spring model as shown in Fig. 1.1b. The stability of flapwise motion is considered using static considerations, whereas dynamic stability analysis is performed for the chordwise motion. In addition, the present chapter aims to evaluate the influence of key parameters such as the length of the beam, the tip mass, the moment of inertia of the cross-section, and the effect of SSI on the onset of instability of the ETH Zürich case, henceforth referred to as "ETHZ".

## 4.1. Model Description

The small-scale model is designed to represent the behaviour of a full-scale prototype of a monopile-founded OWT. Its dimensions and proportions are derived using established simplified scaling laws. A detailed discussion of these scaling procedures is outside the scope of this thesis. Table 4.1 summarizes the geometric and material properties of the adopted small-scale model. These properties serve as the input for the stability analysis presented in the following sections.

**Table 4.1:** Geometric and material parameters of the small-scale OWT model and the centrifuge at ETHZ.

| Symbol | Description | Value | Unit |
|---|---|---|---|
| $\rho$ | Density of model material | $2\,700$ | $\mathrm{kg/m^3}$ |
| $E$ | Young's modulus | $6.89 \times 10^{10}$ | $\mathrm{N/m^2}$ |
| $A$ | Cross-sectional area | $3.704 \times 10^{-4}$ | $\mathrm{m^2}$ |
| $I_y$ | Second moment of area (about $z$-axis) | $2.17926 \times 10^{-7}$ | $\mathrm{m^4}$ |
| $I_z$ | Second moment of area (about $y$-axis) | $2.17926 \times 10^{-7}$ | $\mathrm{m^4}$ |
| $L$ | Beam length | $1.0$ | $\mathrm{m}$ |
| $r$ | Centrifuge arm radius | $3.40625$ | $\mathrm{m}$ |
| $M$ | Tip mass | $2.1$ | $\mathrm{kg}$ |
| $J$ | Rotational inertia of tip mass | $1.453119 \times 10^{-3}$ | $\mathrm{kgm^2}$ |
| $\Omega_{\text{ETHZ}}$ | Operating angular velocity of centrifuge | $16.74$ | $\mathrm{rad\,s^{-1}}$ |

The density $\rho$ and Young's modulus $E$ correspond to the aluminium alloy used for the small-scale beam model. To account for non-uniformities in the geometry of the beam, weighted average values of $A$, $I_y$, and $I_z$ are adopted. The parameter $r$ corresponds to the radius of the centrifuge at ETH Zürich.

## 4.2. Stability Analysis of Flapwise Motion - ETHZ

As discussed in section 3.4.1, flapwise motion can experience divergence type of instability, and the critical angular velocity, $\Omega_{\text{crit}}$, corresponding to the onset of instability can be estimated using static considerations.

### 4.2.1. Analytical and Numerical Estimates

A preliminary estimate of the critical angular velocity can be obtained using Eq. (3.4). By substituting the values of the ETHZ case and converting the result using the relation shown in Eq. (2.17), the critical angular velocity is calculated as $\Omega_{\text{crit}} = 71.95\,\text{rad}\,\text{s}^{-1}$. Note that while deriving this expression, the centrifugal force acting on the distributed mass of the beam and the influence of SSI are neglected, which have a softening effect. Consequently, the actual onset of instability is expected to happen at a lower angular velocity of the centrifuge.

A numerical static buckling analysis is performed considering the distribution of the axial compression force, and the critical angular velocity is computed as $\Omega_{\text{crit}} = 67.05\,\text{rad}\,\text{s}^{-1}$ (without SSI), which is close to the preliminary estimate. As soon as the angular velocity of the centrifuge reaches $\Omega_{\text{crit}}$, the flapwise motion of the small-scale model experiences a divergence type of instability, similar to classical Euler buckling. The effect of SSI on the $\Omega_{\text{crit}}$ is addressed in the next subsection.

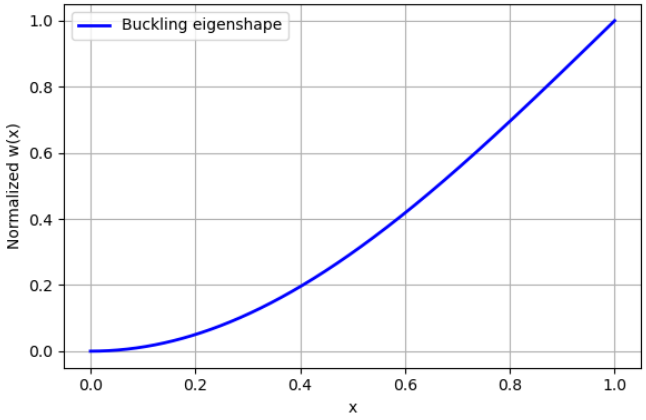


**Figure 4.1:** Eigenshape of first buckling mode of flapwise motion.

### 4.2.2. Parametric Stability Analysis of ETHZ case

To further investigate the sensitivity of the stability of the flapwise motion of the ETHZ case, a parametric stability analysis is performed. This analysis explores how variations in the key parameters affect the onset of instability. Note that the material properties of the beam, such as density and Young's modulus, and the radius of the centrifuge are considered to be constant.

#### Influence of $M$ and $L$

In this subsection, the effect of tip mass, $M$, and beam length, $L$, on the divergence instability of flapwise motion is examined, neglecting SSI. As the centrifuge rotates, centrifugal forces act on both the concentrated tip mass and the distributed self-weight of the beam. These forces generate an effective axial compression along the beam length, which has a softening effect and therefore destabilises the system.

A numerical analysis is performed and the results are presented in the Fig. 4.2, which shows the variation of $\Omega_{\text{crit}}$ as a function of beam length and tip mass.

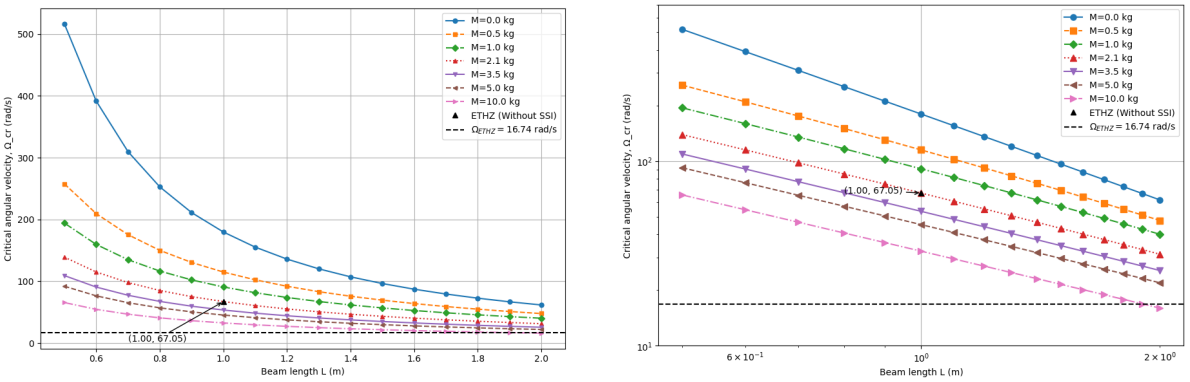


**(a)** Linear scale

**(b)** Log–log scale

**Figure 4.2:** Flapwise motion – Effect of $M$ and $L$ on $\Omega_{\text{crit}}$.

From the Fig. 4.2, it is observed that increasing the beam length, $L$, consistently lowers the $\Omega_{\text{crit}}$, making the system more prone to instability. The influence of tip mass, $M$, is strongest at shorter beam lengths, where even small increases significantly reduce stability (e.g., at $L = 0.5$ m, a $10\,\text{kg}$ tip mass decreases $\Omega_{\text{crit}}$ by more than $400\,\text{rad}\,\text{s}^{-1}$ compared to the massless case).

Comparison with the centrifuge operating velocity ($\Omega_{\text{ETHZ}} = 16.74$ rad/s) shows that the ETHZ case ($M = 2.1$ kg, $L = 1.0$ m, $\Omega_{cr} = 67.05$ rad/s) remains stable in flapwise motion, when SSI is neglected.

### Influence of Moment of Inertia of the cross-section

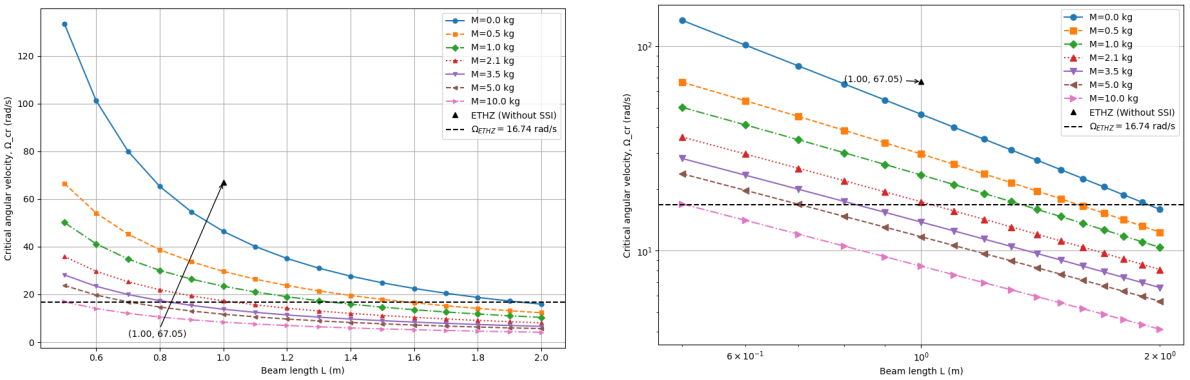


**(a)** EI/15 (Linear scale)

**(b)** EI/15 (Log–log scale)

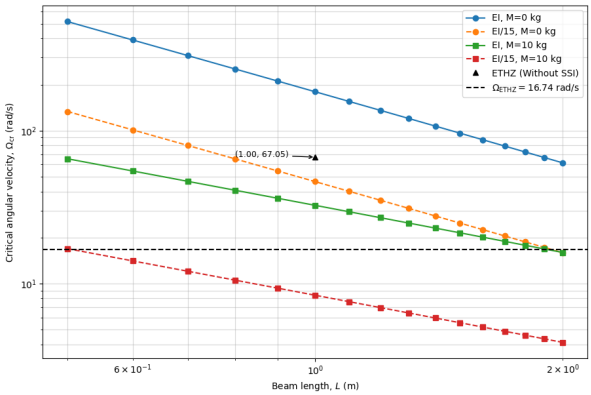


**(c)** Comparison between $EI$ and $EI/15$ (Log–log scale)

**Figure 4.3:** Flapwise motion – Effect of moment of inertia of the cross-section on $\Omega_{\text{crit}}$.

The bending stiffness of the beam, represented by the flexural rigidity $EI$, resists the divergence instability. It is interesting to determine the moment of inertia of the cross-section that leads to the instability of the ETHZ case. By trial and error, it is found that when the moment of inertia was reduced by a factor of $15$, while keeping all other parameters constant, the ETHZ case ($L = 1.0$ m, $M = 2.1$ kg) buckles at a critical angular velocity of approximately $17\,\mathrm{rad\,s^{-1}}$, which is very close to the operating velocity of the centrifuge. Fig. 4.3 shows the plots generated for the reduced stiffness case. Note that SSI is neglected.

Fig. 4.3 clearly shows the stabilising role of $EI$. While the destabilising axial force from centrifugal loading remains unchanged, the reduced stiffness lowers the beam's restoring capacity, making it more flexible and prone to buckling.

### Influence of SSI

In this subsection, the influence of SSI on the stability of the flapwise motion is examined. As described in section 2.6, SSI is incorporated through a lumped spring model at the mudline level. For this analysis, the Young's modulus of the soil is taken as $28\,\mathrm{MPa}$ at a depth of $0.09\mathrm{m}$ below the ground level. Table 4.2 summarizes the spring stiffness values corresponding to three representative soil profiles, namely, constant, linear, and parabolic distributions calculated as per the formulae shown in Appendix B.

**Table 4.2:** Spring stiffness values for different soil profiles ($E = 28\,\mathrm{MPa}$ at $0.09\,\mathrm{m}$ below the ground level).

| | Constant | Linear | Parabolic |
|---|---|---|---|
| $K_L\,(\mathrm{N\,m^{-1}})$ | $1.299 \times 10^7$ | $2.325 \times 10^7$ | $1.795 \times 10^7$ |
| $K_R\,(\mathrm{N\,m\,rad^{-1}})$ | $1.070 \times 10^6$ | $1.581 \times 10^6$ | $1.251 \times 10^6$ |
| $K_{LR}\,(\mathrm{N\,m\,m^{-1}})$ | $-2.475 \times 10^6$ | $-4.176 \times 10^6$ | $-3.413 \times 10^6$ |
| $K_V\,(\mathrm{N\,m^{-1}})$ | $1.034 \times 10^7$ | $8.545 \times 10^6$ | $9.563 \times 10^6$ |

The inclusion of SSI modifies the boundary conditions at the fixed end ($x = 0$), reducing the effective restraint provided by the soil as compared to the fixed base case. Note that the fixed base case is an extreme and a special case of SSI when the soil is assumed to be rigid. To quantify the effect of SSI, a numerical analysis is performed to determine the $\Omega_{\text{crit}}$ value for the ETHZ case ($L = 1.0\,\mathrm{m}$, $M = 2.1\,\mathrm{kg}$) and the results are summarized in Table 4.3.

**Table 4.3:** Flapwise motion - $\Omega_{\text{crit}}$ for ETHZ case for different soil profiles ($E = 28\,\mathrm{MPa}$ at $0.09\,\mathrm{m}$ below the ground level).

| | Constant | Linear | Parabolic | Without SSI |
|---|---|---|---|---|
| $\Omega_{\text{crit}}\ \mathrm{rad\,s^{-1}}$ | $65.293$ | $65.776$ | $65.303$ | $67.050$ |

As per Table 4.3, the inclusion of SSI slightly reduces the $\Omega_{\text{crit}}$ compared to the fixed-end case. Among the three soil profiles, the values remain close, with the linear distribution giving the largest $\Omega_{\text{crit}}$ and the constant profile the lowest. Overall, the reduction is modest (about $2 - 3\%$), indicating that for the given soil stiffness, the effect of SSI on flapwise divergence instability is present but not dominant.

To further investigate the combined effect of SSI, beam length, $L$, and tip mass, $M$, numerical analyses were carried out for several extreme cases of $M$ and $L$. The corresponding critical angular velocities are presented in Table 4.4. The variations lie in the range of $1.25$ to $7\%$.

**Table 4.4:** $\Omega_{\text{crit}}$ (Rad/sec) for different soil profiles, tip masses and beam lengths ($E = 28\,\text{MPa}$ at $0.09\,\text{m}$ below the ground level).

| $M$ kg | $L$ m | Constant | Linear | Parabolic | Without SSI |
|---|---|---|---|---|---|
| 0.0 | 0.5 | 479.76 | 489.54 | 479.96 | 516.55 |
| 0.0 | 1.0 | 172.98 | 174.81 | 173.02 | 179.67 |
| 0.0 | 2.0 | 60.37 | 60.69 | 60.37 | 61.55 |
| 2.1 | 0.5 | 132.06 | 133.91 | 132.10 | 138.92 |
| 2.1 | 1.0 | 65.29 | 65.78 | 65.30 | 67.05 |
| 2.1 | 2.0 | 30.82 | 30.94 | 30.82 | 31.26 |
| 10.0 | 0.5 | 62.31 | 63.16 | 62.33 | 65.46 |
| 10.0 | 1.0 | 31.66 | 31.88 | 31.67 | 32.47 |
| 10.0 | 2.0 | 15.76 | 15.81 | 15.76 | 15.96 |

The influence of SSI on the flapwise stability is illustrated in Fig. 4.4 for the parabolic soil profile, which is the representative of the soil conditions encountered at the prototype. The plots present the variation of the $\Omega_{\text{crit}}$ with respect to beam length, $L$, and tip mass, $M$. Fig. 4.4 and Table 4.4 show that tip mass and beam length have a strong effect on stability. Larger tip masses and longer beams greatly reduce the $\Omega_{\text{crit}}$, making the system more prone to instability. In comparison, the influence of SSI is small, causing only a few percent reduction in $\Omega_{\text{crit}}$ relative to the fixed-base case.

The trends remain the same as in the fixed-end condition: increasing tip mass and beam length lower $\Omega_{\text{crit}}$, while SSI only shifts the curves slightly downward due to reduced foundation stiffness. For typical soil stiffness, SSI does not change the overall instability behaviour, and it is reasonable to ignore SSI.

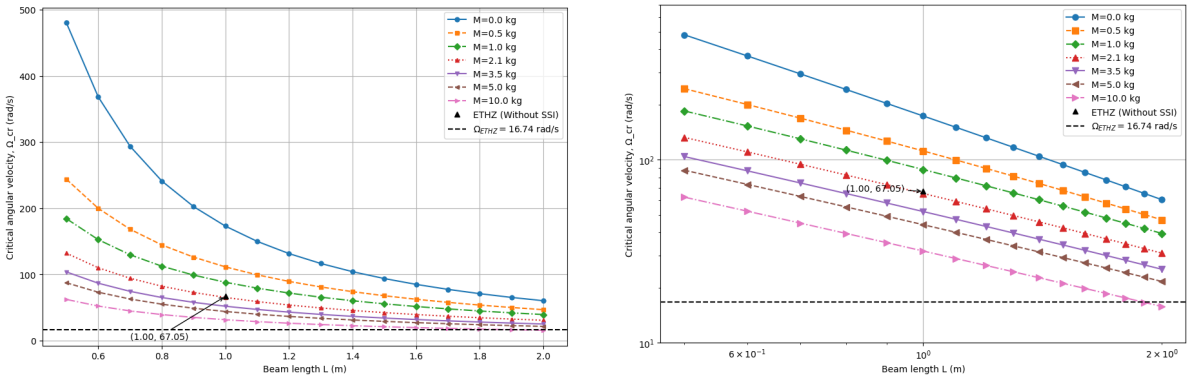


**(a)** Linear scale

**(b)** Log–log scale

**Figure 4.4:** Flapwise motion – Effect of SSI on $\Omega_{\text{crit}}$.

In summary, tip mass and beam length are the main factors controlling divergence instability, while SSI plays only a minor role. However, in very soft soils, SSI can reduce the critical velocity enough to fall within the centrifuge's operating range, which may trigger instability during testing.

In the Fig. 4.5, a parametric analysis is conducted by varying the stiffness of the soil, and the results are plotted. From the figure, it can be observed that a soil with a Young's modulus of $50\,\text{MPa}$ exhibits behaviour very close to that of a rigid foundation, which indicates that further increases in stiffness would not significantly affect the critical angular velocity.

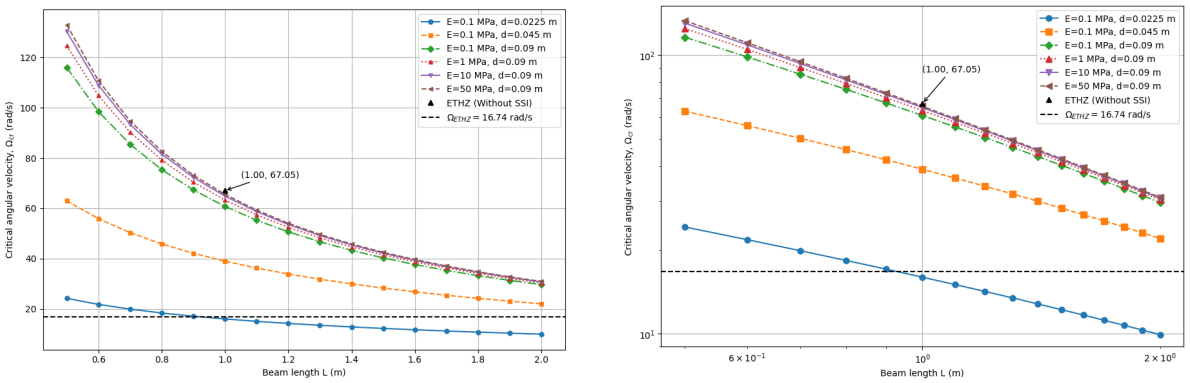


**(a)** Linear scale

**(b)** Log–log scale

**Figure 4.5:** Flapwise motion – Parametric analysis on the effect of various soil stiffness values (at a depth of $1\,\mathrm{m}$ below the ground level) on $\Omega_{\text{crit}}$ for ETHZ case.

It is interesting to determine the soil stiffness that can lead to divergence instability in the ETHZ case during the operating angular velocity of the centrifuge, which is $16.74\,\mathrm{rad\,s^{-1}}$. By trial and error, it is determined that the critical angular velocity is approximately $17\,\mathrm{rad\,s^{-1}}$ for a value of $E = 0.1\,\mathrm{MPa}$ with a diameter of the small-scale model of $22.5$ mm. The corresponding spring stiffness values are listed in Table 4.5. A stiffness of $0.1\,\mathrm{MPa}$ is very low for soils and may occur during extreme cases, which is when the entire soil layer is liquified, which may happen during earthquakes.

**Table 4.5:** Spring stiffness values for the extreme soil case $E = 0.1\,\mathrm{MPa}$ and $d = 25\,\mathrm{mm}$.

| | Constant | Linear | Parabolic |
|---|---|---|---|
| $K_L\,(\mathrm{N\,m^{-1}})$ | $3.786 \times 10^4$ | $1.492 \times 10^5$ | $7.762 \times 10^4$ |
| $K_R\,(\mathrm{N\,m\,rad^{-1}})$ | $4.086 \times 10^3$ | $8.002 \times 10^3$ | $5.346 \times 10^3$ |
| $K_{LR}\,(\mathrm{N\,m\,m^{-1}})$ | $-9.245 \times 10^3$ | $-2.740 \times 10^4$ | $-1.509 \times 10^4$ |
| $K_V\,(\mathrm{N\,m^{-1}})$ | $2.349 \times 10^4$ | $1.652 \times 10^4$ | $1.981 \times 10^4$ |

## 4.3. Stability Analysis of Chordwise Motion

As described in Section 3.5.1, stability of chordwise motion requires a dynamic analysis due to velocity-dependent Coriolis coupling between $u$ and $v$ DOFs. In contrast to flapwise bending, where a simplified analytical expression allows for a preliminary estimate of the $\Omega_{\text{crit}}$, such an approximation is not possible here due to the coupling term. Consequently, the stability of chordwise motion must be assessed directly through numerical analysis of the coupled system.

### 4.3.1. Eigenfrequencies of ETHZ Case

A numerical analysis is performed to evaluate the first four eigenfrequencies of the chordwise motion for the ETHZ case. The results, shown in Figs. 4.6, illustrate the development of both real and imaginary parts of the first four eigenfrequencies of the chordwise motion as the angular velocity of the centrifuge increases. Note that when the eigenfrequency turns complex, with a negative imaginary part, the system becomes unstable. When the eigenfrequency slowly approaches zero as the angular velocity increases, the system experiences a divergence type of instability. The first three bending frequencies, as well as the first axial frequency of the coupled chordwise motion, are presented. Soil–structure interaction is not considered in this analysis in order to isolate the structural behaviour.

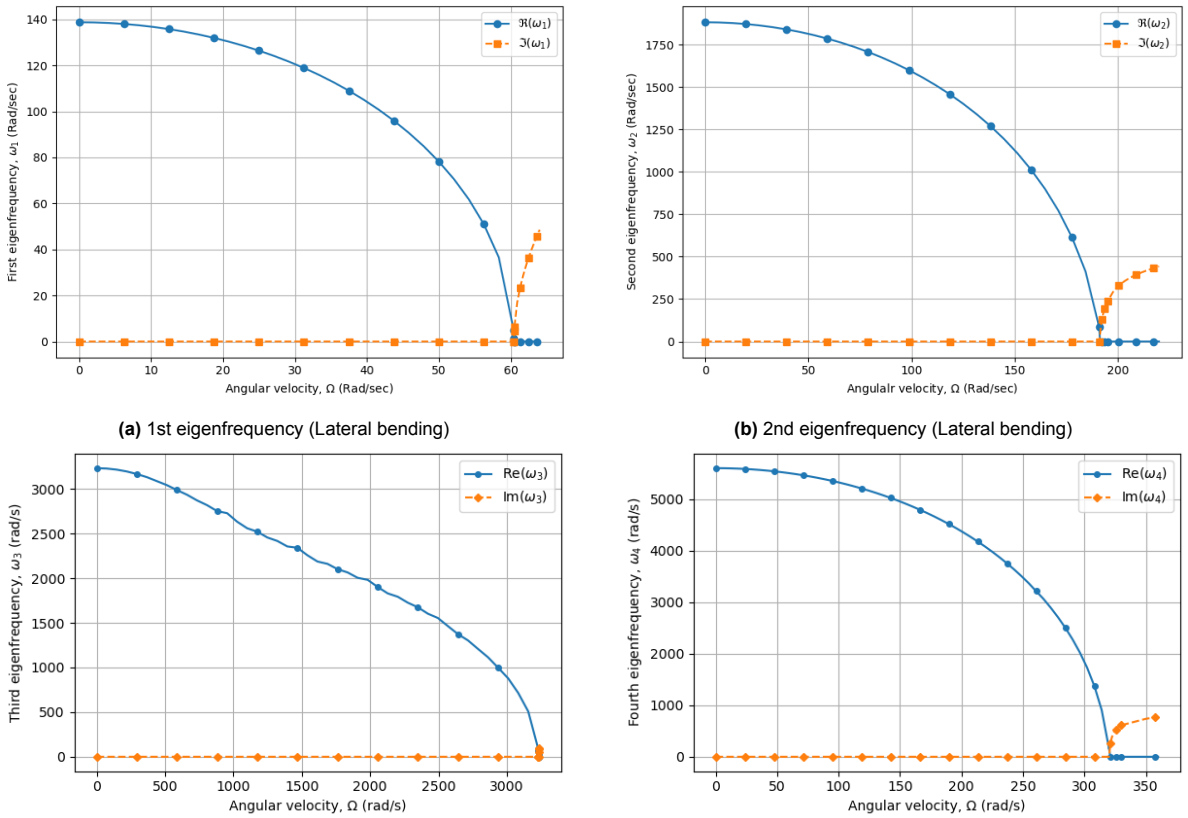


**(a)** 1st eigenfrequency (Lateral bending)

**(b)** 2nd eigenfrequency (Lateral bending)

**(c)** 3rd eigenfrequency (Axial motion)

**(d)** 4th eigenfrequency (Lateral bending)

**Figure 4.6:** Chordwise motion - Influence of $\Omega$ on the eigenfrequencies.

In all cases, the real part of the frequency decreases steadily as the angular velocity increases, reflecting the progressive softening of the system due to axial compression. At the critical angular velocity, the real part becomes zero, marking the onset of instability. Beyond this point, the imaginary part becomes non-zero, which indicates that the mode transitions into an unstable state with exponential growth. These results confirm that divergence-type instability governs the chordwise motion, with each mode exhibiting the same characteristic behaviour at its respective critical velocity.

For the ETHZ case, the first bending mode becomes unstable at around $\Omega \approx 60\,\mathrm{rad\,s^{-1}}$, the second bending mode at about $\Omega \approx 190\,\mathrm{rad\,s^{-1}}$, and the first axial mode at approximately $\Omega \approx 3232\,\mathrm{rad\,s^{-1}}$. The fourth mode also follows the same trend, with instability occurring near $\Omega \approx 320\,\mathrm{rad\,s^{-1}}$.

The dominant mechanism driving the reduction in natural frequencies is the axial compression induced by centrifugal forces, which leads to a softening effect and ultimately governs the onset of instability. This behaviour is consistent with the flapwise case, though chordwise modes become critical at lower velocities due to the additional softening term. Fig. **??** shows the evolution of eigenshapes with angular velocity

### 4.3.2. Parametric Stability Analysis of ETHZ case

In this section, a parametric stability analysis is conducted to investigate the influence of various parameters on the divergence instability of chordwise motion. The parameters are varied within a reasonable range, and the corresponding critical angular velocities are evaluated through numerical analysis. The results are presented in the following plots, which illustrate how each parameter affects the onset of divergence instability. Note that the material properties are not changed.

#### Influence of $M$ and $L$

The following plots show the variation of the critical angular velocity of divergence instability for chordwise motion, $\Omega_{crit}$, as the tip mass and length of the beam are varied.

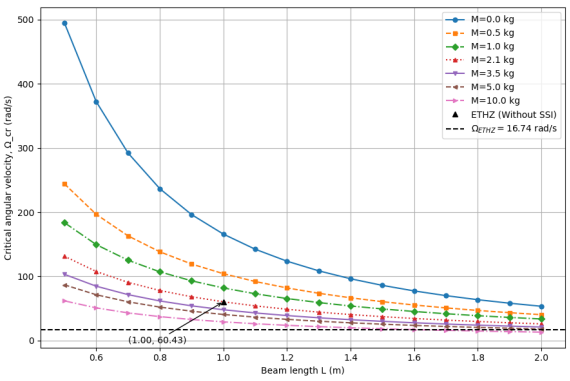


**(a)** Linear scale

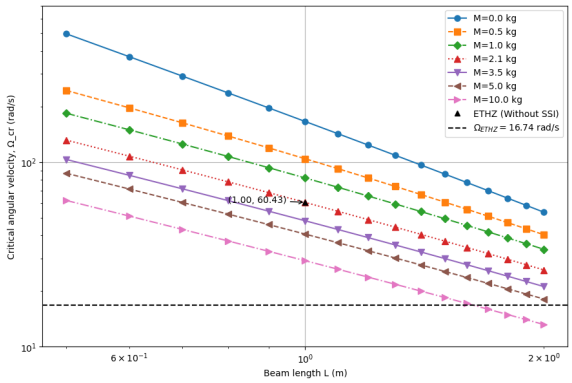


**(b)** Log–log scale

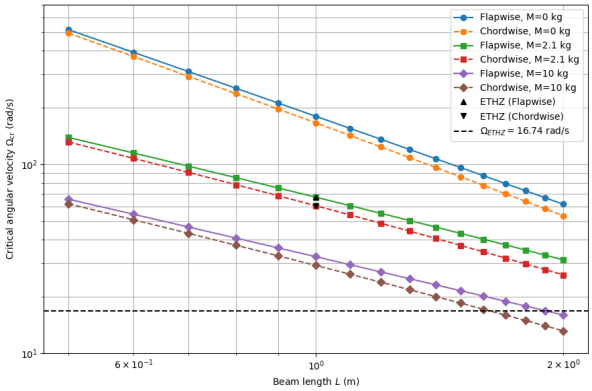


**(c)** Comparison between chordwise and flapwise bending (Log–log scale)

**Figure 4.7:** Chordwise motion – Influence of $M$ and $L$ on $\Omega_{\text{crit}}$.

Similar to the flapwise motion, the axial compression induced by the tip mass has a significant influence on the onset of instability. Increasing the tip mass consistently lowers $\Omega_{\text{crit}}$, particularly for shorter beams where the effect is most pronounced. At larger beam lengths, however, the influence of mass becomes less significant, and the curves converge, showing that slenderness dominates the instability behaviour.

For the ETHZ case ($M = 2.1\,\text{kg}$, $L = 1.0\,\text{m}$ m), the critical angular velocity is estimated to be around $60.4$ rad/s using a static buckling analysis, which is well above the centrifuge operating speed of $16.74$ rad/s indicating that the chordwise motion of the ETHZ configuration remains stable within the centrifuge's operational range.

The critical angular velocities of chordwise bending are consistently lower than those of flapwise bending. This makes chordwise bending the more critical direction for stability, as it governs the earliest onset of divergence instability. The reason for this behaviour lies in the governing equations of motion. Although the Coriolis coupling term contributes very little, the chordwise direction includes an additional softening term of the form $-\rho A\Omega^2 w$. This extra destabilising contribution shifts the onset of instability to lower angular velocities compared to the flapwise case.

From a design perspective, this suggests that chordwise stability must be carefully considered in centrifuge modelling. Even if flapwise bending appears sufficiently stable, the chordwise direction may control the actual limit state and therefore cannot be neglected.

### Influence of Moment of Inertia of the cross-section

The influence of bending stiffness was examined by reducing the moment of inertia of the beam by a factor of $15$. As shown in Fig. 4.8 this reduction lowers the critical angular velocity of the ETHZ reference case ($M = 2.1\,\text{kg}$, $L = 1.0\,\text{m}$) to approximately $17\,\text{rad}\,\text{s}^{-1}$, which is very close to the centrifuge's maximum operating speed.

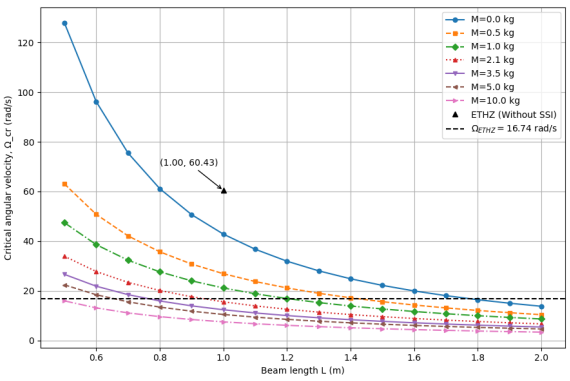


**(a)** Linear scale

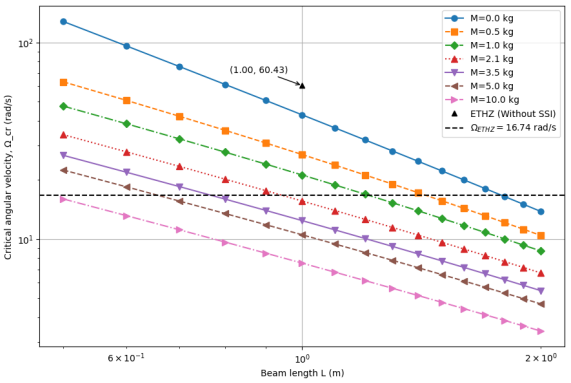


**(b)** Log–log scale

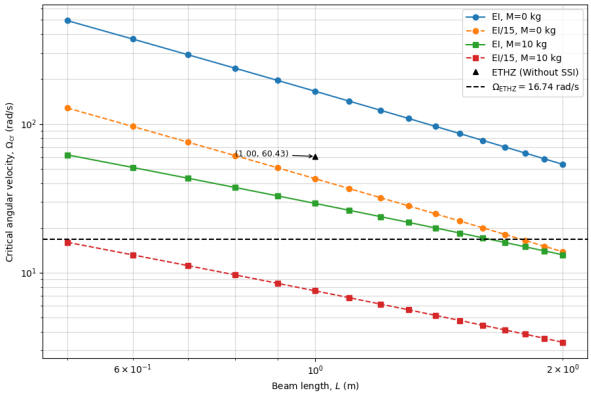


**(c)** Comparison between $EI$ and $EI/15$ (Log–log scale)

**Figure 4.8:** Chordwise motion – Influence of Moment of Inertia of the cross-section on $\Omega_{\text{crit}}$.

The behaviour is consistent with the flapwise case: a lower stiffness reduces the beam's ability to resist axial compression, thereby shifting the onset of divergence instability to much lower angular velocities. This highlights the critical role of structural stiffness in maintaining stability, as even moderate reductions in $I$ can significantly narrow the safety margin during centrifuge operation.

### Influence of SSI

To determine whether flutter-type instability is possible due to the inclusion of SSI, three cases of spring stiffnesses are considered for the soil, one corresponding to the ETHZ case ($E = 28\,\text{MPa}$ at $d = 0.09\,\text{m}$), and the other corresponding to an extremely soft soil ($E = 0.1\,\text{MPa}$ at $d = 0.025\,\text{m}$) and a dynamic stability analysis is performed using numerical techniques. Fig. 4.9 shows the evolution of the first eigenfrequency for both cases as a function of angular velocity. It can be noticed that divergence stability is still dominant, and coupling of displacement fields can be neglected. A static buckling analysis of chordwise bending motion estimates the critical angular velocity for divergence instability as $13.536\,\text{rad}\,\text{s}^{-1}$, which is the same as the plot.

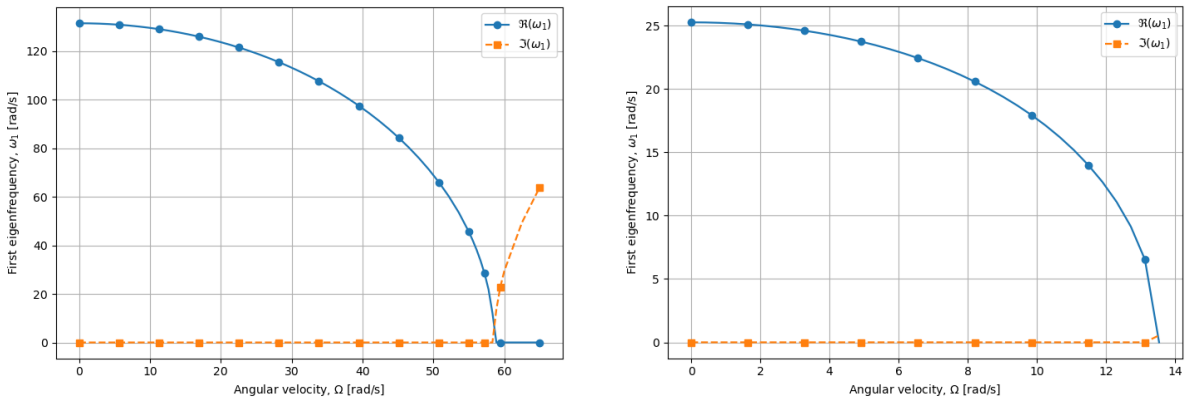


**(a)** ETHZ Case, $E = 28\,\mathrm{MPa}$ at $d = 0.09\,\mathrm{m}$ below GL

**(b)** ETHZ Case, $E = 0.1\,\mathrm{MPa}$ at $d = 0.025\,\mathrm{m}$ below GL

**Figure 4.9:** Chordwise motion – Influence of SSI on $\Omega_{\text{crit}}$.

The effect of various soil profiles, as shown in Table 4.2, on the instability of chordwise motion is shown in the Table 4.6

**Table 4.6:** Chordwise motion - $\Omega_{\text{crit}}$ for ETHZ case for different soil profiles ($E = 28\,\mathrm{MPa}$ at $0.09\,\mathrm{m}$ below the ground level).

| | Constant | Linear | Parabolic | Without SSI |
|---|---|---|---|---|
| $\Omega_{\text{crit}}$ (Rad/sec) | 58.570 | 59.085 | 58.582 | 60.428 |

The effect of SSI on the onset of divergence instability of chordwise motion is examined in Fig. 4.10, where the critical angular velocity is plotted as a function of the beam length, $L$, and the tip mass, $M$, for the parabolic soil profile with $E = 28\,\mathrm{MPa}$ at a depth of $0.09\,\mathrm{m}$ below the ground level.

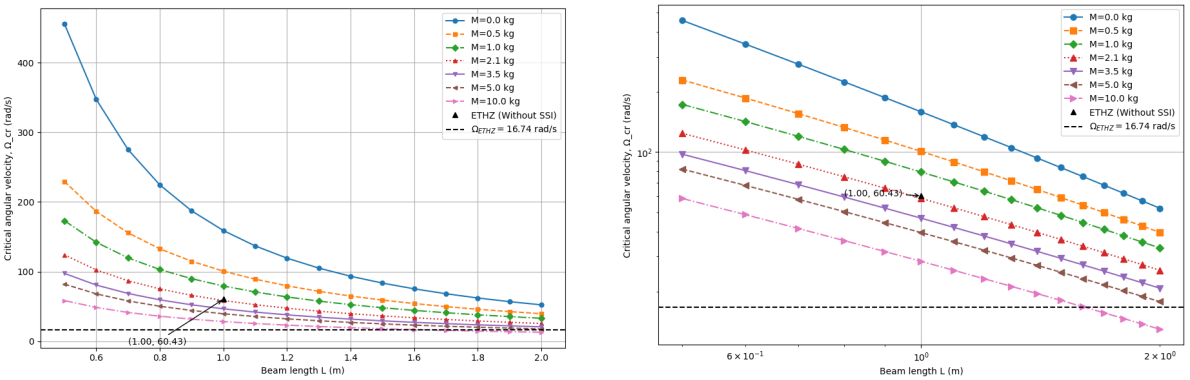


**(a)** Linear scale

**(b)** Log–log scale

**Figure 4.10:** Chordwise motion – Effect of SSI on $\Omega_{\text{crit}}$ for $E = 28\,\mathrm{MPa}$ at a depth of $0.09\,\mathrm{m}$ below the GL.

The overall behaviour is very similar to the flapwise case. SSI slightly reduces the critical angular velocity compared to the fixed-base condition, but the dominant influence remains the combined effect of tip mass and beam length. The reduction due to SSI is relatively small, indicating that foundation flexibility has only a secondary role in chordwise stability for the soil stiffnesses considered here.

## 4.4. Conclusions

In this chapter, the mathematical model developed before is applied to the small-scale model of an OWT tested at the centrifuge facility of ETH Zürich. Stability of both flapwise and chordwise motions is

studied under different parameter variations. The main findings are as follows:

- The maximum allowed centrifuge operating speed at ETH Zürich ($\Omega_{ETHZ} = 16.74\,\mathrm{rad\,s^{-1}}$) is well below the critical velocities for both flapwise and chordwise motions, meaning the model is stable under normal testing conditions.
- Flapwise motion experiences divergence type of instability at about $\Omega \approx 67\,\mathrm{rad\,s^{-1}}$ without SSI, and at slightly lower values when SSI is included. Tip mass and beam length are the dominant factors, while SSI only causes a small reduction in critical velocity (about $2-7\%$). In very soft soil, however, SSI can lower the stability limit enough to fall within the centrifuge's operating range.
- Chordwise motion is more critical, with the first bending mode becoming experiencing divergence instability at about $\Omega \approx 60\,\mathrm{rad\,s^{-1}}$. Similar to the flapwise motion, tip mass and beam length have strong effects, while SSI has only a minor influence. The additional negative stiffness term in the chordwise equations makes this direction less stable than flapwise bending.
- The Coriolis effect does not play a role, even in extreme cases of tip mass and soil stiffness. Instead, divergence remains the dominant form of instability across all examined conditions.
- Reducing the bending stiffness of the beam significantly lowers the critical velocity, showing that cross-sectional properties strongly control stability.

# 5

# Conclusions and Recommendations

In this chapter, the main conclusions of this thesis are summarised, and recommendations for future work are provided.

## 5.1. Conclusions

In this thesis, the stability of a rotating cantilever beam inside a geotechnical centrifuge is studied, with the aim of understanding the onset of instability for dynamically sensitive small-scale models such as monopile-founded OWTs. The main conclusions are:

- A mathematical model was developed in a non-inertial frame of reference using rigorous mathematical derivation. The use of Lagrangian formalism was particularly beneficial, as it directly incorporates the Coriolis effect without approximation. This approach produced a linear set of governing equations that capture centrifugal and Coriolis forces, tip mass effects, and soil–structure interaction (SSI), and can be used to predict the onset of instability. Expressing the equations in a dimensionless form reduced the number of parameters and made the results general.
- The stability analysis showed that:
  - Flapwise motion is governed by divergence instability, and can be assessed using static considerations.
  - In chordwise motion, the axial and lateral degrees of freedom are coupled through the Coriolis term. This coupling requires a dynamic stability analysis, since flutter is theoretically possible. However, the results show that divergence dominates and flutter does not occur under the studied conditions.
  - Because of the coupling terms and the quadratic nature of the axial compression force $T(x)$, numerical techniques are needed to obtain reliable stability limits.
  - Increasing tip mass, beam length, and centrifuge radius consistently reduces the critical angular velocity, while higher bending stiffness increases stability.
- The Coriolis effect was found to play only a minor role, even in extreme cases of tip mass and soil stiffness. This means that established scaling laws can still be used for dynamically sensitive structures, provided that the small-scale model remains stable. If, however, the centrifuge operates beyond a certain angular velocity, the eigenproperties of the small-scale model may start to deviate from those of the prototype due to softening effects from centrifugal forces.
- The case study of the ETH Zürich centrifuge confirmed that the operating speed ($\Omega_{ETHZ} = 16.74$ rad/s) is well below the critical angular velocities for both flapwise and chordwise motions. Thus, the small-scale model remains stable under normal testing conditions. However, in extreme cases with very soft soils or reduced stiffness, the critical velocity may drop close to the centrifuge's operating range.

Overall, this work demonstrates that divergence governs the onset of instability for rotating cantilever beams inside a centrifuge. Chordwise bending is the most critical mode, while SSI and Coriolis effects only play secondary roles under typical conditions.

## 5.2. Recommendations for Future Studies

While this study provides new insights into the stability of rotating beams in centrifuge testing, further work is needed to improve physical realism and strengthen practical application. The following recommendations are made:

1. Nonlinear analysis: This thesis focused on the linear regime and only identified the onset of instability. Future research should explore nonlinear behaviour to capture post-buckling responses and vibration amplitudes after instability occurs.
2. Experimental validation: The results should be compared with actual centrifuge tests on small-scale OWT models. This would confirm the theoretical predictions and improve confidence in applying the model to real structures.
3. Improved SSI modelling: The lumped spring model used here simplifies the soil response. Future work should:
    - Use a distributed spring model (beam on elastic foundation) to capture continuous soil–structure interaction, which would introduce additional interface conditions.
    - Consider dynamic spring stiffnesses, which may become important when axial and lateral degrees of freedom are coupled.
4. Refined small-scale turbine modelling: The current approach idealized the nacelle assembly as a single concentrated tip mass. A more detailed model could represent the nacelle and rotor as multiple discrete point masses, which would better capture the true dynamics and preserve the eigenproperties of the full-scale prototype. While this adds more interface conditions and coupled equations, it provides a more accurate representation of the physical system.

# References


[1] A. Andrei. *Variational Methods and the Euler–Lagrange Equations*. Lecture slides. Unpublished. 2025.

[2] L. Arany et al. “An analytical model to predict the natural frequency of offshore wind turbines on three-spring flexible foundations using two different beam models”. In: *Soil Dynamics and Earthquake Engineering* 74 (2015), pp. 40–45. DOI: 10.1016/j.soildyn.2015.03.007.

[3] Carbon Trust. *Design of Offshore Monopiles Including Seismic Interaction with Soil (DONISIS)*. Accessed: 2025-09-20. 2024. URL: https://www.carbontrust.com/our-work-and-impact/impact-stories/large-scale-rd-projects-offshore-wind/design-of-offshore-monopiles-including-seismic-interaction-with-soil-donisis.

[4] J. Chung and H. H. Yoo. “Dynamic analysis of a rotating cantilever beam by using the finite element method”. In: *Journal of Sound and Vibration* 249.1 (2002), pp. 147–164. DOI: 10.1006/jsvi.2001.3856.

[5] G. Gazetas. “Foundation vibrations”. In: *Foundation engineering handbook*. Ed. by H.Y. Fang. 2nd. Van Nostrand Reinhold, 1991. Chap. 15.

[6] S. M. Han, H. Benaroya, and T. Wei. “Dynamics of transversely vibrating beams using four engineering theories”. In: *Journal of Sound and Vibration* 225.5 (1999), pp. 935–988. DOI: 10.1006/jsvi.1999.2257.

[7] S. Iai, T. Tobita, and T. Nakahara. “Generalised scaling relations for dynamic centrifuge tests”. In: *Géotechnique* 55.5 (2005), pp. 355–362. DOI: 10.1680/geot.2005.55.5.355.

[8] T. R. Kane, R. R. Ryan, and A. K. Banerjee. “Dynamics of a cantilever beam attached to a moving base”. In: *Journal of Guidance Control and Dynamics* 10.2 (1987), pp. 139–151. DOI: 10.2514/3.20195.

[9] M. A. C. F. Lima. “Rotating Cantilever Beams: Finite Element Modeling and Vibration Analysis”. Master’s thesis. University of Porto, 2013. URL: https://repositorio-aberto.up.pt/bitstream/10216/68449/1/000154284.pdf.

[10] Gopal Madabhushi. *Centrifuge Modelling for Civil Engineers*. Boca Raton, FL: CRC Press, 2014. ISBN: 978-1-138-02616-6.

[11] Leonard Meirovitch. *Analytical Methods in Vibrations*. New York: Macmillan, 1967.

[12] Leonard Meirovitch. *Dynamics and Control of Structures*. New York: Wiley, 1990.

[13] S. Naguleswaran. “Lateral vibration of a centrifugally tensioned uniform Euler–Bernoulli beam”. In: *Journal of Sound and Vibration* 176.5 (1994), pp. 613–624. DOI: 10.1006/jsvi.1994.1402.

[14] Upendra Kumar Sah and Jun Yang. “Importance of higher modes for dynamic soil–structure interaction of monopile-supported offshore wind turbines”. In: *Earthquake Engineering & Structural Dynamics* 53.3 (2024), pp. 742–760. DOI: 10.1002/eqe.4095.

[15] A. N. Schofield. “Cambridge Geotechnical Centrifuge Operations”. In: *Géotechnique* 30.3 (1980), pp. 227–268. DOI: 10.1680/geot.1980.30.3.227.

[16] H. H. Yoo, R. R. Ryan, and R. A. Scott. “Dynamics of flexible beams undergoing overall motions”. In: *Journal of Sound and Vibration* 181.2 (1995), pp. 261–278. DOI: 10.1006/jsvi.1995.0139.

[17] H. H. Yoo and S. H. Shin. “Vibration analysis of rotating cantilever beams”. In: *Journal of Sound and Vibration* 212.5 (1998), pp. 807–828. DOI: 10.1006/jsvi.1997.1469.

# A

# Euler-Lagrange Equations

This appendix presents the derivation of the Euler-Lagrange equations and the natural boundary conditions for 1D elements based on Hamilton's principle. The resulting equations are subsequently applied to derive the governing equations that describe the motion of a rotating cantilever beam inside a geotechnical centrifuge, as presented in Chapter 2.

## A.1. Hamilton's Principle and the Action Functional

Hamilton's principle [1] asserts that the dynamics of a mechanical system are governed by a variational problem for a functional based on a single function, the Lagrangian, which contains all physical information about the system and the forces acting upon it. This variational problem is equivalent to and allows for the derivation of the differential equations that describe the motion of the mechanical system.

The Lagrange function, $L$, is defined as the difference between the kinetic energy, $K$, and the potential energy, $P$, of the system, at any particular instant of time. The action functional, $S$, which considers the entire motion of the system between two time instants $t_1$ and $t_2$ is obtained by integrating the Lagrange function.

$$S\big(\mathbf{q}(t)\big) = \int_{t_1}^{t_2} L\big(\mathbf{q}(t), \dot{\mathbf{q}}(t), t\big)\, dt$$

where $\mathbf{q}(t)$ denotes the vector of degrees of freedom describing the motion of the system and $\dot{\mathbf{q}}(t)$ is its time derivative.

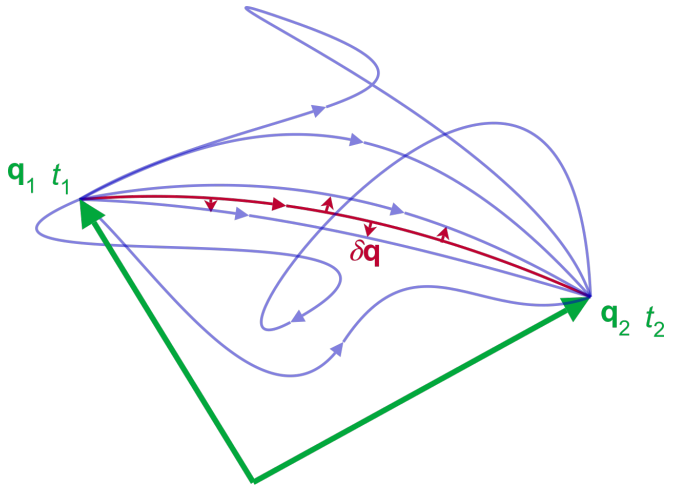


**Figure A.1:** Illustration of the principle of stationary (least) action: the true path (in red) produces $\delta S = 0$.

The action functional, $S$, depends on the Lagrange function, $L$, which in turn depends on the path taken by the system, $\mathbf{q}(t)$. Therefore, $S$, can be theoretically evaluated for any choice of path. Hamilton's principle states that, as the system evolves, $\mathbf{q}$ follows a path through the configurational space and the path taken by the system (red) as shown in Fig. A.1 has a stationary action, meaning, $\delta S = 0$, for small changes in the configuration of the system, $\delta\mathbf{q}$. This path is defined as the 'true path' or the 'stationary path'. Physically, this means the system chooses to move from one equilibrium state to another in a specific path such that it spends the least amount of energy. The mathematical statement of Hamilton's principle is as follows:

$$\frac{\delta S}{\delta \mathbf{q}(t)} = 0$$

## A.2. Action Functional for 1D System with Discrete End Attachments

Consider a 1D system occupying the domain, $x \in [a, b]$, with discrete end attachments at the boundaries $x = a, b$. Here, $x$ denotes the spatial variable along the undeformed length of the system, and $t$ represents time. Let $w(x, t)$ denote the unknown path of the system. The action functional is given by

$$\begin{aligned} S = &\int_{t_1}^{t_2} \int_a^b \left(\lambda\left(t, x, w(x,t), w_{,x}(x,t), w_{,t}(x,t), w_{,xx}(x,t), w_{,xt}(x,t)\right)\right) dx\, dt \\ &+ \int_{t_1}^{t_2} \left(L_{aw}(t, w(a,t), w_{,t}(a,t)) + L_{bw}(t, w(b,t), w_{,t}(b,t))\right) dt \\ &+ \int_{t_1}^{t_2} \left(L_{a\varphi}(t, w_{,x}(a,t), w_{,xt}(a,t)) + L_{b\varphi}(t, w_{,x}(b,t), w_{,xt}(b,t))\right) dt \end{aligned}$$

Here, $\lambda$ is the linear density of the Lagrange function, i.e., Lagrange function per unit length. The terms $L_{aw}, L_{aw_{,x}}, L_{bw}, L_{bw_{,x}}$ are the Lagrange functions of the discrete end attachments at $x = a$ and $x = b$, and $w(x, t)$ represents the stationary path, which is unknown and needs to be determined. The following notations are used in the above expression.

$$w_{,t} = \frac{\partial w}{\partial t}, \quad w_{,x} = \frac{\partial w}{\partial x}, \quad w_{,xx} = \frac{\partial^2 w}{\partial x^2}, \quad w_{,xt} = \frac{\partial^2 w}{\partial x \partial t},$$

## A.3. Derivation of the Euler-Lagrange Equations

Let $\tilde{w}(x, t)$ represent a varied path allowing for a small deviation, $\varepsilon$, from the stationary path, $\tilde{w}(x, t)$. The action functional, $\tilde{S}$, for the varied path, $\tilde{w}(x, t)$, is given by

$$\begin{aligned} \tilde{S} = &\int_{t_1}^{t_2} \int_a^b \left(\lambda\left(t, x, \tilde{w}(x,t), \tilde{w}_{,x}(x,t), \tilde{w}_{,t}(x,t), \tilde{w}_{,xx}(x,t), \tilde{w}_{,xt}(x,t)\right)\right) dx\, dt \\ &+ \int_{t_1}^{t_2} \left(L_{aw}(t, \tilde{w}(a,t), \tilde{w}_{,t}(a,t)) + L_{bw}(t, \tilde{w}(b,t), \tilde{w}_{,t}(b,t))\right) dt \\ &+ \int_{t_1}^{t_2} \left(L_{a\varphi}(t, \tilde{w}_{,x}(a,t), \tilde{w}_{,xt}(a,t)) + L_{b\varphi}(t, \tilde{w}_{,x}(b,t), \tilde{w}_{,xt}(b,t))\right) dt \end{aligned} \tag{A.1}$$

As per Hamilton's principle, for small variations, $\varepsilon$, around the stationary path, the change in the action functional shall be zero. Mathematically, it can be written as

$$\left.\frac{d\tilde{S}}{d\varepsilon}\right|_{\varepsilon=0} = 0 \tag{A.2}$$

Substituting the action functional as shown in Eq. (A.1) into the Eq. (A.2) and applying the chain rule of differentiation leads to

$$\begin{aligned}
&\int_{t_1}^{t_2}\int_a^b \left[\frac{\partial\lambda}{\partial\tilde{w}}\frac{\partial\tilde{w}}{\partial\varepsilon} + \frac{\partial\lambda}{\partial\tilde{w}_{,x}}\frac{\partial\tilde{w}_{,x}}{\partial\varepsilon} + \frac{\partial\lambda}{\partial\tilde{w}_{,t}}\frac{\partial\tilde{w}_{,t}}{\partial\varepsilon} + \frac{\partial\lambda}{\partial\tilde{w}_{,xx}}\frac{\partial\tilde{w}_{,xx}}{\partial\varepsilon} + \frac{\partial\lambda}{\partial\tilde{w}_{,xt}}\frac{\partial\tilde{w}_{,xt}}{\partial\varepsilon}\right] dx\,dt \\
&+ \int_{t_1}^{t_2}\left[\frac{\partial L_{aw}}{\partial\tilde{w}(a,t)}\frac{\partial\tilde{w}(a,t)}{\partial\varepsilon} + \frac{\partial L_{aw}}{\partial\tilde{w}_{,t}(a,t)}\frac{\partial\tilde{w}_{,t}(a,t)}{\partial\varepsilon} + \frac{\partial L_{bw}}{\partial\tilde{w}(b,t)}\frac{\partial\tilde{w}(b,t)}{\partial\varepsilon} + \frac{\partial L_{bw}}{\partial\tilde{w}_{,t}(b,t)}\frac{\partial\tilde{w}_{,t}(b,t)}{\partial\varepsilon}\right] dt \\
&+ \int_{t_1}^{t_2}\left[\frac{\partial L_{a\varphi}}{\partial\tilde{w}_{,x}(a,t)}\frac{\partial\tilde{w}_{,x}(a,t)}{\partial\varepsilon} + \frac{\partial L_{a\varphi}}{\partial\tilde{w}_{,xt}(a,t)}\frac{\partial\tilde{w}_{,xt}(a,t)}{\partial\varepsilon}\right] dt \\
&+ \int_{t_1}^{t_2}\left[\frac{\partial L_{b\varphi}}{\partial\tilde{w}_{,x}(b,t)}\frac{\partial\tilde{w}_{,x}(b,t)}{\partial\varepsilon} + \frac{\partial L_{b\varphi}}{\partial\tilde{w}_{,xt}(b,t)}\frac{\partial\tilde{w}_{,xt}(b,t)}{\partial\varepsilon}\right] dt = 0
\end{aligned} \tag{A.3}$$

The varied path is defined as $\tilde{w}(x,t) = w(x,t) + \varepsilon\,\xi(x,t)$, where $\xi(x,t)$ is an arbitrary variation and $\varepsilon \in \mathbb{R}$ is a small scalar parameter, representing the deviation from the stationary path. For $\varepsilon = 0$, the varied path coincides with the stationary one, i.e.,

$$\tilde{w}(x,t) = w(x,t), \quad \tilde{w}_{,x}(x,t) = w_{,x}(x,t), \quad \tilde{w}_{,t}(x,t) = w_{,t}(x,t), \quad \text{etc. for } \varepsilon = 0$$

and the derivative terms of the varied path simplify as:

$$\frac{\partial\tilde{w}}{\partial\varepsilon} = \xi(x,t), \quad \frac{\partial\tilde{w}_{,x}}{\partial\varepsilon} = \xi_{,x}(x,t), \quad \frac{\partial\tilde{w}_{,t}}{\partial\varepsilon} = \xi_{,t}(x,t), \quad \text{etc. for } \varepsilon = 0$$

Introducing above relations into Eq. (A.3), one obtains

$$\begin{aligned}
&\int_{t_1}^{t_2}\int_a^b \left[\frac{\partial\lambda}{\partial w}\xi + \frac{\partial\lambda}{\partial w_{,x}}\xi_{,x} + \frac{\partial\lambda}{\partial w_{,t}}\xi_{,t} + \frac{\partial\lambda}{\partial w_{,xx}}\xi_{,xx} + \frac{\partial\lambda}{\partial w_{,xt}}\xi_{,xt}\right] dx\,dt \\
&+ \int_{t_1}^{t_2}\left[\frac{\partial L_{aw}}{\partial w(a,t)}\xi(a,t) + \frac{\partial L_{aw}}{\partial w_{,t}(a,t)}\xi_{,t}(a,t) + \frac{\partial L_{bw}}{\partial w(b,t)}\xi(b,t) + \frac{\partial L_{bw}}{\partial w_{,t}(b,t)}\xi_{,t}(b,t)\right] dt \\
&+ \int_{t_1}^{t_2}\left[\frac{\partial L_{a\varphi}}{\partial w_{,x}(a,t)}\xi_{,x}(a,t) + \frac{\partial L_{a\varphi}}{\partial w_{,xt}(a,t)}\xi_{,xt}(a,t) + \frac{\partial L_{b\varphi}}{\partial w_{,x}(b,t)}\xi_{,x}(b,t) + \frac{\partial L_{b\varphi}}{\partial w_{,xt}(b,t)}\xi_{,xt}(b,t)\right] dt = 0
\end{aligned} \tag{A.4}$$

Using the chain rule of differentiation to each term to isolate $\xi$, $\xi_{,x}$, $\xi_{,t}$:

$$\begin{aligned}
\frac{\partial}{\partial x}\left(\frac{\partial\lambda}{\partial w_{,x}}\xi\right) &= \frac{\partial}{\partial x}\left(\frac{\partial\lambda}{\partial w_{,x}}\right)\xi + \frac{\partial\lambda}{\partial w_{,x}}\xi_{,x} \\
\Rightarrow \frac{\partial\lambda}{\partial w_{,x}}\xi_{,x} &= \frac{\partial}{\partial x}\left(\frac{\partial\lambda}{\partial w_{,x}}\xi\right) - \frac{\partial}{\partial x}\left(\frac{\partial\lambda}{\partial w_{,x}}\right)\xi
\end{aligned}$$

Similarly,

$$\frac{\partial\lambda}{\partial w_{,t}}\xi_{,t} = \frac{\partial}{\partial t}\left(\frac{\partial\lambda}{\partial w_{,t}}\xi\right) - \frac{\partial}{\partial t}\left(\frac{\partial\lambda}{\partial w_{,t}}\right)\xi$$

The chain rule needs to be applied twice on the double derivative term.

$$\begin{aligned}
\frac{\partial}{\partial x}\left(\frac{\partial\lambda}{\partial w_{,xx}}\xi_{,x}\right) &= \frac{\partial\lambda}{\partial w_{,xx}}\xi_{,xx} + \frac{\partial}{\partial x}\left(\frac{\partial\lambda}{\partial w_{,xx}}\right)\xi_{,x} \\
\Rightarrow \frac{\partial\lambda}{\partial w_{,xx}}\xi_{,xx} &= \frac{\partial}{\partial x}\left(\frac{\partial\lambda}{\partial w_{,xx}}\xi_{,x}\right) - \frac{\partial}{\partial x}\left(\frac{\partial\lambda}{\partial w_{,xx}}\right)\xi_{,x}
\end{aligned} \tag{A.5}$$

But,

$$\begin{aligned}
\frac{\partial}{\partial x}\left(\frac{\partial}{\partial x}\frac{\partial\lambda}{\partial w_{,xx}}\xi\right) &= \frac{\partial}{\partial x}\left(\frac{\partial\lambda}{\partial w_{,xx}}\right)\xi_{,x} + \frac{\partial^2}{\partial x^2}\left(\frac{\partial\lambda}{\partial w_{,xx}}\right)\xi \\
\Rightarrow \frac{\partial}{\partial x}\left(\frac{\partial\lambda}{\partial w_{,xx}}\right)\xi_{,x} &= \frac{\partial}{\partial x}\left(\frac{\partial}{\partial x}\frac{\partial\lambda}{\partial w_{,xx}}\xi\right) - \frac{\partial^2}{\partial x^2}\left(\frac{\partial\lambda}{\partial w_{,xx}}\right)\xi
\end{aligned} \tag{A.6}$$

Substituting Eq. (A.6) into Eq. (A.5) yields

$$\frac{\partial\lambda}{\partial w_{,xx}}\,\xi_{,xx} = \frac{\partial}{\partial x}\left(\frac{\partial\lambda}{\partial w_{,xx}}\,\xi_{,x}\right) - \frac{\partial}{\partial x}\left(\frac{\partial}{\partial x}\frac{\partial\lambda}{\partial w_{,xx}}\,\xi\right) + \frac{\partial^2}{\partial x^2}\left(\frac{\partial\lambda}{\partial w_{,xx}}\right)\xi$$

Similarly,

$$\frac{\partial\lambda}{\partial w_{,xt}}\,\xi_{,xt} = \frac{\partial}{\partial t}\left(\frac{\partial\lambda}{\partial w_{,xt}}\,\xi_{,x}\right) - \frac{\partial}{\partial x}\left(\frac{\partial}{\partial t}\frac{\partial\lambda}{\partial w_{,xt}}\,\xi\right) + \frac{\partial^2}{\partial x\partial t}\left(\frac{\partial\lambda}{\partial w_{,xt}}\right)\xi$$

The Lagrange functions of the end attachments are treated in a similar way:

$$\frac{\partial}{\partial t}\left(\frac{\partial L_{aw}}{\partial w_{,t}(a,t)}\,\xi(a,t)\right) = \frac{\partial}{\partial t}\left(\frac{\partial L_{aw}}{\partial w_{,t}(a,t)}\right)\xi(a,t) + \frac{\partial L_{aw}}{\partial w_{,t}(a,t)}\,\xi_{,t}(a,t)$$

$$\Rightarrow \frac{\partial L_{aw}}{\partial w_{,t}(a,t)}\,\xi_{,t}(a,t) = \frac{\partial}{\partial t}\left(\frac{\partial L_{aw}}{\partial w_{,t}(a,t)}\,\xi(a,t)\right) - \frac{\partial}{\partial t}\left(\frac{\partial L_{aw}}{\partial w_{,t}(a,t)}\right)\xi(a,t)$$

Similarly,

$$\frac{\partial L_{bw}}{\partial w_{,t}(b,t)}\,\xi_{,t}(b,t) = \frac{\partial}{\partial t}\left(\frac{\partial L_{bw}}{\partial w_{,t}(b,t)}\,\xi(b,t)\right) - \frac{\partial}{\partial t}\left(\frac{\partial L_{bw}}{\partial w_{,t}(b,t)}\right)\xi(b,t)$$

$$\frac{\partial L_{a\varphi}}{\partial w_{,xt}(a,t)}\,\xi_{,xt}(a,t) = \frac{\partial}{\partial t}\left(\frac{\partial L_{a\varphi}}{\partial w_{,xt}(a,t)}\,\xi_{,x}(a,t)\right) - \frac{\partial}{\partial t}\left(\frac{\partial L_{a\varphi}}{\partial w_{,xt}(a,t)}\right)\xi_{,x}(a,t)$$

$$\frac{\partial L_{b\varphi}}{\partial w_{,xt}(b,t)}\,\xi_{,xt}(b,t) = \frac{\partial}{\partial t}\left(\frac{\partial L_{b\varphi}}{\partial w_{,xt}(b,t)}\,\xi_{,x}(b,t)\right) - \frac{\partial}{\partial t}\left(\frac{\partial L_{b\varphi}}{\partial w_{,xt}(b,t)}\right)\xi_{,x}(b,t)$$

Substituting all the above expressions into Eq. (A.4) produces

$$\begin{aligned}
&\int_{t_1}^{t_2}\int_a^b \Bigg[\frac{\partial\lambda}{\partial w}\,\xi + \frac{\partial}{\partial x}\left(\frac{\partial\lambda}{\partial w_{,x}}\,\xi\right) - \frac{\partial}{\partial x}\left(\frac{\partial\lambda}{\partial w_{,x}}\right)\xi + \frac{\partial}{\partial t}\left(\frac{\partial\lambda}{\partial w_{,t}}\,\xi\right) - \frac{\partial}{\partial t}\left(\frac{\partial\lambda}{\partial w_{,t}}\right)\xi \\
&\qquad + \frac{\partial}{\partial x}\left(\frac{\partial\lambda}{\partial w_{,xx}}\,\xi_{,x}\right) - \frac{\partial}{\partial x}\left(\frac{\partial}{\partial x}\frac{\partial\lambda}{\partial w_{,xx}}\,\xi\right) + \frac{\partial^2}{\partial x^2}\left(\frac{\partial\lambda}{\partial w_{,xx}}\right)\xi \\
&\qquad + \frac{\partial}{\partial t}\left(\frac{\partial\lambda}{\partial w_{,xt}}\,\xi_{,x}\right) - \frac{\partial}{\partial x}\left(\frac{\partial}{\partial t}\frac{\partial\lambda}{\partial w_{,xt}}\,\xi\right) + \frac{\partial^2}{\partial x\partial t}\left(\frac{\partial\lambda}{\partial w_{,xt}}\right)\xi\Bigg]\,dx\,dt \\
&+ \int_{t_1}^{t_2}\Bigg[\frac{\partial L_{aw}}{\partial w(a,t)}\,\xi(a,t) + \frac{\partial}{\partial t}\left(\frac{\partial L_{aw}}{\partial w_{,t}(a,t)}\,\xi(a,t)\right) - \frac{\partial}{\partial t}\left(\frac{\partial L_{aw}}{\partial w_{,t}(a,t)}\right)\xi(a,t) \\
&\qquad + \frac{\partial L_{bw}}{\partial w(b,t)}\,\xi(b,t) + \frac{\partial}{\partial t}\left(\frac{\partial L_{bw}}{\partial w_{,t}(b,t)}\,\xi(b,t)\right) - \frac{\partial}{\partial t}\left(\frac{\partial L_{bw}}{\partial w_{,t}(b,t)}\right)\xi(b,t)\Bigg]\,dt \\
&+ \int_{t_1}^{t_2}\Bigg[\frac{\partial L_{a\varphi}}{\partial w_{,x}(a,t)}\,\xi_{,x}(a,t) + \frac{\partial}{\partial t}\left(\frac{\partial L_{a\varphi}}{\partial w_{,xt}(a,t)}\,\xi_{,x}(a,t)\right) - \frac{\partial}{\partial t}\left(\frac{\partial L_{a\varphi}}{\partial w_{,xt}(a,t)}\right)\xi_{,x}(a,t) \\
&\qquad + \frac{\partial L_{b\varphi}}{\partial w_{,x}(b,t)}\,\xi_{,x}(b,t) + \frac{\partial}{\partial t}\left(\frac{\partial L_{b\varphi}}{\partial w_{,xt}(b,t)}\,\xi_{,x}(b,t)\right) - \frac{\partial}{\partial t}\left(\frac{\partial L_{b\varphi}}{\partial w_{,xt}(b,t)}\right)\xi_{,x}(b,t)\Bigg]\,dt = 0
\end{aligned} \tag{A.7}$$

Expanding the terms with time derivatives in the Eq. (A.7) gives,

$$\begin{aligned}
\int_{t_1}^{t_2}\int_a^b \frac{\partial}{\partial t}\left(\frac{\partial\lambda}{\partial w_{,t}}\,\xi\right)dx\,dt &= \int_a^b\left[\int_{t_1}^{t_2}\frac{\partial}{\partial t}\left(\frac{\partial\lambda}{\partial w_{,t}}\,\xi\right)dt\right]dx \\
&= \int_a^b\left[\frac{\partial\lambda}{\partial w_{,t}}\,\xi\Big|_{t=t_2} - \frac{\partial\lambda}{\partial w_{,t}}\,\xi\Big|_{t=t_1}\right]dx \\
&= \int_a^b\left[\frac{\partial\lambda}{\partial w_{,t}}\Big|_{t=t_2}\xi(x,t_2) - \frac{\partial\lambda}{\partial w_{,t}}\Big|_{t=t_1}\xi(x,t_1)\right]dx
\end{aligned}$$

But the variation of the varied path, $\tilde{w}(x,t)$, at the time instants $t = t_1$ and at $t = t_2$ from the stationary path is zero because the initial and final configurations of the system are known. This means,

$$\xi(x,t)\big|_{t=t_1} = 0 \quad \text{and} \quad \xi(x,t)\big|_{t=t_2} = 0$$
$$\Rightarrow \int_{t_1}^{t_2}\int_a^b \frac{\partial}{\partial t}\left(\frac{\partial \lambda}{\partial w_{,t}}\,\xi\right) dx\,dt = 0$$

Similarly, the following integrals with time derivatives also disappear:

$$\int_{t_1}^{t_2}\int_a^b \frac{\partial}{\partial t}\left(\frac{\partial \lambda}{\partial w_{,t}}\,\xi\right) dx\,dt = 0; \quad \int_{t_1}^{t_2}\int_a^b \frac{\partial}{\partial t}\left(\frac{\partial \lambda}{\partial w_{,xt}}\,\xi_{,x}\right) dx\,dt = 0$$

$$\int_{t_1}^{t_2} \frac{\partial}{\partial t}\left(\frac{\partial L_{aw}}{\partial w_{,t}(a,t)}\,\xi(a,t)\right) dt = 0; \quad \int_{t_1}^{t_2} \frac{\partial}{\partial t}\left(\frac{\partial L_{bw}}{\partial w_{,t}(b,t)}\,\xi(b,t)\right) dt = 0$$

$$\int_{t_1}^{t_2} \frac{\partial}{\partial t}\left(\frac{\partial L_{a\varphi}}{\partial w_{,xt}(a,t)}\,\xi_{,x}(a,t)\right) dt = 0; \quad \int_{t_1}^{t_2} \frac{\partial}{\partial t}\left(\frac{\partial L_{b\varphi}}{\partial w_{,xt}(b,t)}\,\xi_{,x}(b,t)\right) dt = 0$$

Expanding the terms with space derivatives in the Eq. (A.7) gives

$$\begin{aligned}\int_{t_1}^{t_2}\int_a^b \frac{\partial}{\partial x}\left(\frac{\partial \lambda}{\partial w_{,x}}\,\xi\right) dx\,dt &= \int_{t_1}^{t_2}\left[\int_a^b \frac{\partial}{\partial x}\left[\frac{\partial \lambda}{\partial w_{,x}}\,\xi\right] dx\right] dt \\ &= \int_{t_1}^{t_2}\left[\frac{\partial \lambda}{\partial w_{,x}}\,\xi\Big|_{x=b} - \frac{\partial \lambda}{\partial w_{,x}}\,\xi\Big|_{x=a}\right] dt \\ &= \int_{t_1}^{t_2}\left[\frac{\partial \lambda}{\partial w_{,x}}\Big|_{x=b}\xi(b,t) - \frac{\partial \lambda}{\partial w_{,x}}\Big|_{x=a}\xi(a,t)\right] dt\end{aligned}$$

Similarly,

$$\int_{t_1}^{t_2}\int_a^b \frac{\partial}{\partial x}\left[\frac{\partial \lambda}{\partial w_{,xx}}\,\xi_{,x}\right] dx\,dt = \int_{t_1}^{t_2}\left[\frac{\partial \lambda}{\partial w_{,xx}}\Big|_{x=b}\xi_{,x}(b,t) - \frac{\partial \lambda}{\partial w_{,xx}}\Big|_{x=a}\xi_{,x}(a,t)\right] dt$$

$$\int_{t_1}^{t_2}\int_a^b \frac{\partial}{\partial x}\left[\frac{\partial}{\partial x}\left(\frac{\partial \lambda}{\partial w_{,xx}}\right)\xi\right] dx\,dt = \int_{t_1}^{t_2}\left[\frac{\partial}{\partial x}\left(\frac{\partial \lambda}{\partial w_{,xx}}\right)\Big|_{x=b}\xi(b,t) - \frac{\partial}{\partial x}\left(\frac{\partial \lambda}{\partial w_{,xx}}\right)\Big|_{x=a}\xi(a,t)\right] dt$$

$$\int_{t_1}^{t_2}\int_a^b \frac{\partial}{\partial x}\left[\frac{\partial}{\partial t}\left(\frac{\partial \lambda}{\partial w_{,xt}}\right)\xi\right] dx\,dt = \int_{t_1}^{t_2}\left[\frac{\partial}{\partial t}\left(\frac{\partial \lambda}{\partial w_{,xt}}\right)\Big|_{x=b}\xi(b,t) - \frac{\partial}{\partial t}\left(\frac{\partial \lambda}{\partial w_{,xt}}\right)\Big|_{x=a}\xi(a,t)\right] dt$$

Substituting the above relations into Eq. (A.7), the final variational form of Hamilton's principle is obtained:

$$\begin{aligned}&\int_{t_1}^{t_2}\int_a^b \left[\frac{\partial \lambda}{\partial w} - \frac{\partial}{\partial t}\left(\frac{\partial \lambda}{\partial w_{,t}}\right) - \frac{\partial}{\partial x}\left(\frac{\partial \lambda}{\partial w_{,x}}\right) + \frac{\partial^2}{\partial x^2}\left(\frac{\partial \lambda}{\partial w_{,xx}}\right) + \frac{\partial^2}{\partial x \partial t}\left(\frac{\partial \lambda}{\partial w_{,xt}}\right)\right]\xi\,dx\,dt \\ &+ \int_{t_1}^{t_2}\left[\left(-\frac{\partial \lambda}{\partial w_{,x}}\Big|_{x=a} + \frac{\partial}{\partial x}\left(\frac{\partial \lambda}{\partial w_{,xx}}\right)\Big|_{x=a} + \frac{\partial}{\partial t}\left(\frac{\partial \lambda}{\partial w_{,xt}}\right)\Big|_{x=a} + \frac{\partial L_{aw}}{\partial w(a,t)} - \frac{\partial}{\partial t}\left(\frac{\partial L_{aw}}{\partial w_{,t}(a,t)}\right)\right)\xi(a,t)\right. \\ &+ \left(\frac{\partial \lambda}{\partial w_{,x}}\Big|_{x=b} - \frac{\partial}{\partial x}\left(\frac{\partial \lambda}{\partial w_{,xx}}\right)\Big|_{x=b} - \frac{\partial}{\partial t}\left(\frac{\partial \lambda}{\partial w_{,xt}}\right)\Big|_{x=b} + \frac{\partial L_{bw}}{\partial w(b,t)} - \frac{\partial}{\partial t}\left(\frac{\partial L_{bw}}{\partial w_{,t}(b,t)}\right)\right)\xi(b,t) \\ &+ \left(-\frac{\partial \lambda}{\partial w_{,xx}}\Big|_{x=a} + \frac{\partial L_{a\varphi}}{\partial w_{,x}(a,t)} - \frac{\partial}{\partial t}\left(\frac{\partial L_{a\varphi}}{\partial w_{,xt}(a,t)}\right)\right)\xi_{,x}(a,t) \\ &\left.+ \left(\frac{\partial \lambda}{\partial w_{,xx}}\Big|_{x=b} + \frac{\partial L_{b\varphi}}{\partial w_{,x}(b,t)} - \frac{\partial}{\partial t}\left(\frac{\partial L_{b\varphi}}{\partial w_{,xt}(b,t)}\right)\right)\xi_{,x}(b,t)\right] dt = 0\end{aligned}$$

The above equation shall be valid for any arbitrary $\xi(x,t)$. Hence, it results in the Euler-Lagrange equations as presented below:

## A.4. Euler-Lagrange Equations

**Equation of Motion:** $a < x < b$

$$\frac{\partial \lambda}{\partial w} - \frac{\partial}{\partial t}\left(\frac{\partial \lambda}{\partial w_{,t}}\right) - \frac{\partial}{\partial x}\left(\frac{\partial \lambda}{\partial w_{,x}}\right) + \frac{\partial^2}{\partial x^2}\left(\frac{\partial \lambda}{\partial w_{,xx}}\right) + \frac{\partial^2}{\partial x \partial t}\left(\frac{\partial \lambda}{\partial w_{,xt}}\right) = 0 \tag{A.8}$$

**Natural Boundary Conditions (NBCs):**

At $x = a$ (left end):

$$-\frac{\partial \lambda}{\partial w_{,x}} + \frac{\partial}{\partial x}\left(\frac{\partial \lambda}{\partial w_{,xx}}\right) + \frac{\partial}{\partial t}\left(\frac{\partial \lambda}{\partial w_{,xt}}\right) + \frac{\partial L_{aw}}{\partial w(a,t)} - \frac{\partial}{\partial t}\left(\frac{\partial L_{aw}}{\partial w_{,t}(a,t)}\right) = 0 \tag{A.9}$$

$$-\frac{\partial \lambda}{\partial w_{,xx}} + \frac{\partial L_{a\varphi}}{\partial w_{,x}(a,t)} - \frac{\partial}{\partial t}\left(\frac{\partial L_{a\varphi}}{\partial w_{,xt}(a,t)}\right) = 0 \tag{A.10}$$

At $x = b$ (right end):

$$\frac{\partial \lambda}{\partial w_{,x}} - \frac{\partial}{\partial x}\left(\frac{\partial \lambda}{\partial w_{,xx}}\right) - \frac{\partial}{\partial t}\left(\frac{\partial \lambda}{\partial w_{,xt}}\right) + \frac{\partial L_{bw}}{\partial w(b,t)} - \frac{\partial}{\partial t}\left(\frac{\partial L_{bw}}{\partial w_{,t}(b,t)}\right) = 0 \tag{A.11}$$

$$\frac{\partial \lambda}{\partial w_{,xx}} + \frac{\partial L_{b\varphi}}{\partial w_{,x}(b,t)} - \frac{\partial}{\partial t}\left(\frac{\partial L_{b\varphi}}{\partial w_{,xt}(b,t)}\right) = 0 \tag{A.12}$$

# B

# Lump Spring Model

The monopile is the most commonly used type of foundation in offshore wind turbines (OWTs). These structures are continuously subjected to dynamic loads from wind and waves, which can modify the properties of supporting soil, leading to changes in the stiffness of the foundation. This can shift the natural frequency of the OWT closer to the excitation frequencies, which may potentially lead to resonance. For this reason, soil–structure interaction (SSI) must be taken into account.

To capture a range of offshore site conditions, three typical soil profiles are considered. They differ in the variation of Young's modulus and soil strength with depth. A uniform profile represents over-consolidated clay with nearly constant undrained shear strength and stiffness. A linear profile corresponds to normally consolidated clay, where both parameters increase linearly with depth. A parabolic profile represents sandy soils, where Young's modulus increases parabolically at moderate strain levels. Together, these three cases cover the main soil types typically encountered offshore. For the ETHZ site conditions, the parabolic profile is considered.

Several approaches exist in the literature to model SSI. In this work, a lump spring model [14] is adopted, which is based on the monopile head stiffness at the mudline level. The foundation is modeled using discrete springs that represent different stiffness components. These include a lateral spring ($K_L$), a rotational spring ($K_R$), a cross-coupling spring ($K_{LR}$), and a vertical spring ($K_V$). The stiffness values for $K_L$, $K_R$, $K_{LR}$, and $K_V$ are calculated using the method proposed by Gazetas [5] for slender piles. However, this method has not been validated for very large-diameter monopiles, so its application in such cases should be treated with caution. In this study, static stiffnesses of the foundation are considered, which are typically valid for low-frequency loadings.

The following table, which is reproduced from [14], provides the expressions that are used to calculate the monopile head stiffnesses at the mudline level.

**Table B.1:** Formulation of monopile head stiffness for lump spring model.

| Pile head stiffness | Constant | Linear | Parabolic |
|---|---|---|---|
| $K_L$ | $E_s^d d \left(\frac{E_p}{E_s^d}\right)^{0.21}$ | $0.6E_s^d d \left(\frac{E_p}{E_s^d}\right)^{0.35}$ | $0.8E_s^d d \left(\frac{E_p}{E_s^d}\right)^{0.28}$ |
| $K_R$ | $0.15E_s^d d^3 \left(\frac{E_p}{E_s^d}\right)^{0.75}$ | $0.15E_s^d d^3 \left(\frac{E_p}{E_s^d}\right)^{0.80}$ | $0.15E_s^d d^3 \left(\frac{E_p}{E_s^d}\right)^{0.77}$ |
| $K_{LR}$ | $-0.22E_s^d d^2 \left(\frac{E_p}{E_s^d}\right)^{0.50}$ | $-0.17E_s^d d^2 \left(\frac{E_p}{E_s^d}\right)^{0.60}$ | $-0.24E_s^d d^2 \left(\frac{E_p}{E_s^d}\right)^{0.53}$ |
| $K_V$ | $1.9E_s^d d \left(\frac{L}{d}\right)^{\frac{2}{3}} \left(\frac{E_p}{E_s^d}\right)^{\frac{-\left(\frac{L}{d}\right)}{\left(\frac{E_p}{E_s^d}\right)}}$ | $1.8E_s^d d \left(\frac{L}{d}\right)^{0.55} \left(\frac{E_p}{E_s^d}\right)^{\frac{-\left(\frac{L}{d}\right)}{\left(\frac{E_p}{E_s^d}\right)}}$ | $1.9E_s^d d \left(\frac{L}{d}\right)^{0.60} \left(\frac{E_p}{E_s^d}\right)^{\frac{-\left(\frac{L}{d}\right)}{\left(\frac{E_p}{E_s^d}\right)}}$ |

where $E_s^d$ is the soil Young's modulus at a depth equal to the pile diameter $D_p$. $L = L_e$ and $d = D_p$ are the monopile embedded length and outer diameter, respectively. $E_p$ is the monopile Young's modulus.

# C

# Assumed Modes Method

## C.1. Approximate Methods

In Chapter 2, the mathematical model of a rotating cantilever beam inside a geotechnical centrifuge is derived, which is described by a linear, homogeneous system of equations. The equations mathematically describe a free vibration problem, and hence, the stability of the system can be fully determined by its eigenvalues. The governing equations (Eq. (2.6)) contain non-constant coefficients and coupled degrees of freedom (DOFs), and as a result, closed-form solutions are not available. In such cases, approximate methods provide eigenvalues and eigenvectors required for a stability analysis.

A standard approach is to assume the solution in the form of a finite series of known (assumed) functions with unknown coefficients. This replaces the continuous beam model with an $n$-DOF discrete system. Solving the resulting eigenvalue problem yields $n$ approximate eigenfrequencies and eigenvectors. The assumed functions are generally chosen to satisfy the essential (geometric) boundary conditions, and when possible, the natural boundary conditions as well. Accuracy improves as $n$ increases. A detailed description of approximate methods can be found in [11].

## C.2. Assumed-Modes Method (AMM)

One possibility is to represent the solution of the free vibration problem as a linear combination of modes, which are functions of spatial coordinates, multiplied by time-dependent functions. These assumed modes may satisfy both the geometric and natural boundary conditions at both ends, but not necessarily the governing differential equation. The assumed solution is then substituted into the differential equation, and an eigenvalue problem can be formulated. In the subsequent sections, the AMM is used to perform stability analysis of chordwise motion of the rotating cantilever beam.

## C.3. Chordwise Motion

The governing equations of chordwise motion, which describe the axial and lateral bending motions, are presented again for the reader's convenience. In this representation, the problematic Coriolis terms from the boundary conditions are brought into the governing differential equations using the Dirac delta formulation. This formulation results in decoupled boundary conditions which can be satisfied by the assumed modes. Note that soil-structure interaction is ignored.

Governing Differential Equations:

$$\begin{aligned}
&\rho A\frac{\partial^2 u}{\partial t^2} - 2\rho A\Omega\frac{\partial v}{\partial t} - EA\frac{\partial^2 u}{\partial x^2} - \rho A\Omega^2 u - \delta(x-L)\left(2M\Omega\frac{\partial v}{\partial t}\right) = 0 \\
&\rho A\frac{\partial^2 v}{\partial t^2} + 2\rho A\Omega\frac{\partial u}{\partial t} + EI_z\frac{\partial^4 v}{\partial x^4} + \rho I_z\Omega^2\frac{\partial^2 v}{\partial x^2} + \frac{\partial}{\partial x}\left[T(x)\frac{\partial v}{\partial x}\right] \\
&\qquad - \rho I_z\frac{\partial^4 v}{\partial x^2\partial t^2} - \rho A\Omega^2 v + \delta(x-L)\left(2M\Omega\frac{\partial u}{\partial t}\right) = 0
\end{aligned} \tag{C.1}$$

The boundary conditions at $x = 0$ are

$$u(x,t)\big|_{x=0} = 0, \quad v(x,t)\big|_{x=0} = 0, \quad \text{and} \quad \left.\frac{\partial v(x,t)}{\partial x}\right|_{x=0} = 0 \tag{C.2}$$

The boundary conditions at $x = L$ are

$$\begin{aligned}
&M\frac{\partial^2 u}{\partial t^2} + EA\frac{\partial u}{\partial x} - M\Omega^2 u = 0 \\
&M\frac{\partial^2 v}{\partial t^2} - EI_z\frac{\partial^3 v}{\partial x^3} - M\Omega^2 v - T(L)\frac{\partial v}{\partial x} - \rho I_z\Omega^2\frac{\partial v}{\partial x} + \rho I_z\frac{\partial^3 v}{\partial x\partial t^2} = 0 \\
&- EI_z\frac{\partial^2 v}{\partial x^2} - J\frac{\partial^3 v}{\partial x\partial t^2} = 0
\end{aligned} \tag{C.3}$$

where

$$T(x) = Mr\Omega^2 + \rho A\Omega^2\left[(r+L)(L-x) - \left(\frac{L^2-x^2}{2}\right)\right]$$

The following form of solution is assumed for the axial and lateral bending displacements

$$u(x,t) \;=\; \sum_{j=1}^{N} U_j(x)\, q_j^U(t) \quad \text{and} \quad v(x,t) \;=\; \sum_{j=1}^{N} V_j(x)\, q_j^V(t), \tag{C.4}$$

where $q_j^U(t)$ and $q_j^V(t)$ are the time-dependent generalized coordinates, $U_j(x)$ and $V_j(x)$ are the assumed modes that satisfy the boundary conditions listed in Eq. (C.2) and (C.3), and $N$ is the number of assumed modes. For simplicity, the same $N$ number of modes is assumed for both axial and lateral displacements. Note that these assumed modes do not satisfy the governing differential equations.

Substituting the above solution forms into the governing differential equation of axial motion as shown in Eq. (C.1) gives

$$\begin{aligned}
\sum_{j=1}^{N}\Big[&\rho A\, U_j(x)\,\ddot{q}_j^U(t) - 2\,\rho A\,\Omega\, V_j(x)\,\dot{q}_j^V(t) - EA\, U_j''(x)\, q_j^U(t) \\
&- \rho A\,\Omega^2\, U_j(x)\, q_j^U(t) - \delta(x-L)\left(2M\Omega\, V_j(x)\,\dot{q}_j^V(t)\right)\Big] = 0
\end{aligned}$$

It can be proved that the assumed modes are orthogonal to each other. Using the orthogonality property to eliminate space dependence and utilizing the sifting property of the Dirac function, one obtains

$$\begin{aligned}
\sum_{j=1}^{N}\int_0^L\Big[&\rho A\, U_j(x)U_i(x)\,\ddot{q}_j^U(t) - 2\,\rho A\,\Omega\, V_j(x)U_i(x)\,\dot{q}_j^V(t) - EA\, U_j''(x)U_i(x)\, q_j^U(t) \\
&-\rho A\,\Omega^2\, U_j(x)U_i(x)\, q_j^U(t)\Big]dx - \sum_{j=1}^{N}\left(2M\Omega\, V_j(L)\, U_i(L)\dot{q}_j^V(t)\right) = 0
\end{aligned} \tag{C.5}$$

Applying integration by parts generates the following boundary terms,

$$EA\int_0^L U_j''(x)\,U_i(x)\,dx = EA\Big[\,U_j'(x)\,U_i(x)\,\Big]_0^L - EA\int_0^L U_j'(x)\,U_i'(x)\,dx.$$

But the assumed modes satisfy the boundary conditions. Substituting the assumed solution forms as given in Eq. (C.4) into the boundary conditions of the axial direction (Eq. (C.3) and rearranging gives

$$-EA\,U_j'(L)\,q_j^U = M\,U_j(L)\,\ddot{q}_j^U - M\Omega^2\,U_j(L)\,q_j^U$$

Substituting the above expression in place of the boundary term at $x = L$ in the Eq. (C.5) and noting that $U_i(0) = 0$ gives the final weak form of axial motion.

$$\begin{aligned}&\sum_{j=1}^{N}\int_0^L \Big(\rho A\,U_jU_i\,\ddot{q}_j(t) - 2\rho A\,\Omega\,V_jU_i\,\dot{q}_j(t) + EA\,U_j'U_i'\,q_j(t) - \rho A\,\Omega^2\,U_jU_i\,q_j(t)\Big)\,dx\\ &+\sum_{j=1}^{N}\Big[M\,U_j(L)U_i(L)\,\ddot{q}_j(t) - 2M\Omega\,V_j(L)U_i(L)\,\dot{q}_j(t) - M\Omega^2\,U_j(L)U_i(L)\,q_j(t)\Big] = 0.\end{aligned} \tag{C.6}$$

A similar procedure is used to derive the weak form of the governing differential equation of the lateral bending displacement

$$\begin{aligned}&\sum_{j=1}^{N}\int_0^L \Big(\rho A\,V_jV_i\,\ddot{q}_j + 2\rho A\,\Omega\,U_jV_i\,\dot{q}_j - \rho A\,\Omega^2\,V_jV_i\,q_j + EI\,V_j''V_i''\,q_j - \rho I\,\Omega^2\,V_j'V_i'\,q_j + \rho I\,V_j'V_i'\,\ddot{q}_j\Big)\,dx\\ &+\sum_{j=1}^{N}\Big[J\,V_j'(L)V_i'(L)\,\ddot{q}_j + M\,V_j(L)V_i(L)\,\ddot{q}_j + 2M\Omega\,U_j(L)V_i(L)\,\dot{q}_j - M\Omega^2\,V_j(L)V_i(L)\,q_j\Big] = 0.\end{aligned} \tag{C.7}$$

The two Eqs. (C.6) and (C.7) can be represented in matrix form as

$$\mathbf{M}\,\ddot{\mathbf{Q}}(t) + \mathbf{C}\,\dot{\mathbf{Q}}(t) + \mathbf{K}\,\mathbf{Q}(t) = \mathbf{0}$$

where the generalized time-coordinates are expressed as

$$\mathbf{q}^U(t) = \big[q_1^U(t),\ldots,q_N^U(t)\big]^\top,\quad \mathbf{q}^V(t) = \big[q_1^V(t),\ldots,q_N^V(t)\big]^\top,\quad \text{and}\quad \mathbf{Q}(t) = \begin{bmatrix}\mathbf{q}^U(t)\\ \mathbf{q}^V(t)\end{bmatrix}$$

and the mass, gyroscopic, and stiffness matrices are respectively,

$$\mathbf{M} = \begin{bmatrix}\mathbf{M}_{UU} & \mathbf{0}\\ \mathbf{0} & \mathbf{M}_{VV}\end{bmatrix},\quad \mathbf{C} = \begin{bmatrix}\mathbf{0} & -2\Omega\,\mathbf{G}_{UV}\\ 2\Omega\,\mathbf{G}_{VU} & \mathbf{0}\end{bmatrix},\quad \text{and}\quad \mathbf{K} = \begin{bmatrix}\mathbf{K}_{UU} & \mathbf{0}\\ \mathbf{0} & \mathbf{K}_{VV}\end{bmatrix}.$$

Note that the matrices, $\mathbf{M}$, $\mathbf{C}$, and $\mathbf{K}$ are of size $2N \times 2N$.

The elements of the mass matrices are given by,

$$\begin{aligned}\big(M_{UU}\big)_{ij} &= \int_0^L \rho A\,U_iU_j\,dx + M\,U_i(L)U_j(L),\\ \big(K_{UU}\big)_{ij} &= \int_0^L EA\,U_i'U_j'\,dx - \Omega^2\left(\int_0^L \rho A\,U_iU_j\,dx + M\,U_i(L)U_j(L)\right).\end{aligned}$$

The elements of the stiffness matrices are given by,

$$\begin{aligned}\big(M_{VV}\big)_{ij} &= \int_0^L \big(\rho A\,V_iV_j + \rho I_z\,V_i'V_j'\big)\,dx + M\,V_i(L)V_j(L) + J\,V_i'(L)V_j'(L),\\ \big(K_{VV}\big)_{ij} &= \int_0^L \big(EI_z\,V_i''V_j'' - T(x)\,V_i'V_j'\big)\,dx\\ &\quad - \Omega^2\left(\int_0^L \big(\rho A\,V_iV_j + \rho I_z\,V_i'V_j'\big)\,dx + M\,V_i(L)V_j(L)\right).\end{aligned}$$

The elements of the gyroscopic matrices are given by,

$$\left(G_{UV}\right)_{ij} = \int_0^L \rho A\, U_i V_j\, dx \;+\; M\, U_i(L) V_j(L),$$
$$\left(G_{VU}\right)_{ij} = \int_0^L \rho A\, U_j V_i\, dx \;+\; M\, U_j(L) V_i(L).$$

The next step is to perform an eigenvalue analysis of the matrix equation. However, since $C$ is an unsymmetric matrix, the matrix equation needs to be cast into a first-order state-space form. More details of eigenvalue analysis can be found in [12].

Let $\mathbf{X} = \mathbf{Q}(t)$ and $\mathbf{Y} = \dot{\mathbf{Q}}(t)$ be the state variables. The $2N$ dimensional state vector, $\mathbf{z}(t)$, is then defined as,

$$\mathbf{z}(t) \;=\; \begin{bmatrix} \mathbf{Y} \\ \mathbf{X} \end{bmatrix}$$

The state equations can then be written as

$$\dot{\mathbf{X}} = \mathbf{Y} \quad \text{and} \quad \mathbf{M}\,\dot{\mathbf{Y}} = -\mathbf{C}\,\mathbf{Y} \,-\, \mathbf{K}\,\mathbf{X} \tag{C.8}$$

which can be converted into the following compact form

$$\mathbf{A}\,\dot{\mathbf{z}}(t) \;+\; \mathbf{B}\,\mathbf{z}(t) \;=\; \mathbf{0}$$

with

$$\mathbf{A} = \begin{bmatrix} \mathbf{M} & \mathbf{0} \\ \mathbf{0} & \mathbf{I} \end{bmatrix}, \quad \text{and} \quad \mathbf{B} = \begin{bmatrix} \mathbf{C} & \mathbf{K} \\ -\mathbf{I} & \mathbf{0} \end{bmatrix},$$

The above matrix equation can be rearranged as

$$\dot{z} = \underbrace{\begin{bmatrix} -\mathbf{M}^{-1}\mathbf{C} & -\mathbf{M}^{-1}\mathbf{K} \\ \mathbf{I} & \mathbf{0} \end{bmatrix}}_{\mathbf{F}} z. \tag{C.9}$$

where $\mathbf{F}$ is the $2N \times 2N$ coefficient matrix. The solution of the above equation has the exponential form

$$\mathbf{z}(t) = \mathbf{Z_0}\, e^{st} \tag{C.10}$$

where $s$ is a constant scalar quantity and $\mathbf{Z_0}$ is a constant vector. Introducing the above equation into Eq. (C.9) and dividing by $e^{st}$, the eigenvalue problem is obtained

$$\mathbf{F}\,\mathbf{Z_0} = s\,\mathbf{Z_0} \tag{C.11}$$

The solution of the above equation, in general, can be complex. Therefore, $s$ can be represented as $\sigma + \mathrm{i}\,\omega$, where $\sigma$ and $\omega$ denote the real and imaginary parts of the eigenvalue, $s$, respectively. $\mathrm{i} = \sqrt{-1}$ denotes the imaginary unit. The stability of the system is then determined by the real part, $\sigma$. The system exhibits a divergence type of instability if $\sigma > 0$ and $\omega = 0$, and a flutter type of instability when $\sigma > 0$ and $\omega \neq 0$.

## C.4. Eigenvalue Analysis and Convergence Study

Ten assumed modes are considered for both axial and lateral bending motions to derive the numerical results of the first three eigenvalues of the system. Note that the assumed modes ideally have to satisfy the following equations. Since the boundary conditions depend on $\Omega$, the assumed modes need to be updated as $\Omega$ keeps changing. However, for simplicity, the assumed modes are chosen for $\Omega = 0$.

Governing differential equations of the assumed modes:

$$\rho A\frac{\partial^2 u}{\partial t^2} - EA\frac{\partial^2 u}{\partial x^2} - \rho A\Omega^2 u = 0$$

$$\rho A\frac{\partial^2 v}{\partial t^2} + EI_z\frac{\partial^4 v}{\partial x^4} + \rho I_z\Omega^2\frac{\partial^2 v}{\partial x^2} + Mr\Omega^2\frac{\partial^2 v}{\partial x^2} - \rho I_z\frac{\partial^4 v}{\partial x^2\partial t^2} - \rho A\Omega^2 v = 0$$

The boundary conditions satisfied by the assumed modes at $x = 0$ are

$$u(x,t)\big|_{x=0} = 0, \quad v(x,t)\big|_{x=0} = 0, \quad \text{and} \quad \left.\frac{\partial v(x,t)}{\partial x}\right|_{x=0} = 0$$

The boundary conditions satisfied by the assumed modes at $x = L$ are

$$M\frac{\partial^2 u}{\partial t^2} + EA\frac{\partial u}{\partial x} - M\Omega^2 u = 0$$

$$M\frac{\partial^2 v}{\partial t^2} - EI_z\frac{\partial^3 v}{\partial x^3} - M\Omega^2 v - Mr\Omega^2\frac{\partial v}{\partial x} - \rho I_z\Omega^2\frac{\partial v}{\partial x} + \rho I_z\frac{\partial^3 v}{\partial x\partial t^2} = 0$$

$$-EI_z\frac{\partial^2 v}{\partial x^2} - J\frac{\partial^3 v}{\partial x\partial t^2} = 0$$

Ideally, the assumed modes depend on the $\Omega$ value because the boundary conditions depend on the $\Omega$. However, for simplicity, the assumed modes are chosen based on $\Omega = 0$. Tables C.1, C.2, and C.3 present the value of the imaginary part of the eigenvalue, $\omega$, including the effect of the Coriolis terms. Note that the value of the real part, $\sigma$ is zero. The following conclusions can be drawn

1. As the number of assumed modes increases, the eigenfrequencies converge. Convergence is faster at smaller $\Omega$ values and at near critical $\Omega$, more modes are required for better accuracy.
2. The first three eigenvalues show divergence-type instability, tending to zero at approximately $\Omega \approx 60.43\,\mathrm{rad\,s^{-1}}$, $\Omega \approx 191.36\,\mathrm{rad\,s^{-1}}$, and $\Omega \approx 3232.08\,\mathrm{rad\,s^{-1}}$.
3. For the first two (lateral bending) modes, the AMM with $N = 10$ agrees closely with the numerical results across $\Omega$, with noticeable deviations close to the critical velocities.
4. For the third (axial) mode, AMM and numerical trends differ: AMM shows an initial increase and then a decrease to zero at $\Omega \approx 3232.08\,\mathrm{rad\,s^{-1}}$, while the numerical result decreases monotonically.

**Table C.1:** First eigenfrequency ($\mathrm{rad\,s^{-1}}$) for different values of $\Omega$ for ETHZ case (With the Coriolis terms).

| No. of modes | Angular velocity, $\Omega$ ($\mathrm{rad\,s^{-1}}$) | | | | | |
|---|---|---|---|---|---|---|
| | 0 | 10 | 30 | 50 | 60 | 60.428 |
| 1 | 138.735 | 136.832 | 120.534 | 78.401 | 19.752 | 10.979 |
| 2 | 138.735 | 136.832 | 120.508 | 78.083 | 16.848 | 3.317 |
| 3 | 138.735 | 136.832 | 120.506 | 78.055 | 16.577 | 1.299 |
| 4 | 138.735 | 136.832 | 120.505 | 78.053 | 16.551 | 0.886 |
| 5 | 138.735 | 136.832 | 120.505 | 78.051 | 16.538 | 0.595 |
| 6 | 138.735 | 136.832 | 120.505 | 78.051 | 16.535 | 0.506 |
| 7 | 138.735 | 136.832 | 120.505 | 78.051 | 16.534 | 0.458 |
| 8 | 138.735 | 136.832 | 120.505 | 78.051 | 16.533 | 0.441 |
| 9 | 138.735 | 136.832 | 120.505 | 78.051 | 16.533 | 0.432 |
| 10 | 138.735 | 136.832 | 120.505 | 78.051 | 16.533 | 0.428 |
| Numerical | 138.735 | 136.837 | 120.546 | 78.125 | 16.555 | 0.421 |

**Table C.2:** Second eigenfrequency ($\mathrm{rad\,s^{-1}}$) for different values of $\Omega$ for ETHZ case (With the Coriolis terms).

| No. of modes | Angular velocity, $\Omega$ ($\mathrm{rad\,s^{-1}}$) | | | | | | |
|---|---|---|---|---|---|---|---|
| | 0 | 10 | 60 | 120 | 180 | 191.25 | 191.358 |
| 1 | – | – | – | – | – | – | – |
| 2 | 1882.86 | 1880.18 | 1783.97 | 1448.10 | 581.21 | 179.86 | 173.83 |
| 3 | 1882.86 | 1880.18 | 1783.95 | 1447.71 | 574.70 | 153.48 | 146.41 |
| 4 | 1882.86 | 1880.18 | 1783.88 | 1446.24 | 554.87 | 71.69 | 56.05 |
| 5 | 1882.86 | 1880.18 | 1783.88 | 1446.15 | 553.56 | 62.84 | 44.26 |
| 6 | 1882.86 | 1880.18 | 1783.87 | 1445.99 | 551.80 | 50.05 | 22.96 |
| 7 | 1882.86 | 1880.18 | 1783.87 | 1445.97 | 551.53 | 47.78 | 17.52 |
| 8 | 1882.86 | 1880.18 | 1783.87 | 1445.95 | 551.30 | 45.84 | 11.27 |
| 9 | 1882.86 | 1880.18 | 1783.87 | 1445.94 | 551.24 | 45.33 | 8.98 |
| 10 | 1882.86 | 1880.18 | 1783.87 | 1445.94 | 551.19 | 44.89 | 6.46 |
| Numerical | 1882.86 | 1880.19 | 1783.99 | 1446.37 | 552.58 | 44.78 | 1.65 |

**Table C.3:** Third eigenfrequency ($\mathrm{rad\,s^{-1}}$) for different values of $\Omega$ for ETHZ case (With the Coriolis terms).

| No. of modes | Angular velocity, $\Omega$ ($\mathrm{rad\,s^{-1}}$) | | | | | | | | | |
|---|---|---|---|---|---|---|---|---|---|---|
| | 0 | 10 | 60 | 600 | 1200 | 2400 | 3000 | 3200 | 3232 | 3232.08 |
| 1 | 3232 | 3232 | 3234 | 3363 | 3545 | 3259 | 2152 | 898 | 47 | 12 |
| 2 | 3232 | 3232 | 3234 | 3366 | 3561 | 3335 | 2273 | 987 | 53 | 13 |
| 3 | 3232 | 3232 | 3234 | 3367 | 3566 | 3359 | 2315 | 1023 | 55 | 14 |
| 4 | 3232 | 3232 | 3234 | 3368 | 3569 | 3371 | 2336 | 1041 | 56 | 14 |
| 5 | 3232 | 3232 | 3234 | 3368 | 3570 | 3378 | 2350 | 1053 | 57 | 14 |
| 6 | 3232 | 3232 | 3234 | 3370 | 3572 | 3384 | 2360 | 1062 | 58 | 14 |
| 7 | 3232 | 3232 | 3234 | 3369 | 3573 | 3388 | 2367 | 1070 | 58 | 15 |
| 8 | 3232 | 3232 | 3234 | 3368 | 3573 | 3392 | 2373 | 1075 | 59 | 15 |
| 9 | 3232 | 3232 | 3234 | 3368 | 3575 | 3395 | 2378 | 1080 | 59 | 15 |
| 10 | 3232 | 3232 | 3234 | 3368 | 3578 | 3397 | 2382 | 1083 | 59 | 15 |
| Numerical | 3232 | 3232 | 3229 | 2978 | 2511 | 1619 | 891 | 334 | 17 | 4 |

## C.5. Effect of the Coriolis Terms

To understand the effect of the Coriolis terms, the stability analysis of chordwise motion is conducted by ignoring the Coriolis terms from all the governing equations. Tables C.4, C.5, and C.6 present the value of the imaginary part of the eigenvalue, $\omega$ without the Coriolis terms. Note that the value of the real part, $\sigma$ is zero. The following conclusions can be drawn:

1. The critical angular velocities of the first three modes are essentially unchanged relative to the case with the Coriolis terms.
2. Without Coriolis coupling, axial and lateral motions decouple. The axial equation has constant coefficients and hence, using the axial eigenfunctions as assumed modes that already satisfy the boundary conditions yields immediate convergence.

**Table C.4:** First eigenfrequency ($\mathrm{rad\,s^{-1}}$) for different values of $\Omega$ for ETHZ case (Without the Coriolis terms).

| No. of modes | Angular velocity, $\Omega$ ($\mathrm{rad\,s^{-1}}$) | | | | | |
|---|---|---|---|---|---|---|
| | 0 | 10 | 30 | 50 | 60 | 60.428 |
| 1 | 138.74 | 136.83 | 120.55 | 78.44 | 19.77 | 10.99 |
| 2 | 138.74 | 136.83 | 120.53 | 78.12 | 16.86 | 3.32 |
| 3 | 138.74 | 136.83 | 120.53 | 78.09 | 16.59 | 1.30 |
| 4 | 138.74 | 136.83 | 120.53 | 78.09 | 16.56 | 0.89 |
| 5 | 138.74 | 136.83 | 120.53 | 78.09 | 16.55 | 0.60 |
| 6 | 138.74 | 136.83 | 120.53 | 78.09 | 16.55 | 0.51 |
| 7 | 138.74 | 136.83 | 120.53 | 78.09 | 16.54 | 0.46 |
| 8 | 138.74 | 136.83 | 120.53 | 78.09 | 16.54 | 0.44 |
| 9 | 138.74 | 136.83 | 120.53 | 78.09 | 16.54 | 0.43 |
| 10 | 138.74 | 136.83 | 120.53 | 78.09 | 16.54 | 0.43 |
| Numerical | 138.74 | 136.83 | 120.53 | 78.09 | 16.54 | 0.42 |

**Table C.5:** Second eigenfrequency ($\mathrm{rad\,s^{-1}}$) for different values of $\Omega$ for ETHZ case (Without the Coriolis terms).

| No. of modes | Angular velocity, $\Omega$ ($\mathrm{rad\,s^{-1}}$) | | | | | | |
|---|---|---|---|---|---|---|---|
| | 0 | 10 | 60 | 120 | 180 | 191.25 | 191.358 |
| 1 | – | – | – | – | – | – | – |
| 2 | 1882.86 | 1880.19 | 1784.03 | 1448.32 | 581.94 | 180.58 | 174.53 |
| 3 | 1882.86 | 1880.19 | 1784.01 | 1447.93 | 575.42 | 154.10 | 147.01 |
| 4 | 1882.86 | 1880.19 | 1783.94 | 1446.46 | 555.59 | 72.00 | 56.30 |
| 5 | 1882.86 | 1880.19 | 1783.94 | 1446.37 | 554.28 | 63.11 | 44.45 |
| 6 | 1882.86 | 1880.19 | 1783.93 | 1446.21 | 552.52 | 50.26 | 23.06 |
| 7 | 1882.86 | 1880.19 | 1783.93 | 1446.19 | 552.25 | 47.99 | 17.60 |
| 8 | 1882.86 | 1880.19 | 1783.93 | 1446.17 | 552.02 | 46.04 | 11.31 |
| 9 | 1882.86 | 1880.19 | 1783.93 | 1446.16 | 551.96 | 45.52 | 9.02 |
| 10 | 1882.86 | 1880.19 | 1783.93 | 1446.16 | 551.91 | 45.09 | 6.49 |
| Numerical | 1882.86 | 1880.19 | 1783.93 | 1446.15 | 551.85 | 44.58 | 0.00 |

**Table C.6:** Third eigenfrequency ($\mathrm{rad\,s^{-1}}$) for different values of $\Omega$ for ETHZ case (Without the Coriolis terms).

| No. of modes | Angular velocity, $\Omega$ ($\mathrm{rad\,s^{-1}}$) | | | | | | | |
|---|---|---|---|---|---|---|---|---|
| | 0 | 600 | 1200 | 2400 | 3000 | 3200 | 3232 | 3232.08 |
| 1 | 3232.09 | 3175.91 | 3001.06 | 2164.80 | 1202.65 | 454.29 | 23.48 | 5.85 |
| 5 | 3232.09 | 3175.91 | 3001.06 | 2164.80 | 1202.65 | 454.29 | 23.48 | 5.85 |
| 10 | 3232.09 | 3175.91 | 3001.06 | 2164.80 | 1202.65 | 454.29 | 23.48 | 5.85 |
| Numerical | 3232.09 | 3175.91 | 3001.06 | 2164.80 | 1202.65 | 454.29 | 23.48 | 5.85 |

**Effect of angular velocity on modeshapes**

Figure C.1 shows how the first eigenshape changes as the angular velocity increases. Ten assumed modes are used for both axial and lateral motion. The shapes vary with increasing $\Omega$, due to the effect of axial compression induced by the centrifugal force. Moreover, the effect of the Coriolis terms on the modeshapes is negligible since the modeshapes remain essentially unchanged up to the critical speed, even when the Coriolis terms are neglected.

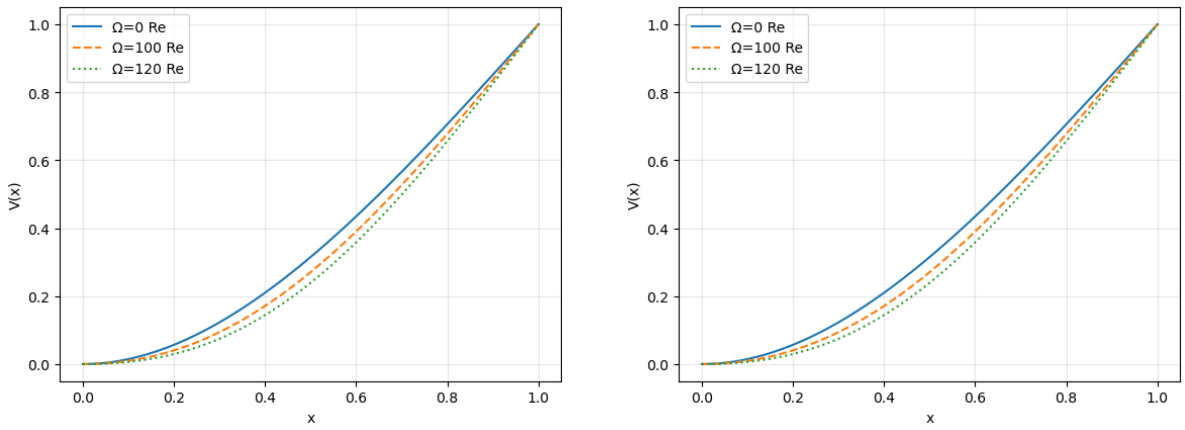


**(a)** First modeshape (Lateral bending), With Coriolis

**(b)** First modeshape (Lateral bending), Without Coriolis

**Figure C.1:** Variation of the first eigenshape with angular velocity (with and without the Coriolis terms).

# D

# Nonlinear EOMs

## D.1. Nonlinear Potential Energy

In Section 2.2, a linearized version of total potential energy is presented, which resulted in a linear set of EOMs. To obtain these, the nonlinear terms that result after substituting the expression of Green-Lagrange strain are neglected. In this appendix, a full set of non-linear EOMs is derived.

For small strains, the general nonlinear expression of the axial strain is given by the Green–Lagrange formulation as

$$\varepsilon_{xx} = u_{x,x} + \frac{1}{2}(u_{x,x}^2 + u_{y,x}^2 + u_{z,x}^2)$$

The total strain energy is given by

$$\frac{1}{2}\,E \int_V \varepsilon_{xx}^2 dV$$

Let $T(x)$ be the axial compression force in the beam acting along the centroid of the cross section. $T(x)$ is assumed to be positive and needs to be solved from the static equilibrium of the axial motion. The potential energy due to $T(x)$ is given by:

$$\int_0^L \left( -\frac{1}{2}T(x)(v_{,x})^2 - \frac{1}{2}T(x)(w_{,x})^2 \right) dx$$

The following relations are used,

$$I_y = \int_A z^2 \,\mathrm{d}A, \quad I_z = \int_A y^2 \,\mathrm{d}A, \quad J_y = \int_A z^4 \,\mathrm{d}A, \quad J_z = \int_A y^4 \,\mathrm{d}A, \quad J_{yz} = \int_A y^2 z^2 \,\mathrm{d}A \tag{D.1}$$

## D.2. Lagrange Function

Substituting the Green-Lagrange strain formulation into the total strain energy and including the potential energy due to axial compression results in the following Lagrange function is obtained

$$
\begin{aligned}
\lambda = & \left[\frac{1}{2}\rho A\left(\frac{\partial u}{\partial t}\right)^2+\frac{1}{2}\rho I_y\left(\frac{\partial^2 w}{\partial x\,\partial t}\right)^2+\frac{1}{2}\rho I_z\left(\frac{\partial^2 v}{\partial x\,\partial t}\right)^2\right.\\
& +\frac{1}{2}\rho A\Omega^2 v^2-\rho A\Omega\, v\left(\frac{\partial u}{\partial t}\right)+\rho I_z\Omega\left(\frac{\partial^2 v}{\partial x\,\partial t}\right)\\
& +\frac{1}{2}\rho A\left(\frac{\partial v}{\partial t}\right)^2+\frac{1}{2}\rho A\Omega^2 u^2+\frac{1}{2}\rho I_y\Omega^2\left(\frac{\partial w}{\partial x}\right)^2+\frac{1}{2}\rho I_z\Omega^2\left(\frac{\partial v}{\partial x}\right)^2\\
& \left.-\rho A\Omega(r+L-x)\left(\frac{\partial v}{\partial t}\right)+\rho A\Omega\, u\left(\frac{\partial v}{\partial t}\right)-\rho A\Omega^2(r+L-x)u+\frac{1}{2}\rho A\left(\frac{\partial w}{\partial t}\right)^2\right]\\
& -\left[\frac{1}{2}EA\left(\frac{\partial u}{\partial x}\right)^2+\frac{1}{2}EI_y\left(\frac{\partial^2 w}{\partial x^2}\right)^2+\frac{1}{2}EI_z\left(\frac{\partial^2 v}{\partial x^2}\right)^2\right.\\
& +\frac{1}{2}EA\left(\frac{\partial u}{\partial x}\right)^3+\frac{3}{2}EI_y\left(\frac{\partial u}{\partial x}\right)\left(\frac{\partial^2 w}{\partial x^2}\right)^2+\frac{3}{2}EI_z\left(\frac{\partial u}{\partial x}\right)\left(\frac{\partial^2 v}{\partial x^2}\right)^2\\
& +\frac{1}{2}EA\left(\frac{\partial u}{\partial x}\right)\left(\frac{\partial v}{\partial x}\right)^2+\frac{1}{2}EA\left(\frac{\partial u}{\partial x}\right)\left(\frac{\partial w}{\partial x}\right)^2\\
& +\frac{1}{8}EA\left(\frac{\partial u}{\partial x}\right)^4+\frac{3}{4}EI_y\left(\frac{\partial u}{\partial x}\right)^2\left(\frac{\partial^2 w}{\partial x^2}\right)^2+\frac{3}{4}EI_z\left(\frac{\partial u}{\partial x}\right)^2\left(\frac{\partial^2 v}{\partial x^2}\right)^2\\
& +\frac{1}{8}EJ_y\left(\frac{\partial^2 w}{\partial x^2}\right)^4+\frac{1}{8}EJ_z\left(\frac{\partial^2 v}{\partial x^2}\right)^4+\frac{3}{4}EJ_{yz}\left(\frac{\partial^2 w}{\partial x^2}\right)^2\left(\frac{\partial^2 v}{\partial x^2}\right)^2\\
& +\frac{1}{8}EA\left(\frac{\partial v}{\partial x}\right)^4+\frac{1}{8}EA\left(\frac{\partial w}{\partial x}\right)^4\\
& +\frac{1}{4}EA\left(\frac{\partial u}{\partial x}\right)^2\left(\frac{\partial v}{\partial x}\right)^2+\frac{1}{4}EI_y\left(\frac{\partial^2 w}{\partial x^2}\right)^2\left(\frac{\partial v}{\partial x}\right)^2+\frac{1}{4}EI_z\left(\frac{\partial^2 v}{\partial x^2}\right)^2\left(\frac{\partial v}{\partial x}\right)^2\\
& +\frac{1}{4}EA\left(\frac{\partial u}{\partial x}\right)^2\left(\frac{\partial w}{\partial x}\right)^2+\frac{1}{4}EI_y\left(\frac{\partial^2 w}{\partial x^2}\right)^2\left(\frac{\partial w}{\partial x}\right)^2+\frac{1}{4}EI_z\left(\frac{\partial^2 v}{\partial x^2}\right)^2\left(\frac{\partial w}{\partial x}\right)^2\\
& \left.+\frac{1}{4}EA\left(\frac{\partial v}{\partial x}\right)^2\left(\frac{\partial w}{\partial x}\right)^2-\frac{1}{2}T(x)\left(\frac{\partial v}{\partial x}\right)^2-\frac{1}{2}T(x)\left(\frac{\partial w}{\partial x}\right)^2\right]
\end{aligned}
\tag{D.2}
$$

## D.3. Nonlinear EOMs

Applying the Euler-Lagrange equations produces the following set of nonlinear EOMs:

Nonlinear EOM for axial displacement:

$$\begin{aligned}
&\rho A\,\frac{\partial^2 u}{\partial t^2} - 2\rho A\Omega\,\frac{\partial v}{\partial t} - EA\,\frac{\partial^2 u}{\partial x^2} - \rho A\Omega^2 u \\
&- \frac{\partial}{\partial x}\left[\frac{3}{2}EA\left(\frac{\partial u}{\partial x}\right)^2 + \frac{3}{2}EI_y\left(\frac{\partial^2 w}{\partial x^2}\right)^2 + \frac{3}{2}EI_z\left(\frac{\partial^2 v}{\partial x^2}\right)^2 + \frac{1}{2}EA\left(\frac{\partial v}{\partial x}\right)^2 + \frac{1}{2}EA\left(\frac{\partial w}{\partial x}\right)^2\right. \\
&+ \frac{1}{2}EA\left(\frac{\partial u}{\partial x}\right)^3 + \frac{3}{2}EI_y\,\frac{\partial u}{\partial x}\left(\frac{\partial^2 w}{\partial x^2}\right)^2 + \frac{3}{2}EI_z\,\frac{\partial u}{\partial x}\left(\frac{\partial^2 v}{\partial x^2}\right)^2 \\
&\left.+ \frac{1}{2}EA\,\frac{\partial u}{\partial x}\left(\frac{\partial v}{\partial x}\right)^2 + \frac{1}{2}EA\,\frac{\partial u}{\partial x}\left(\frac{\partial w}{\partial x}\right)^2\right] = -\rho A\Omega^2(r+L-x).
\end{aligned} \tag{D.3}$$

Nonlinear EOM for lateral displacement:

$$\begin{aligned}
&\rho A\,\frac{\partial^2 v}{\partial t^2} + 2\rho A\Omega\,\frac{\partial u}{\partial t} + EI_z\,\frac{\partial^4 v}{\partial x^4} + \rho I_z\Omega^2\,\frac{\partial^2 v}{\partial x^2} + \frac{\partial}{\partial x}\Big(T(x)\,\frac{\partial v}{\partial x}\Big) - \rho I_z\frac{\partial^4 v}{\partial x^2\,\partial t^2} - \rho A\Omega^2 v \\
&- \frac{\partial}{\partial x}\left[EA\,\frac{\partial u}{\partial x}\,\frac{\partial v}{\partial x} + \frac{1}{2}EA\left(\frac{\partial u}{\partial x}\right)^2\frac{\partial v}{\partial x} + \frac{1}{2}EI_y\left(\frac{\partial^2 w}{\partial x^2}\right)^2\frac{\partial v}{\partial x}\right. \\
&\left.+ \frac{1}{2}EI_z\left(\frac{\partial^2 v}{\partial x^2}\right)^2\frac{\partial v}{\partial x} + \frac{1}{2}EA\left(\frac{\partial w}{\partial x}\right)^2\frac{\partial v}{\partial x} + \frac{1}{2}EA\left(\frac{\partial v}{\partial x}\right)^3\right] \\
&- \frac{\partial^2}{\partial x^2}\left[3EI_z\,\frac{\partial u}{\partial x}\,\frac{\partial^2 v}{\partial x^2} + \frac{3}{2}EI_z\left(\frac{\partial u}{\partial x}\right)^2\frac{\partial^2 v}{\partial x^2} + \frac{1}{2}EJ_z\left(\frac{\partial^2 v}{\partial x^2}\right)^3\right. \\
&\left.+ \frac{3}{2}EJ_{yz}\left(\frac{\partial^2 w}{\partial x^2}\right)^2\frac{\partial^2 v}{\partial x^2} + \frac{1}{2}EI_z\left(\frac{\partial v}{\partial x}\right)^2\frac{\partial^2 v}{\partial x^2} + \frac{1}{2}EI_z\left(\frac{\partial w}{\partial x}\right)^2\frac{\partial^2 v}{\partial x^2}\right] = 0.
\end{aligned} \tag{D.4}$$

Nonlinear EOM for vertical displacement:

$$\begin{aligned}
&\rho A\frac{\partial^2 w}{\partial t^2} + EI_y\frac{\partial^4 w}{\partial x^4} + \rho I_y\Omega^2\frac{\partial^2 w}{\partial x^2} + \frac{\partial}{\partial x}\left[T(x)\frac{\partial w}{\partial x}\right] - \rho I_y\,\frac{\partial^4 w}{\partial x^2\,\partial t^2} \\
&- \frac{\partial}{\partial x}\left[EA\frac{\partial u}{\partial x}\,\frac{\partial w}{\partial x} + \frac{1}{2}EA\left(\frac{\partial u}{\partial x}\right)^2\frac{\partial w}{\partial x} + \frac{1}{2}EI_y\left(\frac{\partial^2 w}{\partial x^2}\right)^2\frac{\partial w}{\partial x}\right. \\
&\left.+ \frac{1}{2}EI_z\left(\frac{\partial^2 v}{\partial x^2}\right)^2\frac{\partial w}{\partial x} + \frac{1}{2}EA\left(\frac{\partial v}{\partial x}\right)^2\frac{\partial w}{\partial x} + \frac{1}{2}EA\left(\frac{\partial w}{\partial x}\right)^3\right] \\
&- \frac{\partial^2}{\partial x^2}\left[3EI_y\,\frac{\partial u}{\partial x}\,\frac{\partial^2 w}{\partial x^2} + \frac{3}{2}EI_y\left(\frac{\partial u}{\partial x}\right)^2\frac{\partial^2 w}{\partial x^2} + \frac{1}{2}EJ_y\left(\frac{\partial^2 w}{\partial x^2}\right)^3\right. \\
&\left.+ \frac{3}{2}EJ_{yz}\left(\frac{\partial^2 v}{\partial x^2}\right)^2\frac{\partial^2 w}{\partial x^2} + \frac{1}{2}EI_y\left(\frac{\partial v}{\partial x}\right)^2\frac{\partial^2 w}{\partial x^2} + \frac{1}{2}EI_y\left(\frac{\partial w}{\partial x}\right)^2\frac{\partial^2 w}{\partial x^2}\right] = 0.
\end{aligned} \tag{D.5}$$

The natural boundary conditions at $x = L$ are given by:

Axial force equilibrium at $x = L$

$$
\begin{aligned}
&M\,\frac{\partial^2 u}{\partial t^2} - 2M\Omega\,\frac{\partial v}{\partial t} + EA\,\frac{\partial u}{\partial x} - M\Omega^2 u \\
&+ \left[\frac{3}{2}EA\left(\frac{\partial u}{\partial x}\right)^2 + \frac{3}{2}EI_y\left(\frac{\partial^2 w}{\partial x^2}\right)^2 + \frac{3}{2}EI_z\left(\frac{\partial^2 v}{\partial x^2}\right)^2 + \frac{1}{2}EA\left(\frac{\partial v}{\partial x}\right)^2 + \frac{1}{2}EA\left(\frac{\partial w}{\partial x}\right)^2\right. \\
&+ \frac{1}{2}EA\left(\frac{\partial u}{\partial x}\right)^3 + \frac{3}{2}EI_y\,\frac{\partial u}{\partial x}\left(\frac{\partial^2 w}{\partial x^2}\right)^2 + \frac{3}{2}EI_z\,\frac{\partial u}{\partial x}\left(\frac{\partial^2 v}{\partial x^2}\right)^2 \\
&\left.+ \frac{1}{2}EA\,\frac{\partial u}{\partial x}\left(\frac{\partial v}{\partial x}\right)^2 + \frac{1}{2}EA\,\frac{\partial u}{\partial x}\left(\frac{\partial w}{\partial x}\right)^2\right] = -M\Omega^2 r.
\end{aligned}
\tag{D.6}
$$

Shear force equilibrium along lateral direction at $x = L$

$$
\begin{aligned}
&M\frac{\partial^2 v}{\partial t^2} + 2M\Omega\frac{\partial u}{\partial t} - EI_z\frac{\partial^3 v}{\partial x^3} - M\Omega^2 v - T(L)\,\frac{\partial v}{\partial x} - \rho I_z\Omega^2\,\frac{\partial v}{\partial x} + \rho I_z\,\frac{\partial^3 v}{\partial x\,\partial t^2} \\
&+ \left[EA\,\frac{\partial u}{\partial x}\,\frac{\partial v}{\partial x} + \frac{1}{2}EA\left(\frac{\partial u}{\partial x}\right)^2\frac{\partial v}{\partial x} + \frac{1}{2}EI_y\left(\frac{\partial^2 w}{\partial x^2}\right)^2\frac{\partial v}{\partial x}\right. \\
&\left.+ \frac{1}{2}EI_z\left(\frac{\partial^2 v}{\partial x^2}\right)^2\frac{\partial v}{\partial x} + \frac{1}{2}EA\left(\frac{\partial w}{\partial x}\right)^2\frac{\partial v}{\partial x} + \frac{1}{2}EA\left(\frac{\partial v}{\partial x}\right)^3\right] \\
&- \frac{\partial}{\partial x}\left[3EI_z\,\frac{\partial u}{\partial x}\,\frac{\partial^2 v}{\partial x^2} + \frac{3}{2}EI_z\left(\frac{\partial u}{\partial x}\right)^2\frac{\partial^2 v}{\partial x^2} + \frac{1}{2}EJ_z\left(\frac{\partial^2 v}{\partial x^2}\right)^3\right. \\
&\left.+ \frac{3}{2}EJ_{yz}\left(\frac{\partial^2 w}{\partial x^2}\right)^2\frac{\partial^2 v}{\partial x^2} + \frac{1}{2}EI_z\left(\frac{\partial v}{\partial x}\right)^2\frac{\partial^2 v}{\partial x^2} + \frac{1}{2}EI_z\left(\frac{\partial w}{\partial x}\right)^2\frac{\partial^2 v}{\partial x^2}\right] = 0.
\end{aligned}
\tag{D.7}
$$

Moment equilibrium along lateral direction at $x = L$

$$
\begin{aligned}
&-\ EI_z\,\frac{\partial^2 v}{\partial x^2} - J\frac{\partial^3 v}{\partial x\,\partial t^2} - 3EI_z\,\frac{\partial u}{\partial x}\,\frac{\partial^2 v}{\partial x^2} - \frac{3}{2}EI_z\left(\frac{\partial u}{\partial x}\right)^2\frac{\partial^2 v}{\partial x^2} \\
&- \frac{1}{2}EJ_z\left(\frac{\partial^2 v}{\partial x^2}\right)^3 - \frac{3}{2}EJ_{yz}\left(\frac{\partial^2 w}{\partial x^2}\right)^2\frac{\partial^2 v}{\partial x^2} \\
&- \frac{1}{2}EI_z\left(\frac{\partial v}{\partial x}\right)^2\frac{\partial^2 v}{\partial x^2} - \frac{1}{2}EI_z\left(\frac{\partial w}{\partial x}\right)^2\frac{\partial^2 v}{\partial x^2} = 0.
\end{aligned}
\tag{D.8}
$$

Shear force equilibrium along vertical direction at $x = L$

$$
\begin{aligned}
&M\,\frac{\partial^2 w}{\partial t^2} - EI_y\,\frac{\partial^3 w}{\partial x^3} - T(L)\,\frac{\partial w}{\partial x} - \rho I_y\Omega^2\,\frac{\partial w}{\partial x} + \rho I_y\,\frac{\partial^3 w}{\partial x\,\partial t^2} \\
&- \frac{\partial}{\partial x}\left[3EI_y\,\frac{\partial u}{\partial x}\,\frac{\partial^2 w}{\partial x^2} + \frac{3}{2}EI_y\left(\frac{\partial u}{\partial x}\right)^2\frac{\partial^2 w}{\partial x^2} + \frac{1}{2}EJ_y\left(\frac{\partial^2 w}{\partial x^2}\right)^3\right. \\
&\left.+ \frac{3}{2}EJ_{yz}\left(\frac{\partial^2 v}{\partial x^2}\right)^2\frac{\partial^2 w}{\partial x^2} + \frac{1}{2}EI_y\left(\frac{\partial v}{\partial x}\right)^2\frac{\partial^2 w}{\partial x^2} + \frac{1}{2}EI_y\left(\frac{\partial w}{\partial x}\right)^2\frac{\partial^2 w}{\partial x^2}\right] \\
&+ \left[EA\,\frac{\partial u}{\partial x}\,\frac{\partial w}{\partial x} + \frac{1}{2}EA\left(\frac{\partial u}{\partial x}\right)^2\frac{\partial w}{\partial x} + \frac{1}{2}EI_y\left(\frac{\partial^2 w}{\partial x^2}\right)^2\frac{\partial w}{\partial x}\right. \\
&\left.+ \frac{1}{2}EI_z\left(\frac{\partial^2 v}{\partial x^2}\right)^2\frac{\partial w}{\partial x} + \frac{1}{2}EA\left(\frac{\partial w}{\partial x}\right)^3 + \frac{1}{2}EA\left(\frac{\partial v}{\partial x}\right)^2\frac{\partial w}{\partial x}\right] = 0.
\end{aligned}
\tag{D.9}
$$

Moment equilibrium along vertical direction at $x = L$

$$
\begin{aligned}
&- EI_y \frac{\partial^2 w}{\partial x^2} - J \frac{\partial^3 w}{\partial x \, \partial t^2} - 3EI_y \frac{\partial u}{\partial x} \frac{\partial^2 w}{\partial x^2} - \frac{3}{2} EI_y \left( \frac{\partial u}{\partial x} \right)^2 \frac{\partial^2 w}{\partial x^2} \\
&- \frac{1}{2} EJ_y \left( \frac{\partial^2 w}{\partial x^2} \right)^3 - \frac{3}{2} EJ_{yz} \left( \frac{\partial^2 v}{\partial x^2} \right)^2 \frac{\partial^2 w}{\partial x^2} \\
&- \frac{1}{2} EI_y \left( \frac{\partial v}{\partial x} \right)^2 \frac{\partial^2 w}{\partial x^2} - \frac{1}{2} EI_y \left( \frac{\partial w}{\partial x} \right)^2 \frac{\partial^2 w}{\partial x^2} = 0.
\end{aligned}
\tag{D.10}
$$

Note that ignoring the nonlinear terms from the above equations generates the linearized EOMs as presented in Chapter 2.

# E

# Rigid Point Mass Approximation

In this study, the small-scale model of a monopile-founded OWT tested inside a geotechnical centrifuge is represented as a cantilever beam based on Rayleigh beam theory, with the soil stiffness idealized through a lumped spring model. An alternative representation, henceforth called as "rigid point mass approximation", is to model the system as a rigid point mass connected to the soil by a massless rigid beam, where the soil stiffness is again described using translational and rotational springs, analogous to the lumped spring approach. This formulation results in three translational and two rotational degrees of freedom (torsion neglected). The eigenfrequencies obtained from this simplified model are expected to coincide with those from the beam model when the beam density, $\rho$, is assumed to be very small and the Young's modulus, $E$, is taken to be very large. The results of this comparison are summarized in the following table.

**Table E.1:** Input parameters for the beam model to simulate rigid point mass approximation.

| Parameter | Symbol | Value | Unit |
|---|---|---|---|
| Beam length | $L$ | $1.0$ | $\mathrm{m}$ |
| Young's modulus | $E$ | $6.89 \times 10^{15}$ | $\mathrm{Pa}$ |
| Second moment of area | $I$ | $2.179 \times 10^{-7}$ | $\mathrm{m}^4$ |
| Density | $\rho$ | $2.7$ | $\mathrm{kg/m}^3$ |
| Cross–sectional area | $A$ | $3.70 \times 10^{-4}$ | $\mathrm{m}^2$ |
| Centrifuge radius | $r$ | $3.40625$ | $\mathrm{m}$ |
| Tip mass | $M_{\text{tip}}$ | $2.1$ | $\mathrm{kg}$ |
| Tip mass inertia | $J_{\text{tip}}$ | $1.45 \times 10^{-7}$ | $\mathrm{kgm}^2$ |
| **Soil spring stiffness values ($E = 28\,\mathrm{MPa}$ at $0.09\,\mathrm{m}$ depth)** | | | |
| Lateral stiffness | $K_L$ | $1.299 \times 10^7$ | $\mathrm{N\,m}^{-1}$ |
| Rotational stiffness | $K_R$ | $1.070 \times 10^6$ | $\mathrm{N\,m\,rad}^{-1}$ |
| Cross–coupling stiffness | $K_{LR}$ | $-2.475 \times 10^6$ | $\mathrm{N}$ |
| Vertical stiffness | $K_V$ | $1.034 \times 10^7$ | $\mathrm{N\,m}^{-1}$ |

The following table shows the results by using the above set of parameter values.

**Table E.2:** Buckling results for the rigid material case.

| **Mode of motion** | **Instability type** | $\Omega_{\text{cr}}$ $(\text{rad}\,\text{s}^{-1})$ |
|---|---|---|
| Flapwise bending | Divergence | $289.2$ |
| Chordwise bending (decoupled) | Divergence | $242.6$ |
| Axial motion (decoupled) | Divergence | $2219$ |
| Coupled chordwise motion | Divergence (lateral bending) | $242.6$ |

The following figure presents the eigenshapes for the rigid point mass approximation.

# F

# Eigenshapes of Chordwise Motion

In this appendix, the evolution of eigenshapes of chordwise motion is plotted as a function of angular velocity for the ETHZ case, without SSI, using numerical analysis. No noticeable difference is visible due to the exclusion of the Coriolis terms.

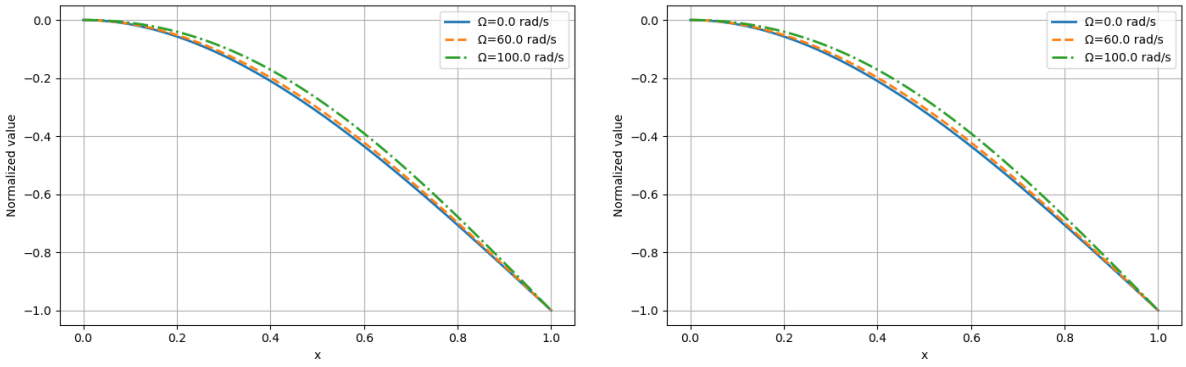


**(a)** With Coriolis term

**(b)** Without Coriolis term

**Figure F.1:** First eigenshape of chordwise motion with and without the Coriolis terms for various angular velocities

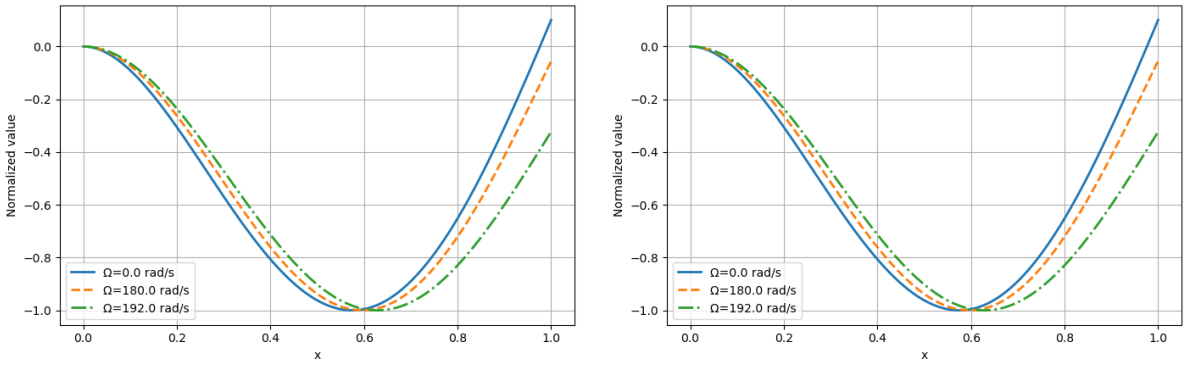


**(a)** With Coriolis term

**(b)** Without Coriolis term

**Figure F.2:** Second eigenshape of chordwise motion with and without the Coriolis terms for various angular velocities

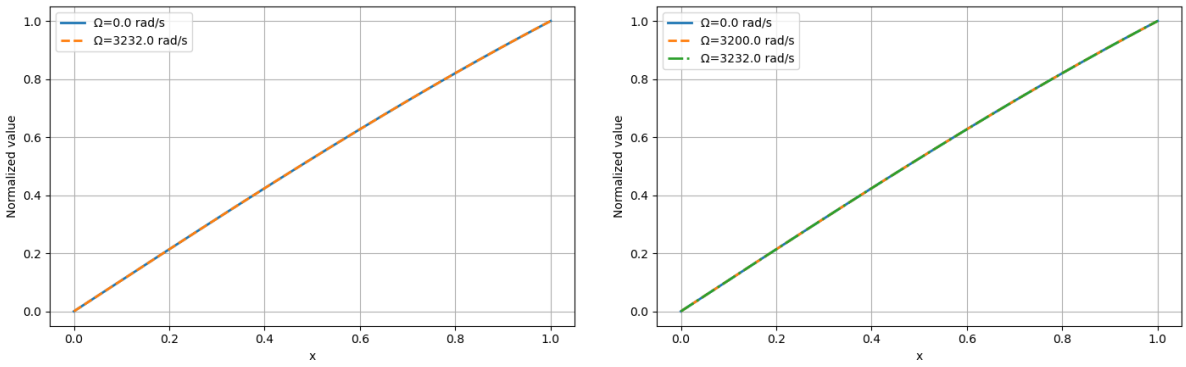


**(a)** With Coriolis term **(b)** Without Coriolis term

**Figure F.3:** Third eigenshape of chordwise motion with and without the Coriolis terms for various angular velocities

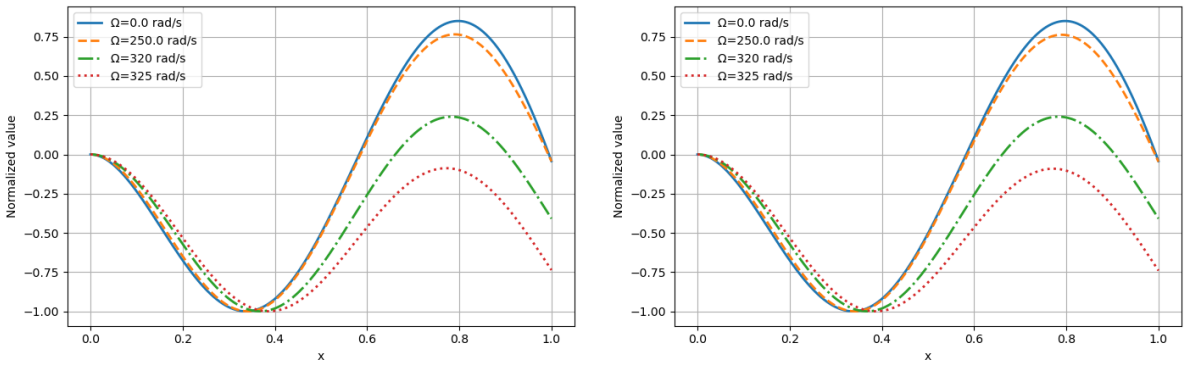


**(a)** With Coriolis term **(b)** Without Coriolis term

**Figure F.4:** Fourth eigenshape of chordwise motion with and without the Coriolis terms for various angular velocities